Deracemization of sodium chlorate with or without the influence of sodium dithionate

Manon Schindler

Normandie Université

THÈSE

Pour obtenir le diplôme de doctorat

Spécialité Physique

Préparée au sein de l'Université de Rouen Normandie

Deracémisation du chlorate de sodium avec et sans l'influence du dithionate de sodium

Présentée et soutenue par
Manon SCHINDLER

Thèse soutenue publiquement le 13 mars 2020 devant le jury composé de		
Mme. Elizabeth HILLARD	Dr. Hab. Université de Bordeaux	Rapporteur
M. Elias VLIEG	Pr. Université Radboud de Nimègue	Rapporteur
Mme. Sylvie MALO	Pr. Université de Caen Normandie	Présidente
M. Woo Sik KIM	Pr. Université Kyung Hee de Séoul	Examinateur
M. Gérard COQUEREL	Pr. Université de Rouen Normandie	Directeur de thèse

Thèse dirigée par Gérard COQUEREL, professeur des universités au laboratoire Sciences et Méthodes Séparatives (EA3233 SMS)

UNIVERSITÉ DE ROUEN NORMANDIE

ED PSIME

SMS Sciences et Méthodes Séparatives

Projet cofinancé par l'Union Européenne
L'Europe s'engage avec le Fonds européen de développement régional

THÈSE

Pour obtenir le diplôme de doctorat

Spécialité Physique

Préparée au sein de l'Université de Rouen Normandie

Deracemization of sodium chlorate with or without the influence of sodium dithionate

Présentée et soutenue par
Manon SCHINDLER

Thèse soutenue publiquement le 13 mars 2020 devant le jury composé de		
Mme. Elizabeth HILLARD	Dr. Hab. Université de Bordeaux	Rapporteur
M. Elias VLIEG	Pr. Université Radboud de Nimègue	Rapporteur
Mme. Sylvie MALO	Pr. Université de Caen Normandie	Présidente
M. Woo Sik KIM	Pr. Université Kyung Hee de Séoul	Examinateur
M. Gérard COQUEREL	Pr. Université de Rouen Normandie	Directeur de thèse

Thèse dirigée par Gérard COQUEREL, professeur des universités au laboratoire Sciences et Méthodes Séparatives (EA3233 SMS)

Projet cofinancé par l'Union Européenne
L'Europe s'engage avec le Fonds européen de développement régional

Acknowledgements

This work was funded by the Normandy region and European regional development fund (FEDER) through the SCAMPI project.

First, I want to thank Prof. Gérard Coquerel for giving me the opportunity to achieve this Ph.D in the SMS laboratory and supervising me. Thank you for sharing your knowledge and your infinite passion for heterogeneous equilibria, crystallization and crystals in general, which brought me here today. Moreover, thank you for your determination to find the best opportunities for all of us. In my case, my Swiss break of 5 months in Nestlé would not have been possible without your disposition to think outside the box. It has been a great opportunity to develop my knowledge about crystallization in industrial field and to reinforce my English level.

Then, I give a particular thanks to Dr. Clément Brandel for supervising my master and Ph.D work. I thank you for sharing your knowledge and valuable ideas and proposals during the past 3 years, for spending time to read and amend all of my writings and presentations and for having believe in me since the beginning. This Ph.D would not have been the same without your contribution and your support.

I would like to thank the jury members, Dr. Elizabeth Hillard and Pr. Elias Vlieg as reviewers and Pr. Sylvie Malo and Pr. Woo Sik Kim as examiners, for accepting to review my thesis. All of your comments will certainly lead to interesting discussion during the defense. I would like thank twice Pr. Woo Sik Kim for our fruitful discussion and collaboration and also Bowen Zhang for our exchange of results and advises.

J'écris maintenant en français pour remercier toutes les personnes qui ont contribuées, à leur manière et de plus ou moins loin à cette thèse.

Merci aux Docteurs-Permanents du laboratoire, Yohann Cartigny, pour m'avoir mis le pied à l'étrier des équilibres hétérogènes et de m'avoir encadrée et conseillée pendant mes deux premiers passages au laboratoire ; Gabin Gbabode pour toutes nos longues discussions scientifiques et non scientifiques, ainsi que pour ta sympathie et ta gentillesse ; Valérie Dupray, coordinatrice du projet européen que je remercie pour sa patience et sa bienveillance. Merci à Morgane Sanselme et Nicolas Couvrat pour leur aide scientifique au quotidien mais aussi pour leur humour tout feu tout flamme (Bisous à Allan !).

Merci aux autres permanent(e)s du laboratoire, Lucie, pour ta patience devant les personnes allergiques aux tâches administratives ! Merci à Céline (marathonienne !), pour tes conseils en CAP et nos moments ensemble en général, une petite déception de n'avoir jamais fait les TPs avec toi. Marie, merci à toi pour ta gentillesse, même si on m'a dit que tu râlais des fois, moi je ne retiendrai que ta bonne humeur et nos rires !

Merci aux étudiants, les nouveaux arrivés et les « déjà partis » : Benjamin, merci évidemment pour ton aide précieuse au début de cette thèse, mais aussi pour toutes tes qualités, trop nombreuses pour les énumérer, merci pour les conseils, les livres, et les bons moments. Merci à Clément (DSJ) pour ton amitié et ton aide aussi sur la fin de cette thèse, j'espère avoir pu en faire au moins la moitié pour toi en retour. Des Cœurs et des bisous pour toi ! De la même génération, je remercie FX, entre taquinage et démontage de Couette Taylor, Bienvenu pour sa bonne humeur et ces terribles anecdotes et Antoine, pas pour ta bonne humeur ni ta gentillesse, mais pour ton humour sarcastique c'est sûr ! Merci à Simon, Docteur loulou, pour nos discussions en général, même si tu as abandonné ton poste au Technicum ! Une pensée pour tous ceux que je n'ai pas beaucoup vu mais avec qui les conversations étaient toujours culturellement intéressantes, Aliou, Lina et Kangli, je vous souhaite toute la réussite que vous méritez. Je souhaite bon courage aux suivants : Chloé, Laureline, Marine, Aurélien, Florent (peut être !) et Mélodie. N'ayez pas peur, c'est malgré tout une super aventure ! Laureline et Chloé, je compte sur vous pour garder l'esprit féminin du bureau !

En dehors du laboratoire, je remercie profondément Clément et Éléonore, pour votre amitié, pour nos discussions sans fin sur la thèse (promis, les gars c'est finit maintenant ! Enfin…), pour nos soirées, nos vacances, et bref, tout quoi ! Que cela dure. Merci aux copains d'il y a longtemps, Paul, Chris, Pauline, Margot, Agathe, Thomas, aux copines qui sont beaucoup trop loin, Shannon, Sarah, Noëlline, et aux nouveaux, l'équipe de choc, Mélaine, Thomas, Ju, Alex, Cécile, Cora, Flo, peut être au ski l'année prochaine ?

Merci à ma famille, mes parents, Christine et Philippe, et mes frères, Clément, Simon et Antoine. Plus besoin d'essayer de prononcer « deracemization » vous l'aurez assez entendu, et moi aussi !

Enfin, merci à Antoine, mon Loulou, pour ton soutien infaillible pendant 3 ans et même plus. Merci pour ton amour depuis tout ce temps. Vivement la suite.

General Introduction

Crystallization is a key operation in the manufacturing and purification of crystallized compounds. Physical chemical properties such as structural purity, crystal size distribution, occurrence of polymorphism, hydrate or solvate, can be significantly impacted and controlled by the crystallization step which includes nucleation, growth and agglomeration mechanisms. Since different crystalline forms (*e.g.* polymorphs or enantiomorphs) often have different (or opposite) physical chemical properties (such as solubility, thermal stability, bioavailability or bioactivity), it is very important to control the process to afford the desired material with satisfactory attributes.

In the field of pharmaceutical chemistry, crystallization based methods are used to resolve enantiomers when asymmetric synthesis or chiral chromatography are not feasible. Enantiomer resolutions *via* crystallization, *i.e.* by means of diastereomeric resolution, preferential crystallization (PC) or deracemization, give access to the pure enantiomer in solid phase. The advantage of deracemization over the other methods is the conversion of the unwanted enantiomer into the desired enantiomer by means of racemization at the solvated state, giving rise to a theoretical yield of 100%.

The deracemization mechanism is still matter of debate and is currently intensively studied using different model compounds under various conditions.

In the present manuscript, research is focused on the study of sodium chlorate ($NaClO_3$) deracemization. $NaClO_3$ is an achiral compound which exhibits supramolecular chirality, and which was originally used to prove the feasibility of deracemization. Due to the absence of chirality in the solvated state, racemization is not based on a chemical reaction, which is often a limiting factor in other deracemization processes. It is therefore a good candidate to focus investigations on other mechanisms involved in deracemization, mainly crystallization, dissolution, breakage and agglomeration processes.

Chapter 1 focuses on the necessary generalities concerning chirality and crystallization that are required for a good understanding of this work. The rest of the manuscript is divided in three parts:

Chapter 2 is focused on the synthesis and on the solid state characterization of a crystalline compound: Sodium dithionate ($Na_2S_2O_6$). This compound attracted our attention as it can be used as an achiral impurity in $NaClO_3$ deracemization. After synthesis of the compound, thermal and chemical stability are investigated by means of complementary analyses in order to ensure the absence of reaction under deracemization conditions.

Chapter 3 is devoted to $NaClO_3$ deracemization. Two different processes are studied and compared: (i) attrition-enhanced deracemization and (ii) temperature cycling-induced deracemization (TCID). The influence of $Na_2S_2O_6$, as impurity is investigated for the TCID process and the results provide a better understanding of the mechanisms involved during the deracemization process *via* specific experiments of crystal growth and secondary nucleation estimates.

Chapter 4 is dedicated to the set-up of a new reactor, a Couette Taylor (CT) reactor, in order to perform $NaClO_3$ deracemization. Indeed, from an industrial perspective, increasing productivity is challenging. The CT reactor gives the possibility to set a continuous process for deracemization (and/or more generally for other crystallization processes), which could considerably increase the productivity. After the implementation of the reactor, the feasibility of deracemization is investigated, then perspectives for optimization are proposed.

The general concern of this work is to reach a better understanding of the deracemization process, particularly for the TCID process. A general conclusion gathers results, proposes a general mechanism of deracemization for the TCID process and summarizes hopeful perspectives for the process in a CT reactor.

Chapter I State of the Art

Crystal Genesis, Chirality and Deracemization

I. Crystal Genesis

A. Crystalline State

There are three common states of matter: gas, liquid and solid. In the solid state, the constituents (molecules, atoms and/or ions) are close packed. According to their degrees of order, two kind of solids can be described.[1] In the crystalline state, the constituents are organized in a periodic array, *i.e.* a three dimensional and strict arrangement. The resulting macroscopic particle is called a *crystal* and presents a long range order (Figure I-1-a). By contrast, in the amorphous state, the solid presents only a short range order comparable to the arrangement found in the liquid state (Figure I-1-b).

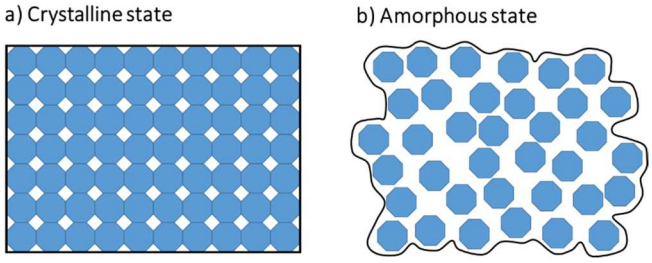

Figure I-1: Schematic organization of (a) a crystal with a regular arrangement of atoms, i.e. a long range order and (b) an amorphous solid characterized by a short range order.

According to the interactions occurring between the constituents (covalent, metallic, ionic or hydrogen bonds), crystals are classified in different groups: ionic crystals, covalent crystals or molecular crystals.

A chemical compound able to form different crystalline structures presents *polymorphism*, from the Greek words 'poly' and 'morph' meaning 'several' and 'shape' respectively. Each form, *i.e.* each polymorph of this compound, has different physico-chemical properties (melting point, solubility,...*etc*) due to the difference in crystal packing (Figure I-2).[2,3]

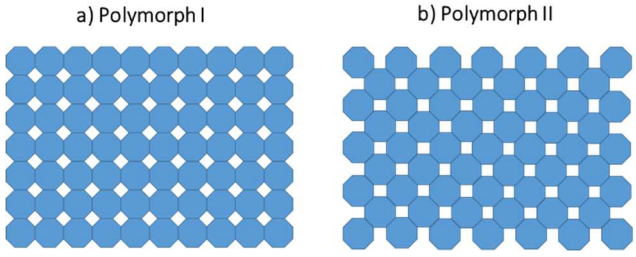

Figure I-2 : Schematic representation of two different crystalline structures of the same compound. Each crystalline structure is a polymorph, named here (a) polymorph I and (b) polymorph II.

When two compounds A and B are involved, miscibility in the solid state exists when compound A is able to accept compound B in its crystal structure. This is possible if only a small change in the crystal packing of A is involved. Two miscible solids form a *solid solution*. According to the organization of pure A and pure B, two kinds of solid solutions can be described: (i) solid solutions by insertion (Figure I-3-a), where B particles occupy the interstitial sites of the A structure, and (ii) solid solutions by substitution (Figure I-3-b) where B particles replace A particles at random, possibly giving rise to a complete solid solution between A and B. This kind of solid solution suggests that the crystalline structures of the pure components A and B are similar.[4]

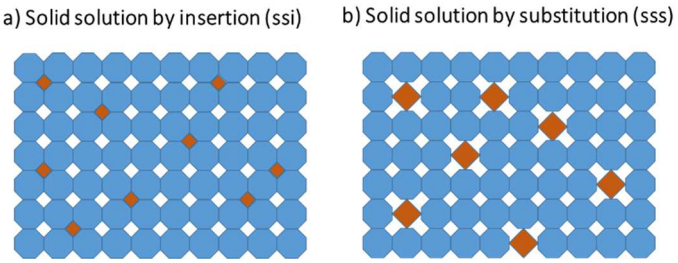

Figure I-3 : Schematic representation of a solid solution (a) by insertion or (b) by substitution.

Partial solid solutions and complete solid solutions give rise to specific phase equilibria represented in Figure I-4-a and Figure I-4-b respectively.

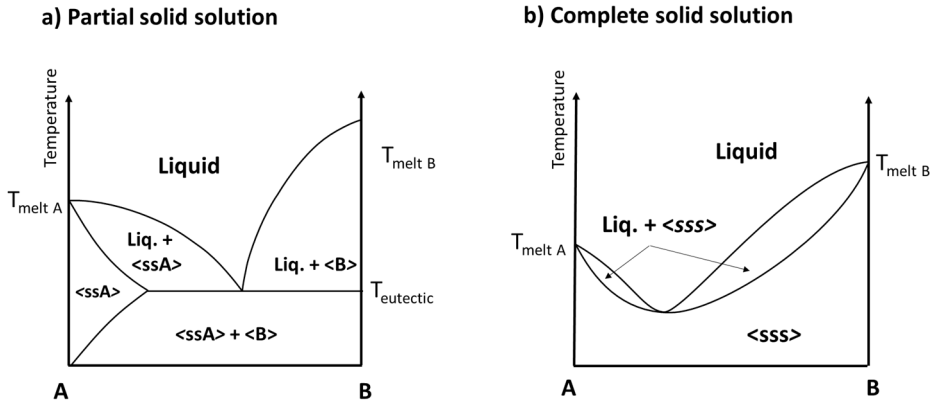

Figure I-4 : Phase diagrams between compounds A and B with a) Partial solid solution of A and b) formation of a complete solid solution between A and B.

By contrast, two compounds A and B can also form a new crystalline architecture that differs from their initial crystal structures (Figure I-5). This new compound AB (provided an equimolar ratio of A and B is involved) is called either a *co-crystal*, a *stoichiometric compound* or a *defined compound*. In the particular case where one of the components is a solvent, *i.e.* in liquid state at room temperature (T) and atmospheric pressure (P), the co-crystal is called a *solvate*. Even more specifically, if one of the components is water, the

crystal is named a *hydrate*.[5,6] Salts are specific co-crystals where the packing is maintained by ionic bonds and proton transfer, as opposed to strong hydrogen bonds or Van Der Walls interactions found in common co-crystals.[7]

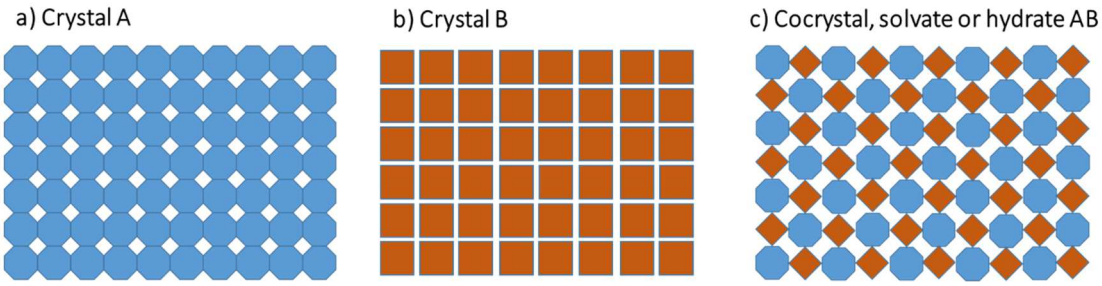

Figure I-5 : Schematic representation of two different crystals from two different compounds (a) A and (b) B forming (c) a new crystalline structure AB. This new crystal form AB is called a co-crystal or a solvate according to the state at which one of the co former (e.g. B) exists under ambient conditions. Additionally, if B is water, AB is called a hydrate.

Phase equilibria in the case of stoichiometric compound formations are represented in Figure I-6-a. In addition to the situations described in Figure I-3 and I-4, it is also possible that no interactions occur between A and B: there is absence of solid state miscibility (Figure I-6-b).

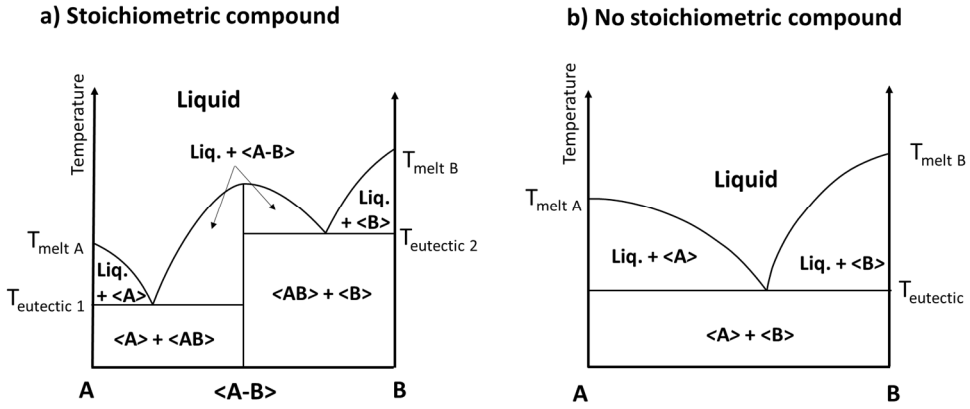

Figure I-6 : Phase diagrams between A and B a) with a stoichiometric compound AB and b) without formation of a stoichiometric compound.

B. Crystallography

Crystallography is the science describing the packing of the matter in a crystal. The periodicity in all possible crystalline structures is described by the 230 space groups (SG). They are the combination of one of the 14 Bravais lattices with one of the 32 point groups. Although it should be noted that all possible combinations of the 14 Bravais lattices and the 32 point groups should be 448 space groups (32×14), but as some SG are isomorphic,

the number of distinct SG is actually reduced to 230.[8] Among the 230 SG, three different classes are described as a function of the chirality and the centrosymmetry of the SG:[9]

- 92 SG are centrosymmetric and achiral: They present an inversion center as a symmetry element and are then compatible with a racemic mixture of enantiomers.
- 65 SG are non-centrosymmetric and can contain chiral structures. Among them, 22 SG are chiral SG (11 enantiomorphic pairs). According to the Sohncke classification, those 65 SG contain only first class symmetry elements, such as rotation, translation or screw axis, which preserve the orientation and the handedness of the symmetry unit. Necessarily, pure enantiomers (see below) crystallize in one of these 65 non-centrosymmetric Sohncke types SG.
- 73 SG are non-centrosymmetric but achiral: Even though they do not present inversion centers, they remain compatible with a mixture of enantiomers by means of glide mirrors or inverted axes.

C. Principle of Crystallization from Solution

Crystal genesis is the study of crystal formation, that is to say the process of crystallization. It is about how a crystalline long range order emerges from a less ordered medium (amorphous solid, liquid, gas state or dissolved compound in a solvent). Crystallization proceeds in three steps: (i) first a driving force must be established, (ii) then formation of nuclei up to a suitable size and (iii) growth of nuclei, *i.e.* crystal growth.

In the present manuscript, almost every crystallization was performed from solutions.

1. Establishment of the Driving Force: The Supersaturation β

The amount of a component dissolved in a solvent is expressed by the concentration C, *i.e.* the mass (or the number of moles) of the component dissolved per weight (or volume) unit of the solvent. At a given temperature and pressure, the concentration of a given component in a given solvent has a limit: the solubility, C*.

The solubility is the maximal amount of compound which can be dissolved per weight (or volume) unit of the solvent, at fixed T and P (Figure I-7- solid line). However, this limit can be overcome in particular conditions (see below). Then, the system is supersaturated, and supersaturation is the driving force for solution crystallization. β is the ratio of supersaturation and is defined (Equation I-1) as the ratio of the concentration *C* by *C**.

$$\beta = \frac{C}{C^*}$$ *Equation I-1*

When:

- β < 1, the system is undersaturated
- β = 1, the system is saturated
- β > 1, the system is supersaturated.

A supersaturated solution is in a metastable state which can be achieved either by increasing the concentration, *e.g.* by solvent evaporation (Figure I-7-1), or by decreasing *C**, *e.g.* by cooling or the addition of an anti-solvent (Figure I-7-2).[10] Crystallization of the excess amount in the liquid phase restores the stable equilibrium state. However, for low supersaturation, *i.e.* β slightly superior to 1, the driving force is sometimes not sufficient to induce spontaneous crystallization and the system can stay in this metastable state, until a certain limit of β. This limit has been described by Ostwald in 1897 and is now called the Ostwald limit (dashed line in Figure I-7).[11] Therefore, the metastable domain is defined by the metastable zone width (MSZW) between the solubility curve and the Ostwald limit (represented in grey in Figure I-7). In this domain, spontaneous crystallization is unlikely.[12] Therefore, the higher β, the more uncontrolled the crystallization.

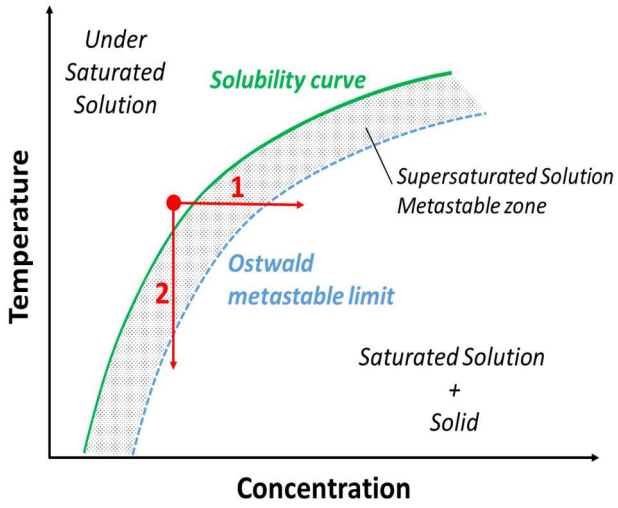

Figure I-7: Solubility curve (green solid line) of a compound in solution and Ostwald limit (blue dashed line). Crystallization is triggered (1) by an increase of the concentration, that is to say, by solvent evaporation or (2) by a decrease of the solubility, that is to say, by a decrease of the temperature.

2. Nucleation

Nucleation is the second step towards crystallization. Two kinds of nucleation, primary or secondary, are described according to the origin of the formation of the nuclei.[13]

- Primary nucleation

Primary nucleation is the formation of nuclei from a solution where no crystalline particle of the solute compound is present. In a supersaturated solution, solvated particles tend to aggregate by forming bonds. The aggregates can either redissolve or grow further into nuclei. When such aggregation occurs without the assistance of a foreign substance (e.g. crystallizer sides, impurities…), this is *homogeneous nucleation*.[14] The free enthalpy of nucleation, $\Delta G_{nucleation}$ accounts for the free energy of the nucleus. Two opposite energetic contributions are involved in $\Delta G_{nucleation}$: (i) the Gibbs free energy associated with crystallization, Δg_{υ} of the system, is a negative contribution, proportional to the nuclei volume and due to the decrease of free enthalpy (exothermicity of the nucleation) and of entropy (there is an increase of order upon aggregation) and (ii) a positive contribution due to the creation of a solid-liquid interface, therefore proportional to the nuclei surface and to the surface free energy γ (per unit area of the nucleus). Then, $\Delta G_{nucleation}$ is defined as Equation I-2.[13]

$$\Delta G_{nucleation} = -\frac{4}{3}\pi r^3 \Delta g_{\upsilon} + 4\pi r^2 \gamma \qquad \textit{Equation I-2}$$

The evolution of $\Delta G_{nucleation}$ is schematically plotted in Figure I-8. The nucleus has to reach a critical size (r*) to be able to grow. Below r*, the contribution of the surface energy dominates, $\Delta G_{nucleation}$ is positive, the nucleus is unstable and the growth is unfavorable. When the nucleus size reaches r*, *i.e.* $\Delta G_{nucleation}$ reaches the highest value, ΔG^*, the growth of the nucleus is favorable as $\Delta G_{nucleation}$ will decrease. However, for $r^* < r < r_0$, $\Delta G_{nucleation}$ is still positive, thus, nucleus is thermodynamically metastable and kinetically stable as the re-dissolution of the nucleus would increase $\Delta G_{nucleation}$. Afterwards, for $r > r_0$, $\Delta G_{nucleation}$ becomes negative, the nucleus is thermodynamically stable.

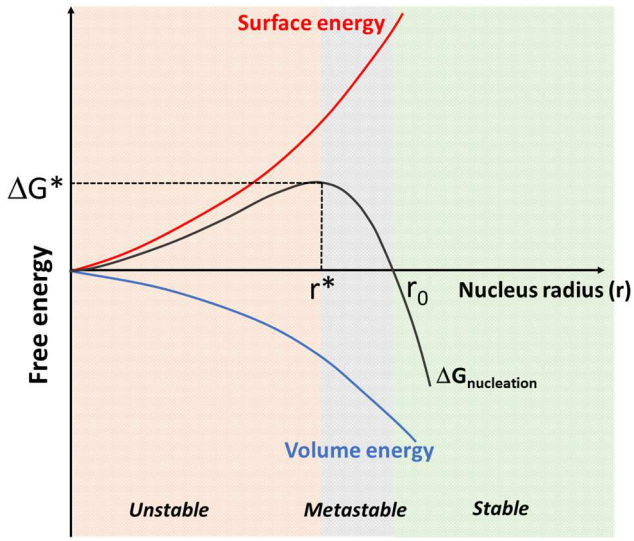

Figure I-8 : Schematic representation of the evolution of the nucleation free enthalpy $\Delta G_{nucleation}$ versus the nucleus radius (r) (black curve). The negative contribution linked to the volume energy and the positive contribution due to the surface energy are represented by blue and red curves respectively. Unstable, metastable and stable domains are colored in orange, grey and green respectively.

However, homogeneous nucleation is rare and is generally admitted at very high supersaturation. In most cases, primary nucleation is *heterogeneous*,[14,15] that is to say that aggregation occurs with the assistance of tiny foreign particles such as dust, or on an interface such as the wall of the reactor, the edges of stirrer, etc.… In the case of heterogeneous nucleation, ΔG* is lower than in homogeneous nucleation.

- Secondary nucleation

By contrast, in the case of secondary nucleation, nuclei form from existing crystals.[16,17] Different mechanisms have been proposed to describe secondary nucleation:[18] (i) *fluid shear nucleation*,[19,20] *i.e.* the shear forces applied by the solution to the crystal surfaces could be sufficient to detach minute amounts of crystalline matter that would in turn act as secondary nucleation sites, (ii) *contact nucleation*, *i.e.* minute amounts of crystalline matter are liberated by crystals scratching each other or against the reactor walls (or the stirrer), and act as support for the nucleation.[17] Since the energy required for secondary nucleation is much lower than for primary nucleation, secondary nucleation is favored over primary nucleation at low supersaturation.[16]

- Seeding

Seeding consists of the voluntary addition of a small amount of crystals (usually as a powder) to a supersaturated solution in order to trigger its crystallization. This method ensures control of the nucleation and crystallization. By seeding a solution with suitable

seeds, it is possible to control the crystal form or the polymorph produced during the process. Moreover, seeding significantly reduces the induction time for crystallization.[21]

3. Crystal Growth

The third step towards crystal formation is crystal growth, the process by which a nucleus grows to become a crystal. As soon as the energy barrier ΔG^* is overcome, the nucleus grows by surface adsorption of the particles available in the solution, *i.e.* the growth units. The solution supplies those particles until it is back to its saturation concentration.

Two different mechanisms were described for the adsorption of the growth units at the crystal solution interface:

- Two dimensional nucleation:[22] For a perfect crystal, *i.e.* without defects at the surface, there is no preferential adsorption sites at the growing crystal surfaces, the growth units mature together and form a two-dimensional nucleus at the crystal-solution interface, which grow in two dimensions, thus expanding the crystal. This mechanism is expected at high supersaturations.
- Spiral growth:[23,24] At lower supersaturation, crystal growth occurs via a screw dislocation (detailed in part I.E.) emerging from the crystal surface. This defect offers a preferential adsorption zone where the growth units can dock on. The adsorption of the growth units follows the dislocation which might result in the appearance of a spiral at the crystal surface.

D. Growth Kinetics

The rate of adsorption of the growth units at the crystal interface depends on intrinsic factors, such as the crystalline structure, the nature of the bonds, the presence of crystal defects, as well as on external factors related to experimental conditions such as the supersaturation (the higher the supersaturation, the faster the crystal growth, due to the higher probability of collisions between crystals and free particles), the temperature, the solvent or the presence of impurities. These factors directly influence the adsorption rate, *i.e.* the crystal growth rate. Also, due to these factors, crystal growth is not isotropic, which leads to a specific morphology of the final crystal *via* the appearance of faces. The growth rate of each crystal face (*i.e.*, facial growth rate) is decisive for the morphology, as the slower the growth rate, the more visible is the face in the final morphology (Figure I-9).

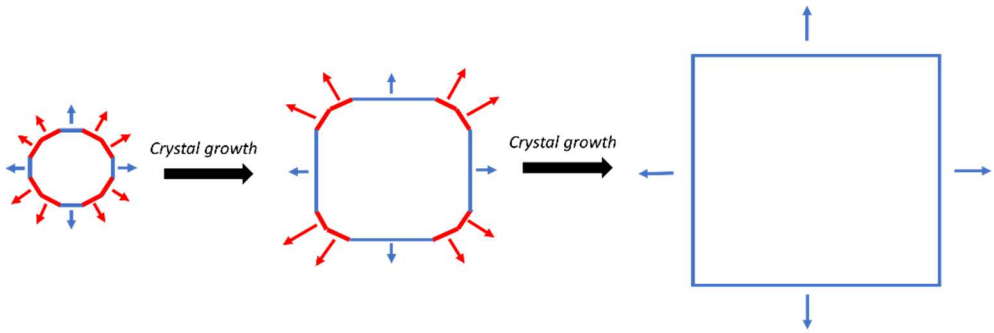

Figure I-9 : From the left to the right, schematic representation of a crystal growth. Red faces grow faster (larger red arrows) than blue ones. The blue faces are prominent one the final habit.

The Kossel model describes three kinds of crystal surfaces offering adsorption sites for growth units: (i) Kinked surfaces (*K* faces) with the highest number of adsorption sites, (ii) Stepped surfaces (*S* faces) and (iii) Flat surfaces (*F* faces) with lesser probability of adsorption (Figure I-10).[25]

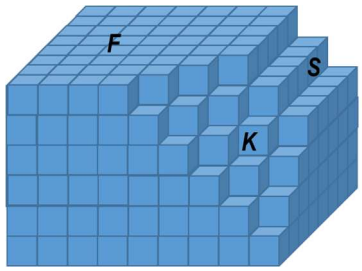

Figure I-10 : Schematic representation of the Kossel Model with kinked faces (K), stepped faces (S) and flat faces (F).

Face growth rates can be estimated by monitoring the development of a face along its normal direction for instance using a microscope. When the crystal growth becomes uncontrolled, *e.g.* in the case of very high supersaturation, the crystal surface becomes more and more rough. This phenomenon is called the roughening transition.[26]

1. Crystal Habit Prediction

Different mathematical models have been developed to predict crystal morphologies.[27] The first one is the Bravais Friedel Donnay Harker (BFDH) model, which is mainly focused on the geometry of the structure (intrinsic factors) to determine the crystal habit and relative growth rates of faces. The BFDH method assumes that the face growth is due to the addition of a molecular layer and that the face growth rate is proportional to $1/d_{(hkl)}$ where $d_{(hkl)}$ is the distance between molecular layer. The thinner this layer, the faster the face growth because the addition of a molecular layer is easier and faster. In many cases, good approximations of crystal habits and identification of the most important faces formed

during growth can be predicted by using the BFDH model. However, as there are no energetic considerations, the stronger the bonds in the crystal state, the less accurate the method.

The Attachment Energy method[28] is more accurate than the BFDH method as such energetic considerations are included. The attachment energy, E_{att} is defined as the energy released when a slice of thickness d_{hkl} is added to the (hkl) face of the growing crystal. E_{att} is the energy of the slice attachment (E_{slice}) withdrawn from the energy of the lattice ($E_{lattice}$) (Equation I-3). The lower E_{att}, the slower the face growth rate.

$$E_{att} = E_{lattice} - E_{slice} \qquad \textit{Equation I-3}$$

The Hartman-Perdok method relies on the Periodic Bond Chains (PBCs) theory. It states that a crystal is more stable when a constituting unit can form long uninterrupted periodic chains. PBCs are constructed by means of a strong crystal bonds. A two-dimensional connected net is created by the intersection of non-parallel PBCs and constitute a stable face. According to the dimension of the PBCs formation, 0, 1 or 2 for two-dimensional nets correspond to *K*, *S*, and *F* faces respectively (Figure I-10). The higher the dimension of the PBCs formation, the more stable the corresponding face is and the slower its growth.[29] Then, F faces are the most visible whereas K faces are the least represented ones in the final habit of the crystal.

2. Growth Kinetics in the Presence of Impurities

As the face growth rate depends on the interaction with the environment, *i.e.* the solution, the presence of other compounds may change these interactions and modify the growth rate, the morphology and the crystal size distribution.

First, the presence of an impurity can change the interfacial energy, *i.e.* the affinity between the solute and the solvent. It may result in a solubility increase (or decrease) and possibly an increase of the metastable zone width defined by the Ostwald limit (Figure I-7).[30–32]

The kinetics of the system could also be changed by a modification of the crystal growth rate. Indeed, adsorption of impurities at the crystal surface can block the growth sites which are no longer available for the growth unit. According to the impurity concentration and to the adsorption rate, the crystal growth can be slowed down or even stopped.[33]

Two cases are encountered according to the affinity between impurity and solute: (i) the reversible adsorption, where the crystal growth rate is decreased and (ii) the irreversible

adsorption, where additives are progressively included in the crystalline structure and can form a solid solution.

The affinity between impurity and solute, most often due to geometric similarities, along specific faces impacts their relative growth rate and, further, the whole crystal growth (Figure I-11) The resulting habit can therefore be considerably changed.

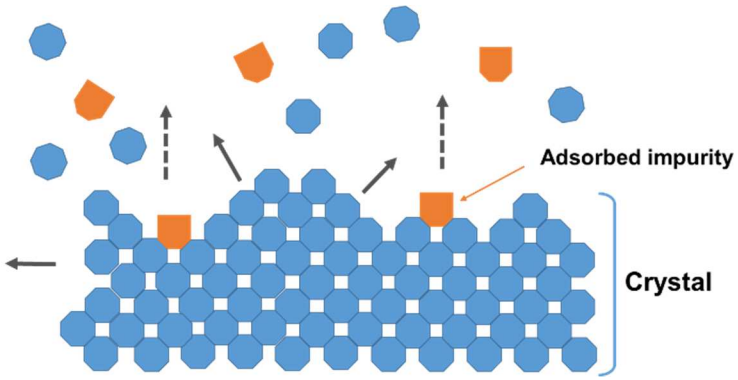

Figure I-11 : Schematic representation of impurity adsorption on the crystal surface. The crystal growth is impacted by the impurity alongside specific directions. Face growth not impacted and face growth hindered by the impurity are represented by solid arrows and dashed arrows, respectively.

Using this phenomenon, morphology or size can be controlled by the suitable use of a tailor-made impurity, called additives in this context.[34–36]

3. Ostwald Ripening

By means of the dissolution – crystallization dynamic equilibrium occurring between the crystal and the saturated solution as well as diffusion, the crystals in a saturated solution undergo a ripening phenomenon where the smaller crystals are dissolved in favor of the growth of the larger ones. This is related to the Gibbs-Thomson effect which states that small particles have a higher solubility than large ones. Indeed, in order to minimize interfacial energy, smaller crystals are dissolved in the favor of the growth of larger crystals.[37,38] This phenomenon is called Ostwald ripening.[39] Ostwald ripening can also occur in dry conditions when two crystals are put in contact, although it is far less effective.

E. Defects in Crystals

During crystal growth, stacking faults may occur leading to defects and irregularities in the crystalline structure. Actually, a perfect single crystal almost does not exist and crystal defects are always present in a real crystal. The different types of defects are described according to their dimension.

Point defects (0D): These types of defects have the dimension of the crystal constituents. It could be a "vacancy", where a growth unit is missing in the crystal structure.[40] In contrast, a "self-interstitial" is an additional constituent occupying an interstitial site of the crystalline structure.[40] The deformation of the structure and the associated energy caused by self-interstitial defects is more important than a vacancy, which makes them rare, especially in molecular crystals. Another type of point defect is the substitution of an atom, molecule or ion by a foreign substance, considered as an impurity. Such defects give rise to a solid solution.[41]

Linear defects (1D):[42] Linear defects could be either "edge dislocations" or "screw dislocations". Concerning edge dislocations, a part of a crystallographic plane is missing. The neighboring crystallographic planes loosen up to fill the space where the plane is missing. For screw dislocations, the dislocations shift the crystallographic plane perpendicular to the direction of the plane. Screw dislocations can initiate the spiral growth mechanism.

Surface defects (2D): These defects occurs at the surface of a crystal. The main surface defects are grain boundaries, stacking faults and twinning.

- Grain boundaries are the result of more or less important misorientation between two (or more) crystal sections, *i.e.* grains. Grains are linked by grain boundaries at which some particles belong to both grains. The lower the misorientation, the more particles are shared between the grains.[43] When the coherence between the different grains is high over the whole volume of the crystal, the term "crystal mosaicity" is sometimes used.
- Stacking faults are disruptions in the crystalline structure along molecular or atomic planes where the normal order of succession into atomic planes is not respected.[44]
- A specific case is that of twin crystals, which are 'a *symmetrical reorientation of parts or of a crystal as a whole*.'[45] Two grains of the twin crystal share a common reticular plane and the symmetry of the packing is respected all along the twinning plane.[46]

Inclusions (3D): During crystal growth, entrapment of macroscopic amounts of a foreign substance can occur. This foreign substance can be either gaseous matter or supersaturated solution (inclusions). The properties of the crystal is obviously affected by these inclusions.[47]

II. Chirality

A. Definition

From the Greek word 'kheir', meaning hands, chirality is the particular ability of one object to exist in two opposite configurations, mirror image related, such as our hands. Molecules, or arrangements of molecules, presenting two mirror image related configurations are known as chiral and each configuration is an *enantiomer*.[48]

B. Enantiomer Properties

1. Physical-Chemical Properties

Two enantiomers have the same scalar properties such as melting point, density, solubility (in achiral media), ability to present polymorphism, refractive index, spectra (IR, X-Ray, RMN…).[49]

However, they have different vector properties, not in terms of magnitude, but in terms of sign. Indeed, their optical properties, notably the optical rotation of polarized light are strictly opposite. One enantiomer deviates the plane of polarized light to the right (clockwise), it is *dextrogyre,* noted *d* or (+). The counter enantiomer deviates the plan of polarized light, with the same deviation degree, to the left (anti-clockwise) and is *levogyre*, noted *l* or (-). Thus, based on the deviation of the plane of polarized light, the polarimetric methods, circular dichroism or polarized light microscopy, are good methods to distinguish enantiomers and to determine the proportions of each of them in a system.[49]

2. Biological Properties and API

The building blocks of biological organisms, *i.e.* all living things (made of proteins, sugars, amino acids…), are chiral. This makes them particularly sensitive to stereochemistry, as interactions between chiral compounds and chiral receptors are different according to the concerned enantiomer (Figure I-12).[50] Thus, the biological properties of two opposite enantiomers are often different.

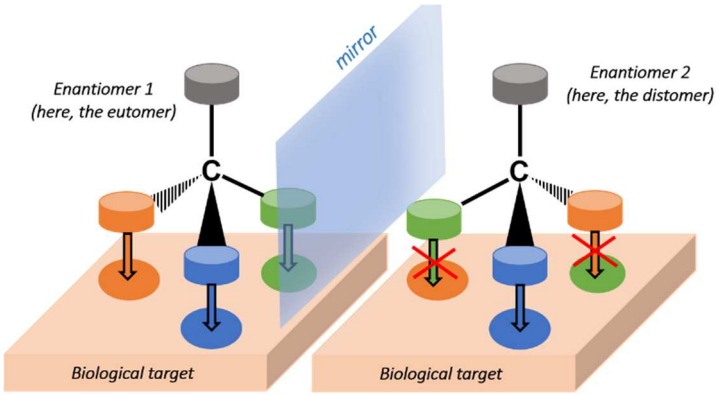

Figure I-12 : Schematic representation of the interaction between a chiral biological receptor (Biological target) and a chiral compound (enantiomers 1 and 2). The enantiomer 1 is compatible with the biological target, it is the eutomer (right), while the enantiomer 2 is not suitable, it is the distomer (left).

In this context, the Food and Drug Administration (FDA, USA) and authorities in Europe, China and Japan require the use of the active compound alone, *i.e.* the active enantiomer (also called *the eutomer*, designated as the desired enantiomer) for the commercialization of the active pharmaceutical ingredient (API)[51,52] since the counter enantiomer (the unwanted enantiomer, called *the distomer*) could be inactive or toxic.[53] Therefore, the distomer is now considered as an impurity and has to be eliminated.

3. Heterogeneous Equilibria between Enantiomers

Crystallization of a system composed of two enantiomers can lead to three main types of equilibria.[54]

- Racemic compound (Figure I-13-a): In most cases (90-95%), crystallization of the two enantiomers results in a *racemic compound,* also named a *racemate*. This stoichiometric compound is made of the two enantiomers in equal proportions and presents a crystalline structure different from the crystalline structure of the pure enantiomer.

The term racemic composition should be differentiated from the term racemic compound. Racemic composition corresponds to 50% of both enantiomers, whatever the crystallographic configuration.

- Conglomerate (Figure I-13-b): In 5-10% of cases, both enantiomers do not crystallize together. Crystallization leads to a physical mixture of both enantiomers.

- Solid solution: If partial or total miscibility in the solid state between enantiomers is possible, then they form a solid solution by substitution, partial (Figure I-13-c) or complete (Figure I-13-d).

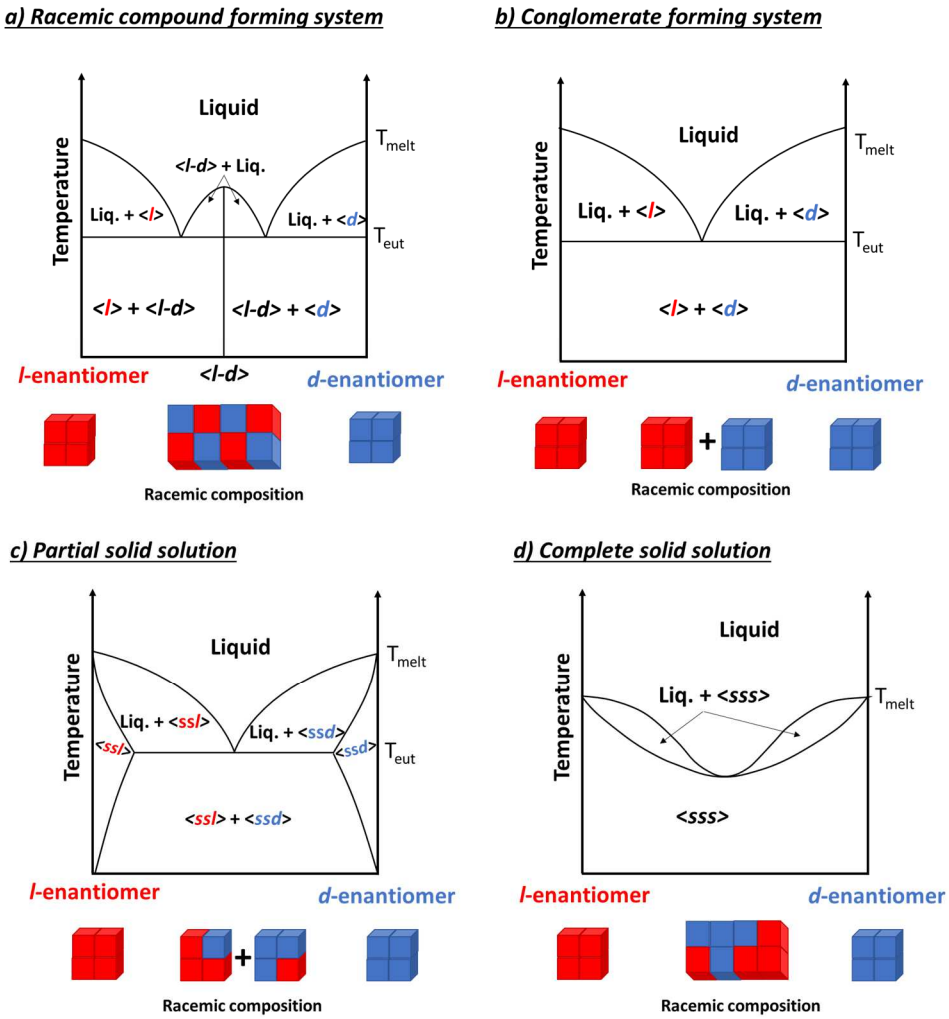

Figure I-13 : Schematic representation of three main cases encountered in heterogeneous equilibria between enantiomers: a) the formation of a racemic compound (<l-d>), b) the conglomerate forming system, c) the formation of partial solid solutions (<ssl> and <ssd>) and d) the complete solid solution by substitution (sss) between enantiomers. The schematic crystals present at the racemic composition are represented below each case.

In the present work, the system investigated crystallizes as a conglomerate of enantiopure particles, although the situation is complexified by the loss of chirality in the liquid state or in solution (see below in Section C-4)

4. Enantiomeric Excess

The quantification of both enantiomers in a system is commonly described by the *enantiomeric excess* (*ee*). This value determines the percent deviation from the racemic

mixture, for which the *ee* equals 0 %. Thus, the *ee* determines the absolute difference between the proportions of enantiomers, following Equation I-4, where n_d and n_l are the amount (in mol or mass) of *d*-crystals and *l*-crystals respectively. No sign is included in this equation, and the predominant enantiomer has to be identified. In order to avoid confusion, a sign of *ee* can be determined, following the modified Equation I-5. Using this equation, a positive *ee* means that *d*-enantiomer predominates and conversely.[55]

$$ee(\%) = \frac{|n_d - n_l|}{n_d + n_l} * 100 \qquad \textit{Equation I-4}$$

$$ee(\%) = \frac{n_d - n_l}{n_d + n_l} * 100 \qquad \textit{Equation I-5}$$

In the case of a solid sample, the crystal enantiomeric excess (CEE) is determined with n_d and n_l correspond to the mass or the number of *d*-crystals and *l*-crystals respectively (Equation I-6).

$$CEE(\%) = \frac{n_d - n_l}{n_d + n_l} * 100 \qquad \textit{Equation I-6}$$

C. Classification of Chirality

Chirality in chemistry materializes differently. It could be directly related to the intrinsic molecular structure (configurational or conformational chirality)[56] or to the packing of several molecules.

1. Molecular Chirality due to the Presence of an Asymmetric Center

The most common type of chirality described in undergraduate textbooks is the chirality induced by the presence of a stereogenic atom in the molecule, and even more commonly a stereogenic carbon which has four different substituents. Two arrangements of the four different substituents are possible: these are the two opposite configurations of the two enantiomers of the molecule (Figure I-14). The chirality is said to be “configurational”, as a covalent bond between the chiral center and one of the four constituent has to be broken to obtain the second enantiomer.[56]

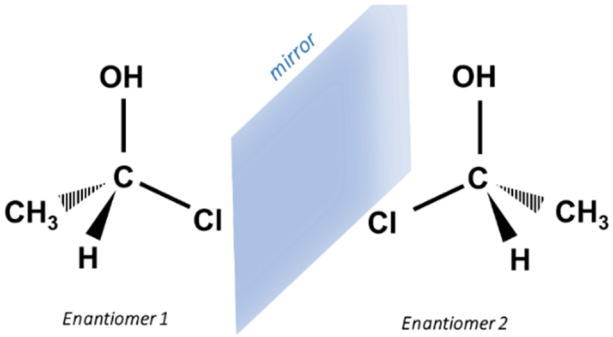

Figure I-14 : Both enantiomers of a chiral molecule with a stereogenic carbon bonded to four different substituents.

Different notations are used to label each enantiomer. Enantiomers can be labelled either R (*rectus*) and S (*sinister*) according to the Cahn, Ingold and Prelog priority rules, or L and D (commonly used for amino acids), according to the Fisher projection's rule. L and D are not related to the levogyre / dextrogyre character of the molecule.[57] *l* and *d* (in lowercase) (or (-)/(+)), is the only notation related to the optical deviation of the polarized light.

2. Diastereomery

When the molecule has more than one stereogenic center, the number of possible configurations, *i.e.* the number of stereoisomers is 2^n, with n, being the number of stereogenic centers. Stereoisomers with exactly opposed stereogenic centers are enantiomers, other configurations are diastereomers (Figure I-15).[56]

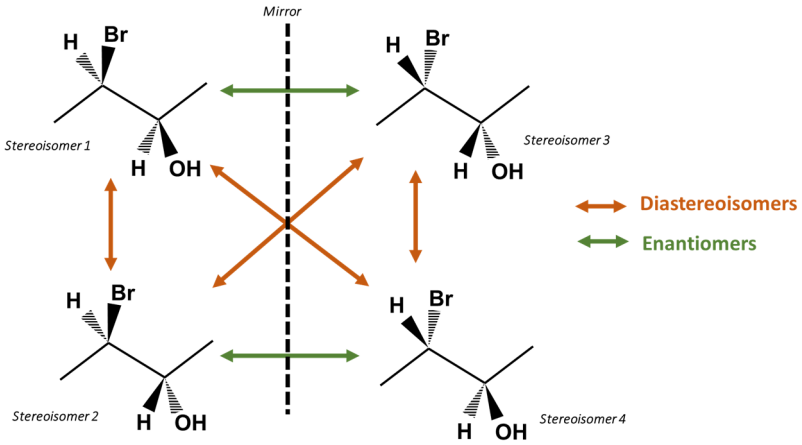

Figure I-15 : Relation between four stereoisomers of a molecule with two stereogenic centers.

3. Atropisomery

Atropisomerism was discovered in 1922 by Christie and Kenner.[58] These authors described the '*optical activity due to axial chirality*', and later on the term of "atropisomer" was coined by Kuhn in 1933.[59] Atropisomers are planar molecules whose conformation is

hindered by the absence of free rotation around a single bond.[48] The interconversion from one to the second atropisomer does not require a chemical reaction, *i.e* no breakage of chemical bonds, a suitable energy flux such as temperature, can be sufficient to change the conformation of the molecule (Figure I-16).

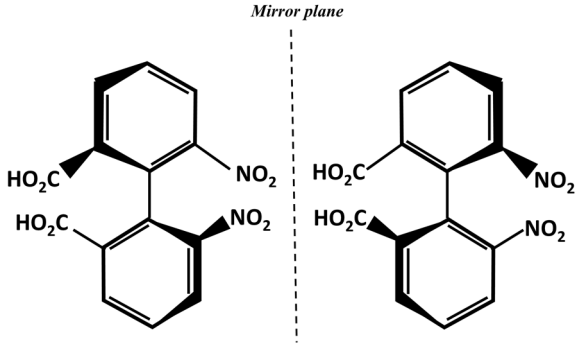

Figure I-16 : Atropisomers of 6,6'-dinitro-2,2'-dicarboxybiphenyl

4. Supramolecular Chirality

Achiral compounds, *i.e.* optically inactive compounds, can actually crystallize in one of the 65 chiral space groups. While these compounds are fully optically inactive in the liquid or dissolved state, their crystallization leads to optically active crystals, *i.e.* chiral crystals. For instance, helical assemblies of achiral groups of molecules can afford chirality by means of clockwise or anticlockwise rotations. A good example of supramolecular chirality is quartz (SiO_2). Indeed, β-quartz crystallizes either in the $P6_421$ or $P6_221$ SG depending on the handedness of the molecular arrangement around the 6-fold axis. The same holds for the low temperature form, α-quartz, which crystallizes either in the $P3_221$ or $P3_121$ SG. Two opposite enantiomorphs are therefore described for each polymorph.[60,61] While the difference between 6_2 and 6_4 or between 3_1 and 3_2 screw axes is easy to grasp, it is harder to recognize that a clockwise or anticlockwise rotation around a 2_1 screw axis can also give rise to a chiral supramolecular arrangement (Figure I-17-a)-b))[62,63] In this context, the supramolecular chirality occurring in the crystalline state for sodium chlorate ($NaClO_3$), which crystallizes in $P2_13$, has been well known since the work of Kipping and Pope (Figure I-17-c)).[64]

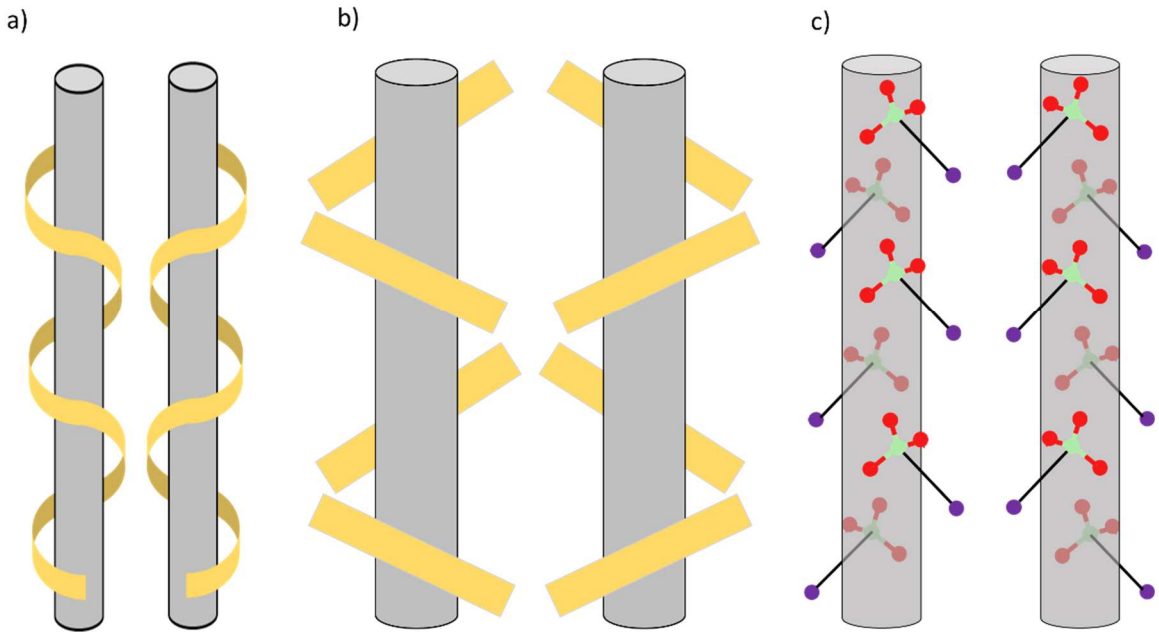

Figure I-17 : Schematic representation of chirality generation via 2_1 assemblies of a) helix, b) bars and c) sodium chlorate crystal structure.

To distinguish each supramolecular enantiomer it is necessary to perform the analyses in the solid state, as the chirality is entirely lost in the liquid or solvated state (Figure I-18). Different methods are feasible for the characterization of solid state chirality such as X-ray single crystal analysis, careful observation of the morphology of the crystals (two macroscopic single crystals of two opposite enantiomorphs are mirror image related), circular dichroism (of a KBr pellet or Nujol mull) or polarized light microscopy (each enantiomorph will behave differently).[65]

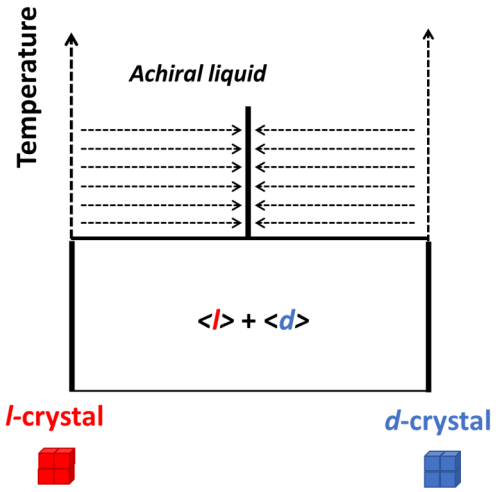

Figure I-18 : Degenerated binary phase diagram of achiral compounds forming chiral crystals. Due to the absence of chirality at the liquid state, dashed areas are not accessible.

D. Access to Pure Enantiomers

1. Stereoselective Synthesis of the Desired Enantiomer

- Chiral pool synthesis:[66] Synthesis of a chiral compound using readily available chiral building blocks from a well-known set of natural chiral substances (the chiral pool), such as amino acids or sugars.
- Asymmetric synthesis:[67] Starting from an achiral precursor, the synthesis is enantioselective by means of a chiral environment, such as a chiral auxiliary or chiral catalyst, which is able to control the stereogenic center in the desired product.

When stereoselective synthesis is not possible, the synthesis is non-stereoselective and gives rise to a racemic mixture from which the enantiomers have to be resolved, i.e. separated.

2. Resolutions of Enantiomers

Resolution is the separation of enantiomers from a racemic or enantio-enriched mixture. For this purpose, several methods can be envisaged.

- Chiral chromatography

Chiral chromatography was first used as an analytical method and then developed as a preparative method. The two enantiomers interact differently with the chiral stationary phase so that their retention times are different. Thus, enantiomers are separated at the end of the chromatographic column.[68]

Alternatively, many resolution methods based on crystallization were developed, such as Pasteurian Resolution, Preferential Crystallization, Second Order Asymmetric Transformation, Preferential Enrichment and Deracemization.

- Pasteurian resolution

This method relies on the different physical-chemical properties between two diastereomers. By the addition of an enantiopure reagent, the two enantiomers form two different diastereomers.[64,69] As they have different physical-chemical properties, and particularly a different solubility, they can be easily separated by a selective crystallization step. Diastereomers have to be transformed back into the enantiomers,

usually by a salting out procedure. While the yield is never 100%, this method is reliable and workable either at the laboratory as well as at the industrial scale.

- Preferential crystallization (PC)

Efficiency of the preferential crystallization (PC) method relies on chiral discrimination in the solid state. The prerequisite for the establishment of PC is the presence of a stable conglomerate between the two enantiomers. Racemic compound or complete solid solution type systems are therefore excluded, but partial solid solutions and metastable conglomerates might be acceptable. This method relies on the kinetic stereoselective crystallization of one enantiomer from a supersaturated solution, triggered by suitable seeding.[70,71] The enantiomer in excess crystallizes by entrainment and is collected. Three different methods were described based on this process: Seeded Isothermal Preferential Crystallization (SIPC),[70,72] Seeded Polythermal Programmed Preferential Crystallization (S3PC)[72] and Auto-Seeded Polythermal Programmed Preferential Crystallization (AS3PC).[73]

The limit of PC is the yield; the theoretical maximum yield cannot exceed 50 % since, particularly in the context of the API production, the counter enantiomer is defined as an impurity and is not converted into the desired one. To tackle this problem, racemization in solution was considered in order to improve PC, which leads to the second-order asymmetric transformation.

- Second-Order Asymmetric Transformation (SOAT)[74]

Resolution by SOAT combines PC and racemization in solution, *i.e.* the interconversion between enantiomers during the process.[71] During the crystallization of one enantiomer, the counter enantiomer, in excess in solution, is converted into the desired one. Since the enantiomeric excess in solution is continuously reset to 0 % by racemization, SOAT does not rely on a kinetic state which avoids the crystallization of the counter enantiomer. SOAT was described by Jamison *et al.*[75] for diastereomers and recently described for atropisomers by Oketani *et al.*.[76] By means of racemization in the liquid phase, the yield can be increased up to 100 % *ee* in the solid phase.

- Preferential enrichment (PE)[77]

In the PE process, the liquid phase will be highly enriched during crystallization, while the deposited crystals will remain close to the racemic composition, conversely to other methods.[78,79] It can be described as the opposite process of PC.[78] From a highly supersaturated solution ($4 \leq \beta \leq 25$), slightly enriched, PE occurs in stagnant conditions

and requires a non-stoichiometric racemic compound, *i.e* a partial solid solution. A stereo oriented exchange occurs between the deposited crystals and the mother liquor, giving a high *ee* in the mother liquor and a slight *ee* of the counter enantiomer in the deposited crystals.[80]

- Deracemization

Deracemization is another process enabling access to 100 %*ee* in the solid phase. This method is detailed in the next section.

III. Deracemization and Spontaneous Symmetry Breaking

As for SOAT, deracemization combines racemization in solution and auto-amplification of slight enantiomeric imbalances in the solid phase. A pure enantiomer is collected in the solid phase and the composition of the liquid phase remains racemic by means of racemization. The significant difference with other crystallization methods is the presence of a racemic mixture of crystals in contact with a saturated solution at the beginning of the process.

Deracemization is only applicable to conglomerate forming systems and requires relatively fast racemization in solution. Racemization of chiral compounds can be performed by a chemical reaction (*e.g.* using a strong base) but can also be due to the achiral nature of the compound in case of supramolecular chirality.[81,82]

A. Discovery of Spontaneous Symmetry Breaking in a Suspension

In 1954, Havinga[81] highlighted the possibility to perform symmetry breaking of chiral systems by crystallization, provided three required conditions are met: (i) no racemic compound formation between both enantiomers, (ii) the substance must be racemized in solution and (iii) crystal growth is faster than the formation of crystal nuclei.

In 1990 (one century after the description of the enantiomorphism of $NaClO_3$ by Kipping and Pope)[64], Kondepudi *et al* showed the possible stereoselectivity of the crystallization of sodium chlorate ($NaClO_3$) *under stirring* – while unstirred solution gave rise to a perfect racemic mixture in the deposited crystals.[83] The *mother crystal theory* was put forward to

explain this phenomenon:[84–86] In this theory, the chirality of the first crystal appearing in the solution, *i.e.* the *mother crystal*, guides the chirality of all other crystals, *i.e.* daughter crystals. Kondepudi *et al.* and Martin *et al.* highlighted the importance of the stirring to enhance secondary nucleation for total symmetry breaking.[87,88] However, if the crystallization is performed in stagnant conditions, the occurrence of both enantiomorphs at the end of the process results from multiple nucleation events. $NaClO_3$ fulfills Havinga's condition: (i) there is no racemic compound or solid solution formation, (ii) $NaClO_3$ is instantaneously racemized in solution as there is no chirality in the liquid state and (iii) secondary nucleation is favored over primary nucleation by means of low supersaturation.

Later, Viedma showed that concerning crystallization of $NaClO_3$ from highly supersaturated solution, the appearance of the mother crystal is not sufficient to decrease the supersaturation and cannot avoid primary nucleation elsewhere in the medium. These experiments resulted in racemic mixtures, due to uncontrolled primary nucleation in the process. However, he observed that if the obtained racemic suspensions are left two days under stirring, then the deposited crystals systematically become fully enantiopure. Therefore, the theory of the mother crystal was reconsidered.[89]

From these observation, Viedma performed experiments from racemic suspensions, *i.e.* crystals in equilibrium with saturated solution, of $NaClO_3$ in water and showed the fast (*i.e.*, <12h) total symmetry breaking when stirred in the presence of glass beads.[90] This experiment definitely invalidated the theory of the mother crystal as crystals of both chiralities were present at the beginning of the experiment. Then, total symmetry breaking occurs *via* matter exchange between crystals and the saturated solution. From there, deracemization was developed as a preparative process.

B. Attrition Enhanced Deracemization, Viedma Ripening

After Viedma's discovery of $NaClO_3$ total symmetry breaking upon grinding the suspension, the technique of deracemization by attrition, *i.e.* attrition-enhanced deracemization, now called *Viedma ripening*,[91] has been successfully applied to many chiral organic compounds,[82,92] including stereoisomers[93] and atropisomers,[94] and to other achiral compounds crystallizing in chiral space groups.[95,96]

1. Principle

From racemic crystals in equilibrium with their saturated solution, matter exchanges between liquid and solid phases at the steady state are continuous. Spontaneous symmetry breaking occurs randomly due to local fluctuations of the *ee* or of the crystal size distribution (CSD) between enantiomers.[91] Total symmetry breaking occurs *via* an auto-catalytic amplification of these slight stochastic imbalances towards an enantiopure end state. Ostwald ripening and attrition are interdependent factors favoring total symmetry breaking (Figure I-19). As a result of the Gibbs Thomson effect,[97] Ostwald ripening leads to dissolution of smaller crystals in favor of the growth of the larger ones. Thus, from a CSD difference between enantiomers, small crystals (schematically represented as blue crystals in Figure I-19) are dissolved, racemized at the solvated state and recrystallized as bigger crystals (schematically represented as red crystals in Figure I-19). Attrition ensures continuous production of smaller crystals feeding Ostwald ripening and chiral clusters which are re-incorporated stereo-specifically in bulk crystals. Indeed, attrition and Ostwald ripening ensure a continuous *crystal recycling* towards total deracemization.[90,98]

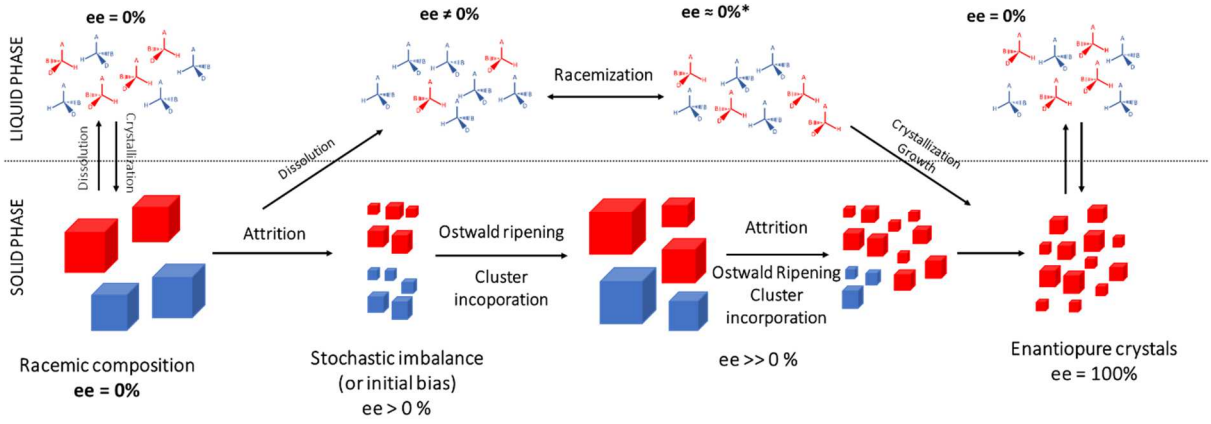

*Figure I-19: Schematic representation of deracemization mechanisms of chiral molecules, as a general case by Viedma ripening. *A very small enantiomeric excess of the opposite sign can exist in the solution during the process.*[81,99]

2. Mathematical Models

Although still under development, mathematical models reported in the literature support the explanation of the Viedma ripening mechanism. Models were based on different key factors such as Ostwald ripening, attrition and chiral cluster re-incorporation. First, Saito *et al*. and Uwaha *et al.* affirmed the importance of the presence of chiral clusters and their incorporation to describe the autocatalytic mechanism of deracemization.[98,100–102]

Additionally, Cartwright *et al.* and Noorduin *et al.* stated that Ostwald ripening coupled with attrition are essential factors to reach homochirality.[38,82,103] Finally, the authors agreed on the concomitant effects of these three critical factors, *i.e.* attrition, Ostwald ripening and the presence of chiral clusters, for the achievement of total symmetry breaking in an autocatalytic way.[104]

C. Temperature Cycling Induced Deracemization

Besides experiments on attrition-enhanced deracemization, Viedma et al. considered the impact of temperature fluctuations on symmetry breaking experiments for amino acids or for $NaClO_3$.[105,106] Indeed, they have shown that the temperature gradient between the hot bottom, in contact with a hot stirring plate, and the colder top of a flask containing $NaClO_3$ crystals in suspension hastens crystal ripening and symmetry breaking. In the case of amino acid deracemization, the temperature gradient used was combined with attrition by glass beads: the larger the temperature gradient, the faster the induction time and total symmetry breaking.[105] However, in the case of $NaClO_3$ deracemization, there were no glass beads and no stirring in the system, symmetry breaking was only ensured by the temperature gradient and boiling of the suspension, which enables circulation of crystals between the hot bottom and cold top.[106] Based on these considerations, Suwannasang *et al*. experimented with controlled temperature fluctuations for total symmetry breaking.[107] These authors studied different cooling rates and temperature ranges and showed successful deracemization of organic chiral compounds by temperature cycling. Later on, members of an ongoing European project (CoRe project, focused on continuous resolution)[108] also studied *Temperature Cycling Induced Deracemization* (TCID) and investigated different key factors such as cooling rate, temperature range and racemization rate.[109–111]

1. Principle

Controlled temperature cycles are repeatedly applied to a racemic mixture of crystals in equilibrium with their saturated solution. Upon oscillating temperature and from local fluctuations of *ee* or CSD (as in Viedma ripening) a slight stochastic imbalance occurs between enantiomers. During heating, crystals are partially dissolved and during cooling, crystal growth and/or secondary nucleation occur. Thus, cyclic dissolution-recrystallization events provide an efficient crystal recycling and an overall similar autocatalytic effect as for Viedma ripening, where Ostwald ripening is enhanced by the

repetitive heating and cooling steps. Incorporation of chiral clusters has been proposed to explain the autocatalytic character of the process, observed in TCID experiments, as in Viedma ripening.[112] Other authors suggested that the crystal growth rate dispersion of the two populations of crystals might be an important factor in the outcome of TCID.[113] So far, no fully satisfactory TCID mechanism has been proposed, however, the influences of parameters were studied such as the amplitude of the temperature oscillation, the cooling rate and the racemization rate. It has been shown that the amount of crystals dissolved per cycle has to be sufficient to trigger symmetry breaking. Therefore, temperature dependence of the solubility will determine the suitable temperature range, *i.e.* between the highest and lowest temperature of the cycle.[110] Study of the impact of cooling rate shows that the deracemization time is not necessarily reduced by faster cooling rates since more cycles are then required.[107] The racemization rate in the mother liquor also influences the time required for deracemization: the faster the racemization, the faster the deracemization.[109,111]

It is also worth noting that damped temperature cycles can improve the efficiency of TCID. Indeed, once symmetry breaking is established, the duration of a temperature cycle can be decreased by damping its highest temperature while maintaining other parameters constant (heating/cooling rates and the lowest temperature). The required cycle number remains the same, but cycles are then faster, inducing faster deracemization.[114]

2. Mathematical Models

Crystal growth and Ostwald ripening are central factors for TCID. Consequently, many mathematical models are focused on the difference of crystal growth rate between each enantiomer (*e.g.* due to initial formation of nuclei at different times) to describe the stochastic symmetry breaking.[113,115] While incorporation of chiral clusters was also considered as in Viedma ripening to explain the autocatalytic character of the mechanism,[112] stereoselective agglomeration should not be essential in TCID.[116] Mathematical models have confirmed the influence of the cooling rate[116] and initial asymmetry, in CSD or *ee*, which guides the direction of deracemization.[116–118]

D. Other Methods

Other energy fluxes were investigated to deracemize a racemic suspension. Indeed, ultrasound[119,120] or microwave[121] are possible ways to induce total symmetry breaking.

Moreover, different methods have been investigated to improve and direct deracemization. It was found that the addition of chiral impurities in a chiral system, in a TCID or Viedma ripening process,[122,123] enables a shift in deracemization towards the desired enantiomer. A similar effect was discovered upon application of circularly polarized light.[124]

References

1. Hancock, B. C. & Zografi, G. Characteristics and Significance of the Amorphous State in Pharmaceutical Systems. *J. Pharm. Sci.* **86**, 1–12 (1997).

2. Threlfall, T. L. Analysis of organic polymorphs. A review. *Analyst.* **120**, 2435–2460 (1995).

3. Haleblian, J. & McCrone, W. Pharmaceutical applications of polymorphism. *J. Pharm. Sci.* **58**, 911–929 (1969).

4. Lowell, C. E. Solid Solution of Boron in Graphite. *J. Am. Ceram. SOC.* **50**, 142–144 (1967).

5. Shan, N. & Zaworotko, M. J. The role of cocrystals in pharmaceutical science. *Drug Discov. Today.* **13**, 7 (2008).

6. Bond, A. D. What is a co-crystal? *CrystEnComm.* **9**, 833–834 (2007).

7. Aakeröy, C. B., Fasulo, M. E. & Desper, J. Cocrystal or Salt: Does It Really Matter? *Mol. Pharmaceutics.* **4**, 317–322 (2007).

8. Koster, G. F. Space groups and their representations. *Solid States Phys.* **5**, 173–256 (1957).

9. Flack, H. D. Chiral and Achiral Crystal Structures. *HCA.* **86**, 905–921 (2003).

10. Lindenberg, C., Krättli, M., Cornel, J., Mazzotti, M. & Brozio, J. Design and Optimization of a Combined Cooling/Antisolvent Crystallization Process. *Cryst. Growth. Des.* **9**, 1124–1136 (2009).

11. Ostwald, W. Studien über die Bildung und Umwandlung fester Körper. *Z. Phys. Chem.* **22U**, 289–330 (1897).

12. Ting, H. Huai. & McCabe, W. L. Supersaturation and Crystal Formation in Seeded Solutions. *Industrial & Engineering Chemistry.* **26**, 1201–1207 (1934).

13. Garside, J. Nucleation. in *Biological Mineralization and Demineralization* vol. 23 23–35 (G.H. Nancollas, 1982).

14. Langhma, E. J. & Mason, B. J. The heterogeneous and homogeneous nucleation of supercooled water. *Proc. R. Soc. Lond. A.* **247**, 493–504 (1958).

15. Liu, X. Y. Heterogeneous nucleation or homogeneous nucleation? *J. Chem. Phys.* **112**, 9949 (2014).

16. Agrawal, S. G. & Paterson, A. H. J. Secondary Nucleation: Mechanisms and Models. *Chem Eng Commun.* **202**, 698–706 (2015).

17. Garside, J. & Davey, R. J. Secondary contact nucleation: Kinetics, growth and scale up. *Chem Eng Commun.* **4**, 33 (1980).

18. Evans, T. W., Margolis, G. & Sarofim, A. F. Mechanisms of secondary nucleation in agitated crystallizers. *AIChE Journal.* **20**, 950–958 (1974).

19. Denk Jr, E. G. & Botsaris, G. D. Fundamental studies in secondary nucleation from solution. *J. Cryst. Growth.* **13**, 493–499 (1972).

20. Sung, C. Y., Estrin, J. & Youngquist, G. R. Secondary nucleation of magnesium sulfate by fluid shear. *AIChE Journal.* **19**, 957–962 (1973).

21. Chung, S. H., Ma, D. L. & Braatz, R. D. Optimal seeding in batch crystallization. *Can. J. Chem. Eng.* **77**, 590–596 (1999).

22. Liu, X. Y., Maiwa, K. & Tsukamoto, K. Heterogeneous two-dimensional nucleation and growth kinetics. *J. Chem. Phys.* **106**, 11 (1997).

23. Jackson, K. A. *Kinetic processes: crystal growth, diffusion, and phase transitions in materials*. (Wiley-VCH, 2004).

24. Amelinckx, S. Spiral growth on carborundum crystal faces. *Nature*. **167**, 939–940 (1951).

25. Mullin, J. W. *Crystallization*. (Elsevier, 2001).

26. Hartman, P. & Bennema, P. The attachment energy as a habit controlling factor. *J. Cryst. Growth*. **49**, 145–156 (1980).

27. Docherty, R., Clydesdale, G., Roberts, K. J. & Bennema, P. Application of Bravais-Friedel-Donnay-Harker, attachment energy and Ising models to predicting and understanding the morphology of molecular crystals. *J. Phys. D: Appl. Phys.* **24**, 89–99 (1991).

28. Clydesdale, G. *et al.* Prediction of the Polar Morphology of Sodium Chlorate Using a Surface-Specific Attachment Energy Model. *J. Phys. Chem. B.* **102**, 7044–7049 (1998).

29. Woensdregt, C. F. Hartman–Perdok theory: influence of crystal structure and crystalline interface on crystal growth. *Faraday Discuss.* **95**, 97–107 (1993).

30. Sangwal, K. Effects of impurities on crystal growth processes. *Prog. Cryst. Growth Charact. Mater.* **32**, 3–43 (1996).

31. Sangwal, K. & Mielniczek-Brzóska, E. Effect of impurities on metastable zone width for the growth of ammonium oxalate monohydrate crystals from aqueous solutions. *J. Cryst. Growth.* **267**, 662–675 (2004).

32. Titiz-Sargut, S. & Ulrich, J. Influence of Additives on the Width of the Metastable Zone. *Cryst. Growth Des.* **2**, 371–374 (2002).

33. Rauls, M., Bartosch, K., Kind, M., Kuch, St., Lacmann, R., Mersmann, A., *et al.* The influence of impurities on crystallization kinetics: a case study on ammonium sulfate. *J. Cryst. Growth.* **213**, 116–128 (2000).

34. Weissbuch, I., Popovitz-Biro, R., Lahav, M., Leiserowitz, L., Understanding and control of nucleation, growth, habit, dissolution and structure of two-and three-dimensional crystals using tailor-made' auxiliaries. *Acta. Cryst. B.* **51**, 115–148 (1995).

35. Addadi, L. *et al.* Growth and Dissolution of Organic Crystals with Tailor-Made Iinhibitors Implications in Stereochemistry and Materials Science. *Angew. Chem. Int. Ed. Engl.* **24**, 466–485 (1985).

36. Weissbuch, I., Addadi, L. & Leiserowitz, L. Molecular Recognition at Crystal Interfaces. *Science.* **253**, 637–645 (1991).

37. Noorduin, W. L., Vlieg, E., Kellogg, R. M. & Kaptein, B. From Ostwald Ripening to Single Chirality. *Angew. Chem. Int. Ed.* **48**, 9600–9606 (2009).

38. Noorduin, W. L. *et al.* Explanation for the Emergence of a Single Chiral Solid State during Attrition-Enhanced Ostwald Ripening: Survival of the Fittest. *Cryst. Growth Des.* **8**, 1675–1681 (2008).

39. Voorhees, P. W. The theory of Ostwald ripening. *J. Stat. Phys.* **38**, 231–252 (1985).

40. Kamiyama, E., Sueoka, K. & Vanhellemont, J. Ab initio study of vacancy and self-interstitial properties near single crystal silicon surfaces. *J. Appl. Phys.* **111**, 083507 (2012).

41. Kuklja, M. M. Defects in yttrium aluminium perovskite and garnet crystals: atomistic study. *J. Phys.: Condens. Matter.* **12**, 2953–2967 (2000).

42. Forty, A. J. Direct observations of dislocations in crystals. *Adv. Phys.* **3**, 1–25 (1954).

43. Duffy, D. M. Grain boundaries in ionic crystals. *J. Phys. C: Solid State Phys.* **19**, 4393–4412 (1986).

44. Anghelina, F. V., Bratu, V. & Popescu, I. N. Estimating the stacking faults of high alloyed steels. *The scientific bulletin of Valahia University Materials and Mechanics.* 7–11 (2013).

45. Klassen-Neklyudova, M. V. *Mechanical Twinning of Crystals*. vol. 1 (1964).

46. Friedel, G. *Leçons de cristallographie*. (1964).

47. Bobo, E., Lefez, B., Caumon, M.-C., Petit, S. & Coquerel, G. Evidence of two types of fluid inclusions in single crystals. *CrystEngComm.* **18**, 5287–5295 (2016).

48. Prelog, V. Chirality in chemistry. *Science.* **193**, 17–24 (1975).

49. Bradshaw, D. S., Leeder, J. M., Coles, M. M. & Andrews, D. L. Signatures of material and optical chirality: Origins and measures. *Chem. Phys. Lett.* **626**, 106–110 (2015).

50. Maier, N. M., Franco, P. & Lindner, W. Separation of enantiomers: needs, challenges, perspectives. *J. Chromatogr. A.* **906**, 3–33 (2001).

51. Ariens, E. J. Stereochemistry, a basis for sophisticated nonsense in pharmacokinetics and clinical pharmacology. *Eur. J. Clin. Pharmacol.* **26**, 663–668 (1984).

52. Li, B. & Haynie, D. T. Chiral Drug Separation. *Encyclopedia of Chemical Processing* 449–458 (2006).

53. Eriksson, T., Björkman, S. & Höglund, P. Clinical pharmacology of thalidomide. *Eur J Clin Pharmacol* **57**, 365–376 (2001).

54. Srisanga, S. & ter Horst, J. H. Racemic Compound, Conglomerate, or Solid Solution: Phase Diagram Screening of Chiral Compounds. *Cryst. Growth Des.* **10**, 1808–1812 (2010).

55. Steendam, R. R. E. & ter Horst, J. H. Scaling Up Temperature Cycling-Induced Deracemization by Suppressing Nonstereoselective Processes. *Cryst. Growth Des.* **18**, 3008–3015 (2018).

56. Dodsiuk, H. Chirality and stereogenicity: The importance of conformational chirality in the classification of stereoisomers. *Tetrahedron: Asymmetry.* **3**, 43–50 (1992).

57. Natarajan, R. & Basak, S. Numerical Characterization of Molecular Chirality of Organic Compounds. *CAD.* **5**, 13–22 (2009).

58. Christie, G. H. & Kenner, J. LXXI.-The Molecular Configurations of Polynuclear Aromatic Compounds. Part I . The Resolution of y-6 :6'-Dinitro- and 4:6 :4':6'-Tetranitro-diphenic Acids into Optically Active Components. *J. Chem. Soc. Transactions.* **121**, 614–620 (1922).

59. Allinger, N. L., Eliel, E. L. & Wilen, S. H. *Topics in Stereochemistry*. vol. 14 (1983).

60. Soai, K. *et al.* D- and L-quartz-promoted highly enantioselective synthesis of a chiral organic compound. *JACS.* **121**, 11235–11236 (1999).

61. Wright, A. F. & Lehman, M. S. The structure of Quarts at 25 and 590°C determined by neutron diffraction. *J. Solid State Chem.* **36**, 371–380 (1981).

62. Miyata, M., Tohnai, N., Hisaki, I. & Sasaki, T. Generation of Supramolecular Chirality around Twofold Rotational or Helical Axes in Crystalline Assemblies of Achiral Components. *Symmetry*. **7**, 1914–1928 (2015).

63. Hisaki, I., Sasaki, T., Tohnai, N. & Miyata, M. Supramolecular-Tilt-Chirality on Twofold Helical Assemblies. *Chem. Eur. J.* **18**, 10066–10073 (2012).

64. Kipping, F. S. & Pope, W. J. LXIII.—Enantiomorphism. *J. Chem. Soc. Trans.* **73**, 606–617 (1898).

65. Matsuura, T. & Koshima, H. Introduction to chiral crystallization of achiral organic compounds Spontaneous generation of chirality. *J. Photochem. Photobiol.* **6**, 7–24 (2005).

66. Nicolaou, K. C., Pappo, D., Tsang, K. Y., Gibe, R. & Chen, D. Y.-K. A Chiral Pool Based Synthesis of Platensimycin. *Angew. Chem. Int. Ed.* **47**, 944–946 (2008).

67. Lygo, B. & Wainwright, P. G. A New Class of Asymmetric Phase-Transfer Catalysts Derived From Cinchona Alkaloids - Application in the Enantioselective Synthesis of a-Amino Acids. *Tetrahedron Lett.* **38**, 8595–8598 (1997).

68. Berthod, A. Chiral Recognition Mechanisms in Enantiomers Separations: A General View. in *Chiral Recognition in Separation Methods* (ed. Berthod, A.) 1–32 (Springer Berlin Heidelberg, 2010).

69. Marchand, P. *et al.* Diastereomeric resolution rationalized by phase diagrams under the actual conditions of the experimental process. *Tetrahedron: Asymmetry*. **15**, 2455–2465 (2004).

70. Secor, R. M. Resolution of Optical Isomers by Crystallization Procedures. *Chem. Rev.* **63**, 297–309 (1962).

71. Collet, A., Brienne, M. J. & Jacques, J. Optical resolution by direct crystallization of enantiomer mixtures. *Chem. Rev.* **80**, 215–230 (1980).

72. Polenske, D., Lorenz, H. & Seidel-Morgenstern, A. Potential of different techniques of preferential crystallization for enantioseparation of racemic compound forming systems. *Chirality* **21**, 728–737 (2009).

73. Coquerel, G., Petit, M.-N., Bouaziz, R., Method of resolution of two enantiomers by crystallization. US6022409A (2000).

74. Arai, K., Ohara, Y., Takakuwa, Y., Lizumi, T., Process for preparing an optical active ester of naphthylpropinic acid. US4417070A (1982).

75. Jamison, M. M. & Turner, E. E. The inter-relation of first- and second-order asymmetric transformations. *J. Chem. Soc.* 437–440 (1942)

76. Oketani, R. *et al.* Deracemization in a Complex Quaternary System with a Second-Order Asymmetric Transformation by Using Phase Diagram Studies. *Chem. Eur. J.* **25**, 13890–13898 (2019).

77. Tamura, R. *et al.* Mechanism of Preferential Enrichment, an Unusual Enantiomeric Resolution Phenomenon Caused by Polymorphic Transition during Crystallization of Mixed Crystals Composed of Two Enantiomers. *JACS.* **124**, 13139–13153 (2002).

78. Uchida, Y., Iwama, S., Coquerel, G. & Tamura, R. A Kinetic/Thermodynamic Origin of Regular Chiral Fluctuation or Symmetry Breaking Unique to Preferential Enrichment. *Chem. Eur. J.* **22**, 11660–11666 (2016).

79. De Saint Jores, C. *et al.* Limitations of Preferential Enrichment: A Case Study on Tryptophan Ethyl Ester Hydrochloride. *Chem. Eng. Technol.* **42**, 1500–1504 (2019).

80. De Saint Jores, C. Towards a deeper understanding of preferential enrichment. A case study: DL arginine fumarate in ethanol water 50/50 mixture. (2019).

81. Havinga, E. Spontaneous formation of optically active substances. *Biochimica et Biophysica Acta* **13**, 171–175 (1954).

82. Noorduin, W. L. *et al.* Complete Deracemization by Attrition-Enhanced Ostwald Ripening Elucidated. *Angew. Chem. Int. Ed.* **47**, 6445–6447 (2008).

83. Kondepudi, D. K., Kaufman, R. J. & Singh, N. Chiral Symmetry Breaking in Sodium Chlorate Crystallization. *Science.* **250**, 975–976 (1990).

84. Kondepudi, D. K. & Hall, J. K. Kinetic chiral symmetry breaking in $NaClO_3$ crystallization. *Physica A: Stat. Mech. Appl.* **188**, 113–119 (1992).

85. Kondepudi, D. K., Bullock, K. L., Digits, J. A., Hall, J. K. & Miller, J. M. Kinetics of chiral symmetry breaking in crystallization. *JACS.* **115**, 10211–10216 (1993).

86. Kondepudi, D. K. & Sabanayagam, C. Secondary nucleation that leads to chiral symmetry breaking in stirred crystallization. *Chem. Phys. Lett.* **217**, 364–368 (1994).

87. Kondepudi, D. K., Bullock, K. L., Digits, J. A. & Yarborough, P. D. Stirring Rate as a Critical Parameter in Chiral Symmetry Breaking Crystallization. *JACS* **117**, 401–404 (1995).

88. Martin, B., Tharrington, A. & Wu, X. Chiral Symmetry Breaking in Crystal Growth: Is Hydrodynamic Convection Relevant? *Phys. Rev. Lett.* **77**, 2826–2829 (1996).

89. Viedma, C. Experimental evidence of chiral symmetry breaking in crystallization from primary nucleation. *J. Cryst. Growth.* **261**, 118–121 (2004).

90. Viedma, C. Chiral Symmetry Breaking During Crystallization: Complete Chiral Purity Induced by Nonlinear Autocatalysis and Recycling. *Phys. Rev. Lett.* **94**, 065504 (2005).

91. Sögütoglu, L.-C., Steendam, R. R. E., Meekes, H., Vlieg, E. & Rutjes, F. P. J. T. Viedma ripening: a reliable crystallisation method to reach single chirality. *Chem. Soc. Rev.* **44**, 6723–6732 (2015).

92. Noorduin, W. L. *et al.* Fast Attrition-Enhanced Deracemization of Naproxen by a Gradual In Situ Feed. *Angew. Chem. Int. Ed.* **48**, 4581–4583 (2009).

93. Engwerda, A. H. J. *et al.* Solid-Phase Conversion of Four Stereoisomers into a Single Enantiomer. *Angew. Chem.* **130**, 15667–15670 (2018).

94. Engwerda, A. H. J. *et al.* Solid Phase Deracemization of an Atropisomer. *Cryst. Growth Des.* **17**, 5583–5585 (2017).

95. McLaughlin, D. T. *et al.* Viedma Ripening of Conglomerate Crystals of Achiral Molecules Monitored Using Solid-State Circular Dichroism. *Cryst. Growth Des.* **14**, 1067–1076 (2014).

96. Azeroual, S. *et al.* Mirror symmetry breaking and chiral amplification in foldamer-based supramolecular helical aggregates. *Chem. Commun.* **48**, 2292 (2012).

97. Perez, M. Gibbs-Thomson effects in phase transformations. *Scripta Materialia* **52**, 709–712 (2005).

98. Saito, Y. & Hyuga, H. Complete Homochirality Induced by Nonlinear Autocatalysis and Recycling. *J. Phys. Soc. Jpn.* **73**, 33–35 (2004).

99. Spix, L., Engwerda, A. H. J., Meekes, H., van Enckevort, W. J. P. & Vlieg, E. Persistent Reverse Enantiomeric Excess in Solution during Viedma Ripening. *Cryst. Growth Des.* **16**, 4752–4758 (2016).

100. Saito, Y. & Hyuga, H. Chiral Crystal Growth under Grinding. *J. Phys. Soc. Jpn.* **77**, 113001 (2008).

101. Uwaha, M. A Model for Complete Chiral Crystallization. *J. Phys. Soc. Jpn.* **73**, 2601–2603 (2004).

102. Uwaha, M. Simple Models for Chirality Conversion of Crystals and Molecules by Grinding. *J. Phys. Soc. Jpn.* **77**, 083802 (2008).

103. Cartwright, J. H. E., Piro, O. & Tuval, I. Ostwald Ripening, Chiral Crystallization, and the Common-Ancestor Effect. *Phys. Rev. Lett.***98**, 165501 (2007).

104. Noorduin, W. L. *et al.* The Driving Mechanism Behind Attrition-Enhanced Deracemization. *Angew. Chem.* **122**, 8613–8616 (2010).

105. Viedma, C., Ortiz, J. E., Torres, T. de, Izumi, T. & Blackmond, D. G. Evolution of Solid Phase Homochirality for a Proteinogenic Amino Acid. *JACS* **130**, 15274–15275 (2008).

106. Viedma, C. & Cintas, P. Homochirality beyond grinding: deracemizing chiral crystals by temperature gradient under boiling. *Chem. Commun.* **47**, 12786 (2011).

107. Suwannasang, K., Flood, A. E., Rougeot, C. & Coquerel, G. Using Programmed Heating–Cooling Cycles with Racemization in Solution for Complete Symmetry Breaking of a Conglomerate Forming System. *Cryst. Growth Des.* **13**, 3498–3504 (2013).

108. https://www.coreitn.eu/. (2016).

109. Oketani, R., Hoquante, M., Brandel, C., Cardinael, P. & Coquerel, G. Practical Role of Racemization Rates in Deracemization Kinetics and Process Productivities. *Cryst. Growth Des.* **18**, 6417–6420 (2018).

110. Breveglieri, F., Maggioni, G. M. & Mazzotti, M. Deracemization of NMPA via Temperature Cycles. *Cryst. Growth Des.* **18**, 1873–1881 (2018).

111. Breveglieri, F. & Mazzotti, M. Role of Racemization Kinetics in the Deracemization Process via Temperature Cycles. *Cryst. Growth Des.* **19**, 3551–3558 (2019).

112. Katsuno, H. & Uwaha, M. Mechanism of chirality conversion by periodic change of temperature: Role of chiral clusters. *Phys. Rev. E* **93**, 013002 (2016).

113. Suwannasang, K., Coquerel, G., Rougeot, C. & Flood, A. E. Mathematical Modeling of Chiral Symmetry Breaking due to Differences in Crystal Growth Kinetics. *Chem. Eng. Technol.* **37**, 1329–1339 (2014).

114. Suwannasang, K., Flood, A. E., Rougeot, C. & Coquerel, G. Use of Programmed Damped Temperature Cycles for the Deracemization of a Racemic Suspension of a Conglomerate Forming System. *Org. Process Res. Dev.* **21**, 623–630 (2017).

115. Uchin, R., Suwannasang, K. & Flood, A. E. Model of Temperature Cycle-Induced Deracemization via Differences in Crystal Growth Rate Dispersion. *Chem. Eng. Technol.* **40**, 1252–1260 (2017).

116. Bodák, B., Maggioni, G. M. & Mazzotti, M. Population-Based Mathematical Model of Solid-State Deracemization via Temperature Cycles. *Cryst. Growth Des.* **18**, 7122–7131 (2018).

117. Bodák, B., Maggioni, G. M. & Mazzotti, M. Effect of Initial Conditions on Solid-State Deracemization via Temperature Cycles: A Model-Based Study. *Cryst. Growth Des.* **19**, 6552–6559 (2019).

118. Xiouras, C., Van Aeken, J., Panis, J., Ter Horst, J.H., Van Gerven, T., Stefanidis, G.D., Attrition-Enhanced Deracemization of $NaClO_3$: Comparison between Ultrasonic and Abrasive Grinding. *Cryst. Growth Des.* **15**, 5476–5484 (2015).

119. Xiouras, C., Fytopoulos, A., Jordens, J., Boudouvis, A., Van Gerven, T., Stefanidis, G.D., Applications of ultrasound to chiral crystallization, resolution and deracemization. *Ultrason. Sonochem*. **43**, 184–192 (2018).

120. Rougeot, C., Guillen, F., Plaquevent, J.-C. & Coquerel, G. Ultrasound-Enhanced Deracemization: Toward the Existence of Agonist Effects in the Interpretation of Spontaneous Symmetry Breaking. *Cryst. Growth Des.* **15**, 2151–2155 (2015).

121. Cameli, F., Xiouras, C. & Stefanidis, G. D. Intensified deracemization via rapid microwave-assisted temperature cycling. *Cryst. Eng. Comm*. **20**, 2897–2901 (2018).

122. Belletti, G., Meekes, H., Rutjes, F. P. J. T. & Vlieg, E. Role of Additives during Deracemization Using Temperature Cycling. *Cryst. Growth Des.* **18**, 6617–6620 (2018).

123. Nguyen, T. P. T. *et al.* Directing the Viedma ripening of ethylenediammonium sulfate using "Tailor-made" chiral additives. *Chem. Commun.* **52**, 12626–12629 (2016).

124. Noorduin, W. L. *et al.* Complete Chiral Resolution Using Additive-Induced Crystal Size Bifurcation During Grinding. *Angew. Chem. Int. Ed.* **48**, 3278–3280 (2009).

Chapter II Synthesis and Characterization of Sodium Dithionate and its Dihydrate

I. Introduction

Sodium dithionate ($Na_2S_2O_6$) is an inorganic compound whose physico-chemical behavior remains largely unexplored and which is commonly confused with other sulfur compounds such as sodium dithionite ($Na_2S_2O_4$). Our interest in this compound, in particular for its chemical preparation as well as its characterization, is related to the study devoted to its influence as a non-chiral tailor-made impurity on the deracemization of sodium chlorate ($NaClO_3$).[1–3] This subject will be detailed in the third chapter. This chapter is focused on the synthesis of $Na_2S_2O_6$ (the compound is not commercially available), and on the characterization of the product. Indeed, solid-state characterization of a crystallized material is of paramount importance for the design of new materials. Properties such as purity, thermal stability, crystal structure, the occurrence of polymorphism,[4] or the ability to form a hydrate or solvate[5] must be thoroughly investigated to establish suitable storage conditions.[6]

After the synthesis of $Na_2S_2O_6$[7] complementary analyses using X-ray diffraction, InfraRed spectroscopy, differential scanning calorimetry and dynamic vapor sorption were performed to characterize $Na_2S_2O_6$ and to establish a clear picture of the solid-state landscape of this inorganic substance.

II. Inorganic Synthesis of Sodium Dithionate, $Na_2S_2O_6$.

The synthesis of sodium dithionate ($Na_2S_2O_6$) was first described by Schlessinger in 1962.[7] Starting from an aqueous solution of sodium sulfite (Na_2SO_3) and silver nitrate ($AgNO_3$), a two step reaction occurs. First, an ion exchange reaction between Na_2SO_3 and $AgNO_3$ occurs, giving rise to Ag_2SO_3 (Equation II-1). Then, a reduction-oxidation reaction between Na_2SO_3 and Ag_2SO_3 takes place, where silver is reduced from +I to 0 and sulfur is oxidized from +IV to +V (Equation II-2). $Na_2S_2O_6$ crystallizes as a dihydrated form.

$$Na_2SO_{3\,(aq)} + 2AgNO_{3\,(aq)} \rightarrow Ag_2SO_{3\,(s)} + 2NaNO_{3\,(aq)} \qquad \text{Equation II-1}$$

$$Ag_2SO_{3\,(s)} + Na_2SO_{3\,(aq)} \rightarrow Na_2S_2O_{6\,(aq)} + 2Ag_{\,(s)} \qquad \text{Equation II-2}$$

The yield of this synthesis was 78 %. It is limited, on one hand, by the solubility of the product, $Na_2S_2O_6$ and on the other by the solubility of the by-product, $NaNO_3$.

X-Ray analysis of the synthesized product confirmed the crystallization of the dihydrate form, by comparison with Kiers *et al.* (Figure II-1).[8]

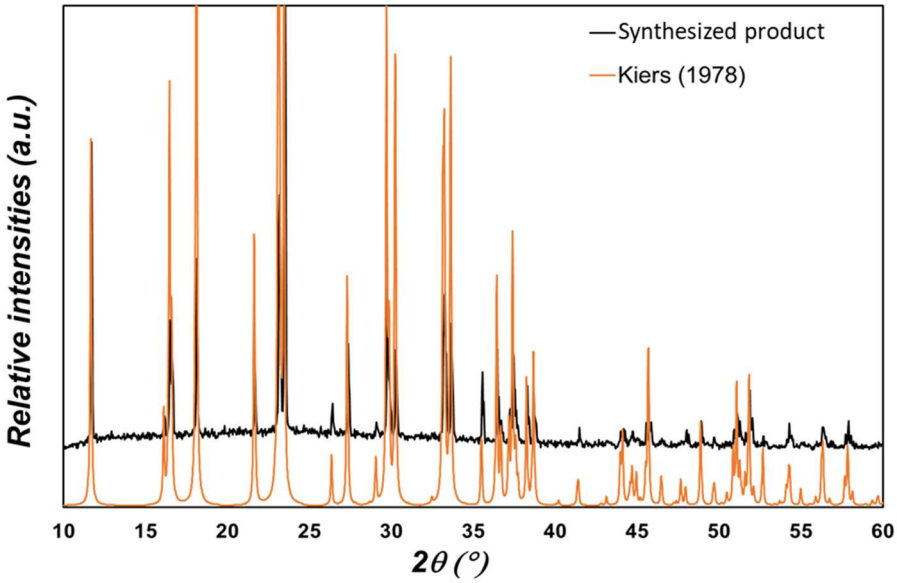

Figure II-1: Comparison of XRPD pattern of synthesized $Na_2S_2O_6 \cdot 2H_2O$ in black and the XRPD pattern of $Na_2S_2O_6 \cdot 2H_2O$ described by Kiers et al.[8] in orange

After synthesis, the product was characterized by different solid-state analysis techniques in order to characterize the relative stability of the dihydrated and the anhydrous forms. The results of these different analyses led us to explore further the dehydration mechanism of this substance.

III. **Solid State Characterization of Sodium Dithionate**

A. **Thermal Analyses**

The dehydration and decomposition of sodium dithionate dihydrate ($Na_2S_2O_6 \cdot 2H_2O$) upon heating were first characterized by Papazian *et al.* in 1972, then by Zsakó *et al.* in 1977.[9,10] The authors detected the dehydration between 40 °C and 110 °C and the decomposition of the product into sodium sulfate below 265 °C. In the present study, a TG-DSC analysis gave an accurate thermogram of $Na_2S_2O_6 \cdot 2H_2O$ up to 300 °C. This analysis, shown in Figure II-2, presents two endothermic events with mass loss associated to thermal events. The first event happens at 56 °C and the second one at 255 °C with mass losses, calculated

by gravimetry, of 14.5 % and 26.0 % respectively. The theoretical value for the loss of two molecules of water by $Na_2S_2O_6 \cdot 2H_2O$ is of 14.9 %mass. The first thermal event can thus be reasonably associated to the complete dehydration of the dihydrate form.

Concerning the second endothermic event, the asymmetric form and the considerable associated mass loss suggests a decomposition of the anhydrous product.[10]

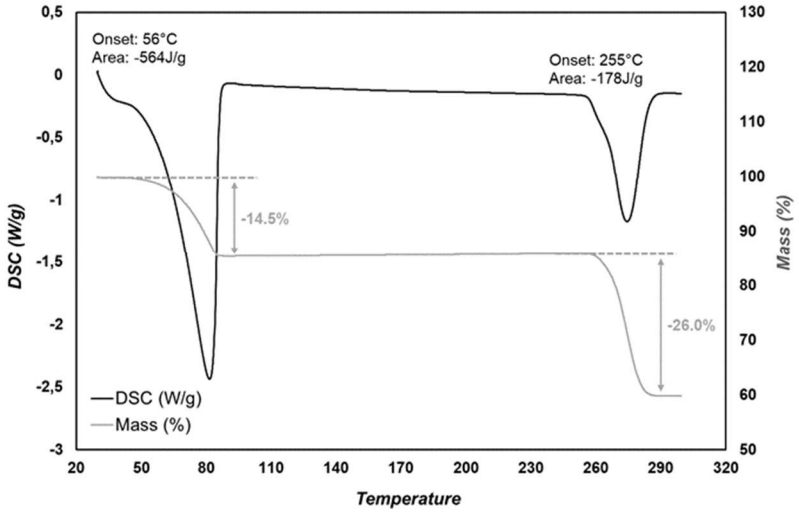

Figure II-2: TG-DSC analysis of the synthesized sodium dithionate dihydrate. DSC signal in grey, and thermo-gravimetric signal in black. Specified percentages were calculated by gravimetric analysis compared to the initial mass of the sample.

Infrared spectroscopy (IR) is a sensitive method to detect the presence of water molecules. Comparison of the IR spectra obtained with the synthesized product, $Na_2S_2O_6 \cdot 2H_2O$ (black line in Figure II-3) and on a sample that was stored beforehand in a furnace at 80°C overnight (grey line in Figure II-3) gave a noteworthy proof of the dehydration. Indeed, water molecules absorb at a characteristic wavelength which is strongly dependent on their intramolecular interactions, especially when the water molecules are involved in hydrogen bonds.

In the spectrum of the dihydrate, the absorbance at 1620 cm^{-1} is typically associated with O-H bending in H_2O molecules.[11] Bands between 3470 and 3560 cm^{-1} were assigned to stretching bands of O-H. While characteristic bands for O-H stretching are usually observed in the 3600-3700 cm^{-1} region, involvement of those hydrogen atoms in hydrogen bonds (between water and oxygen atoms bound to sulfur) increases the stiffness of the bonds and lowers the frequency of vibration below 3600 cm^{-1}.[12] Besides, absorption between 550 and 450 cm^{-1} were associated with S-S stretching while bands at 1200 and 990 cm^{-1} correspond to S=O stretching.[12,13] The latter were still observed in the spectrum

of the anhydrous form, while the characteristic bands of water disappeared. The complete dehydration of $Na_2S_2O_6 \cdot 2H_2O$ above 56 °C, observed by TG-DSC, is confirmed.

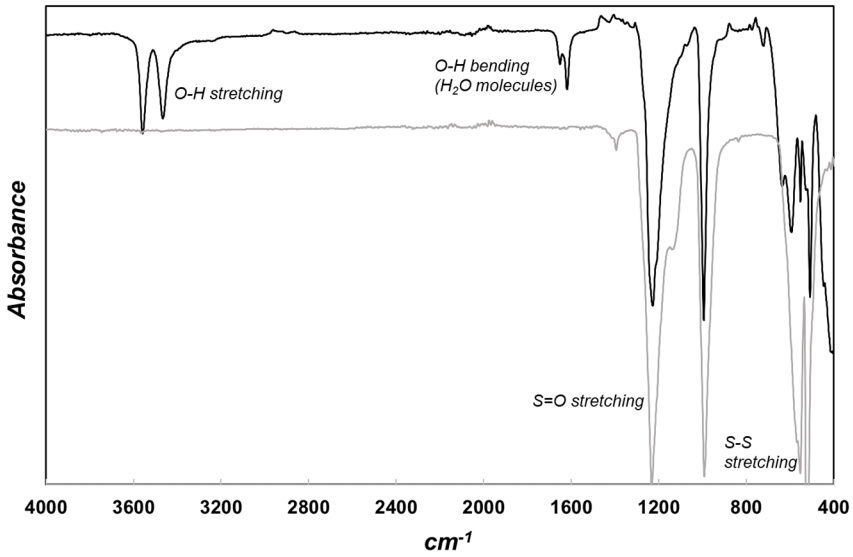

Figure II-3: Dihydrate (black line) and anhydrous (grey line) $Na_2S_2O_6$ ATR-FTIR spectra.

Further studies were performed to confirm the degradation of the product above 255 °C. Temperature Resolved X-Ray Powder diffraction (TR-XRPD) analysis was performed on $Na_2S_2O_6 \cdot 2H_2O$ from room temperature to 304 °C. Figure II-4 is a combination of all XRPD data obtained as a function of temperature. The pattern collected at 101 °C (dark grey in Figure II-4) is different from the pattern at 25 °C. This is in agreement with our interpretation that $Na_2S_2O_6 \cdot 2H_2O$ undergoes dehydration at 56 °C. Furthermore the XRPD pattern collected at 101 °C has been compared to XRPD data from the literature[14] and confirmed the presence of the anhydrous form at this temperature. Concerning the XRPD analysis performed at 253 °C (light grey in Figure II-4), diffraction peaks of the anhydrous form were observed alongside new peaks. At 304 °C (black dashed line in Figure II-4), peaks of the anhydrous form of $Na_2S_2O_6$ completely disappeared and XRPD peaks are assignable to the high temperature form of sodium sulfate (Na_2SO_4) (Figure II-5).[15,16]

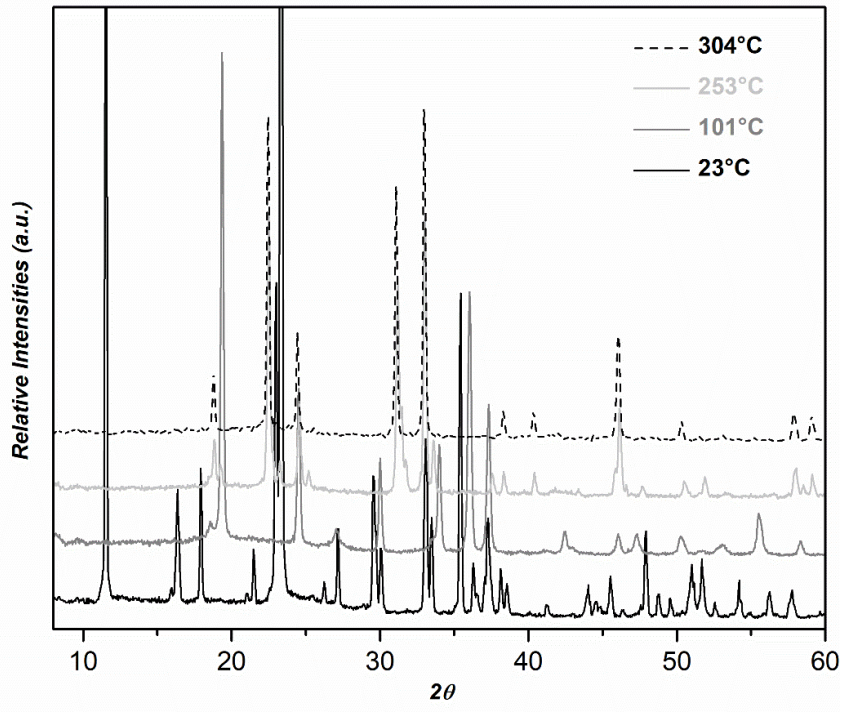

Figure II-4: TR XRPD performed on synthesized $Na_2S_2O_6,2H_2O$ at: room temperature (black line), 101 °C (dark grey line), 253 °C (light grey line), and 304 °C (black dashed line).

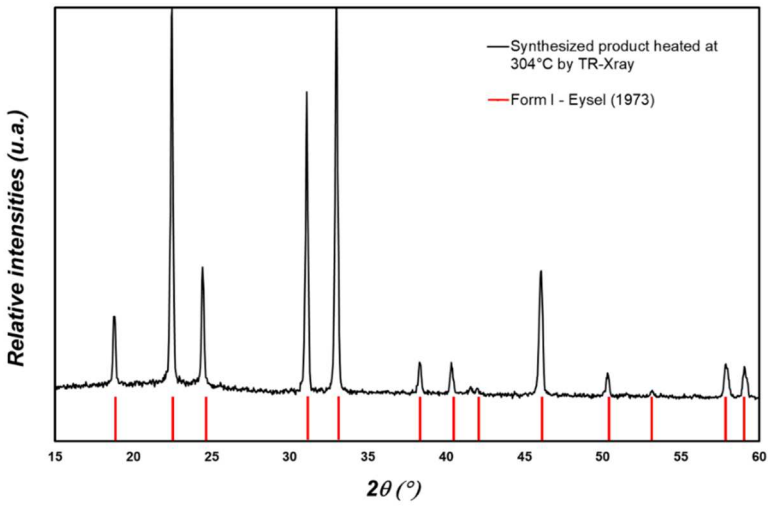

Figure II-5 : Pattern of the synthesized $Na_2S_2O_6,2H_2O$, heated at 304 °C by TR-X-Ray (black line) and diffraction peak positions of Na_2SO_4, form I, high temperature described by Eysel[16] (red peak).

This confirmed the hypothesis of a chemical decomposition of $Na_2S_2O_6$ (Equation II-3) above 250 °C, associated with the second phenomenon observed in TG-DSC (Figure II-2) with a mass loss of 26.0 % corresponding to one molecule of sulfur dioxide, the SO_2, in accordance with the theoretical value of 26.4 % mass. This mechanism is valid in the absence of oxygen.

$Na_2S_2O_{6\,(S)} \rightarrow Na_2SO_{4\,(S)} + SO_{2\,(g)}$ Equation II-3

Contrary to the report of Larson and Van Cleave,[14] dehydration did not occur after grinding at room atmosphere. However, storage of $Na_2S_2O_6 \cdot 2H_2O$ under room atmosphere sometimes lead to a mix of dihydrated and anhydrous forms. This observation prompted us to further study the hydration/dehydration behavior of $Na_2S_2O_6$ as a function of relative humidity.

B. Relative Stability of Dihydrate and Anhydrous Forms of $Na_2S_2O_6$ under Relative Humidity

Using dynamic vapor sorption (DVS) analysis at constant temperature, hydration and dehydration phenomena can be monitored as a function of relative humidity (%RH). Indeed, adsorption and desorption of H_2O by $Na_2S_2O_6$ induce respectively gain and loss of mass that can be tracked during analysis. Figure II-6 shows the percentage of mass change in equivalent number of water molecules as a function of %RH, DVS analyses were performed at 25 °C and 43 °C, without different result. The black curves in Figure II-6, are the first desorption isotherm from 90 to 0 %RH and show that hydrated compound loses two molecules of H_2O at RH between 10 and 0 %RH corresponding to dehydration of the dihydrate into the anhydrous form. Upon increasing RH, from 0 to 90 %RH, the sorption isotherm (grey curves in Figure II-6) shows that rehydration of the anhydrous form into the dihydrate occurs between 40 and 50 %RH.

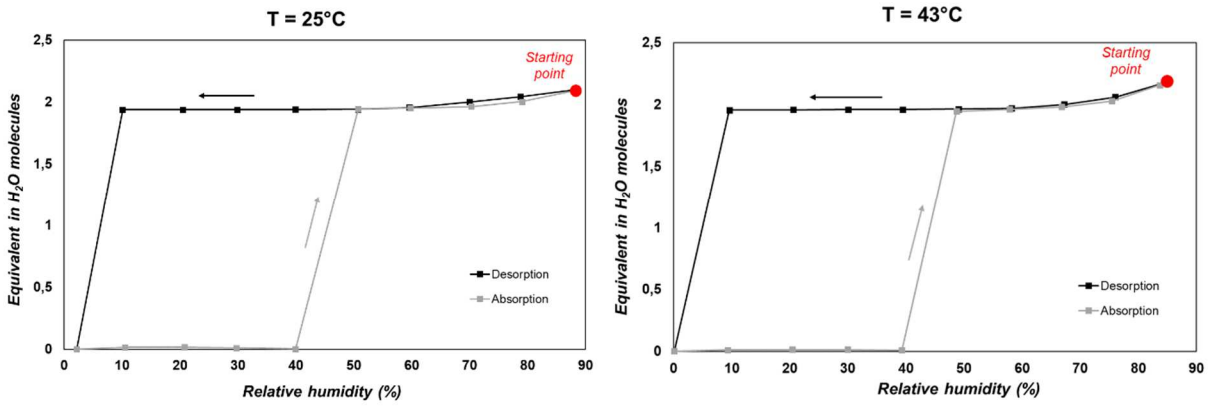

Figure II-6: Isotherm plots of $Na_2S_2O_6 \cdot 2H_2O$ at 25 °C (left) and 43 °C (right) with mass variation in equivalent number of H_2O molecules as a function of relative humidity (RH) during desorption (in black), first step and then sorption (in grey).

Thus, DVS analysis proved the full reversibility of the hydration and dehydration phenomena. Each form of $Na_2S_2O_6$ has its own stability domain as a function of RH at

room temperature, *i.e.* 25°C, and there is no behavior change at higher temperature, *i.e.* at 43°C, closer to the dehydration temperature observed at 56 °C. $Na_2S_2O_6$ is stable under 40 %RH while the dihydrated form is stable above 50%RH.

IV. Structural Role of Water and Mechanism of Dehydration

Large hysteresis between sorption, *i.e.* hydration occurs between 40 and 50 %RH, and desorption, *i.e.* dehydration occurs between 10 and 0 %RH, suggests that the departure of water molecules from the structure of the dihydrated form is delayed, indicating that water has an important role in the scaffolding of the crystal structure. This latter has been solved by Martinez *et al.* and was refined by different authors.[8,14,17,18] $Na_2S_2O_6 \cdot 2H_2O$ crystallizes in the orthorhombic space group *P*nma with a = 10.65 Å, b = 10.76 Å and c = 6.41 Å. Selected orientations of the $Na_2S_2O_6 \cdot 2H_2O$ crystal structure are shown in Figure II-7 and highlight the H-bond network in this structure. Each $S_2O_6^{2-}$ ion is linked to two water molecules by means of H-bond (Figure II-7 (a)). Other interactions are essentially non-directional ionic bonds with Na^+ ions which gives rise to a structure that can be described as an alternating sequence of $S_2O_6^{2-}$ layers and Na^+/H_2O layers colored blue and orange respectively in Figure II-7 (b) and (c). Hydrogens bonds (blue dashed lines, Figure II-7) and ionic bonds interconnect those layers.

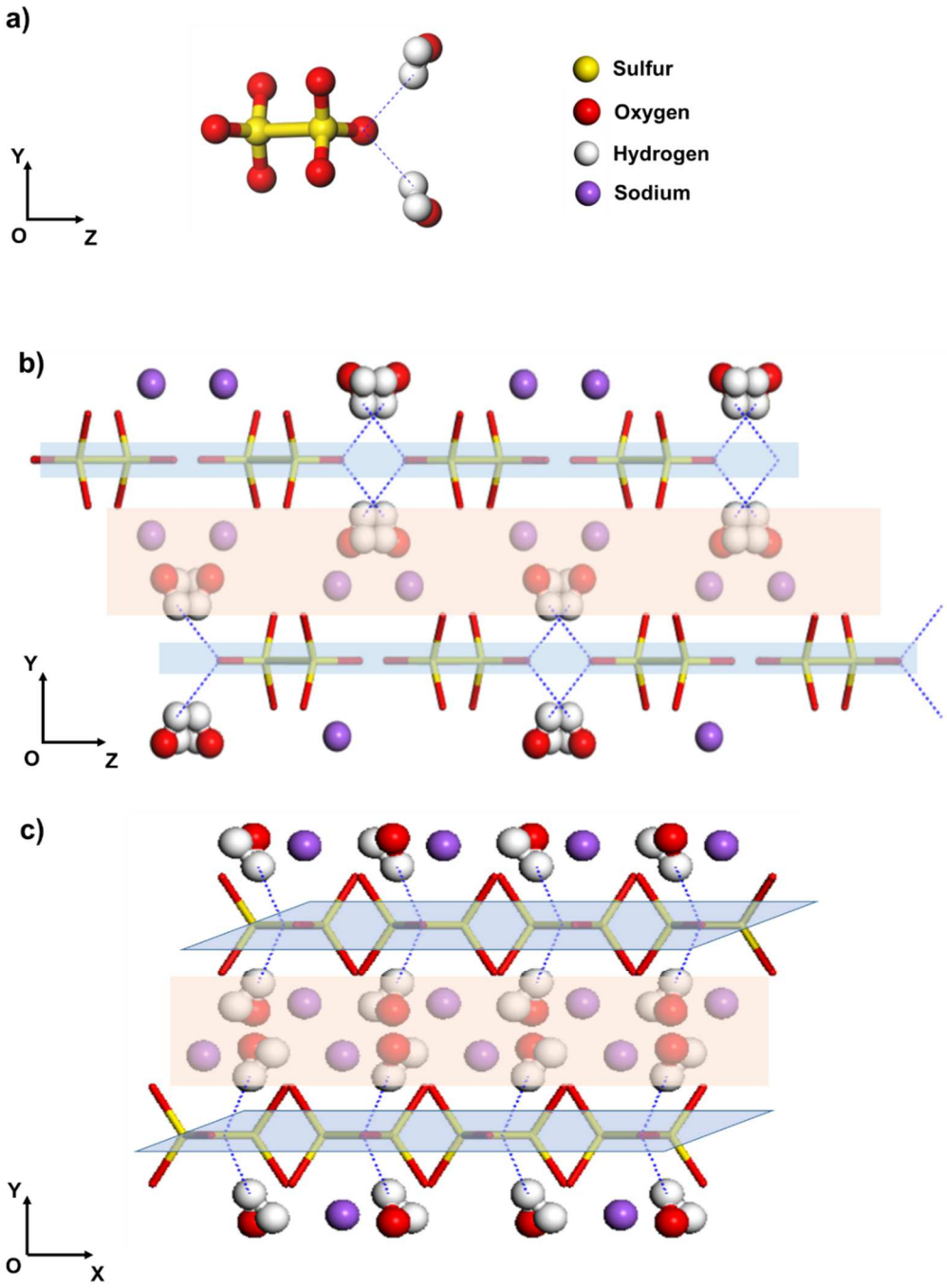

Figure II-7: Projection of the $Na_2S_2O_6 \cdot 2H_2O$ crystal structure along [100] (a),(b) and along [001] (c). Hydrogen bonds are represented in blue dashed lines. $S_2O_6^{2-}$ layers and Na^+/H_2O layers are colored in blue and orange respectively.

The short length of 2.81 Å of those H bonds, measured between donor and acceptor oxygen atoms, and the high energy required to dehydrate $Na_2S_2O_6 \cdot 2H_2O$ (around 564 $J.g^{-1}$ as measured by DSC Figure II-2) are consistent with an important role of water in the $Na_2S_2O_6 \cdot 2H_2O$ structure.

The data presented in this work indicate that the network between water molecules and dithionate ions do not form slice or ribbon from which water molecules could leave the

structure without total destruction of the scaffolding.[19] Water molecules are surrounded by dithionate ions, their departure requires a total destruction of the dihydrate structure, and conversely, the hydration probably requires a long process to build back the dihydrated form, which explains the large hysteresis in DVS analyses (Figure II-6). Thus, the departure of water molecules likely corresponds to a destructive mechanism. That is to say, the solid-solid transition from dihydrated form to the anhydrous form, *i.e.* the dehydration, occurs according to a two-step mechanism: (i) a complete destruction of the dihydrate structure resulting in an amorphous material and (ii) a nucleation and growth phenomenon leading to the crystallized anhydrous material.[19] This is in agreement with our experiment that thermal dehydration of one single crystal of $Na_2S_2O_6 \cdot 2H_2O$ does not generate a single crystal of the anhydrous form but led to a poorly crystallized fine powder of the anhydrous form.

V. Unsolved Anhydrous $Na_2S_2O_6$ Structure and Unexpected DMSO Solvate

Regarding the anhydrous $Na_2S_2O_6$ structure, the most satisfactory powder pattern we could obtain has been indexed using procedures included in the Reflex module of Materials Studio 8.0 software[20] and similar unit-cell parameters to those found by Larson and Van Cleave were obtained, consistent with an hexagonal crystal system with unit cell dimensions of a = 9.08 Å and c = 5.91 Å.[14] Unfortunately, the structure of anhydrous $Na_2S_2O_6$ is still unknown despite our efforts. The low solubility of $Na_2S_2O_6$ in various solvents (acetone, ethanol, acetronitrile, toluene) prevents the obtention of satisfactory single crystals and the determination of the anhydrous $Na_2S_2O_6$ structure. Dehydration of a dihydrate single crystal was unsuccessful and no XRPD pattern suitable for resolution by the powder method was obtained. Nevertheless, Second Harmonic Generation (SHG) analysis, a rapid and sensitive non-linear optical technique useful to detect non-centrosymmetric phases,[21] revealed that the anhydrous $Na_2S_2O_6$ form crystallizes in a non-centrosymmetric space group, contrary to the dihydrate form crystallizing in the centrosymmetric space group *P*nma.[8]

Besides, new single crystals were obtained by crystallization *via* slow evaporation of a dimethylsulfoxide (DMSO) solution. The crystal structure has been determined from single crystal X-Ray diffraction. Due to the poor stability of the crystal under ambient

conditions, the crystal was analyzed in a Lindeman capillary, in contact with the mother liquor.

Structure resolution revealed the occurrence of a solvate: $Na_2S_2O_6 \cdot 3(C_2H_6SO)$. This new compound crystallizes in the monoclinic space group $P2_1/n$ with the following parameters: $\beta = 96.16°$, $a = 10.85$ Å, $b = 8.52$ Å and $c = 19.67$ Å. Crystallographic data are given in Appendix A.8. The asymmetric unit is composed of two sodium cations, one dithionate anion, and three molecules of DMSO, the solvent of crystallization. One of these three molecules exhibits a statistical disorder (Figure II-8), with a ratio of 53%/47%. One position has been fixed to further describe the structure.

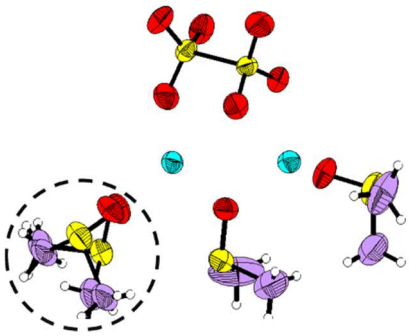

Figure II-8: Asymmetric unit in thermal ellipsoidal representation of $Na_2S_2O_6 \cdot 3(C_2H_6SO)$. The disordered DMSO molecule is circled.

The Na^+ cations exhibit two types of environment: a trigonal bipyramid where the Na^+ ion forms ionic bonds with 5 oxygen atoms (green, Figure II-9), or an octahedron where the Na^+ ion forms ionic bonds with 6 oxygen atoms (blue, Figure II-9).

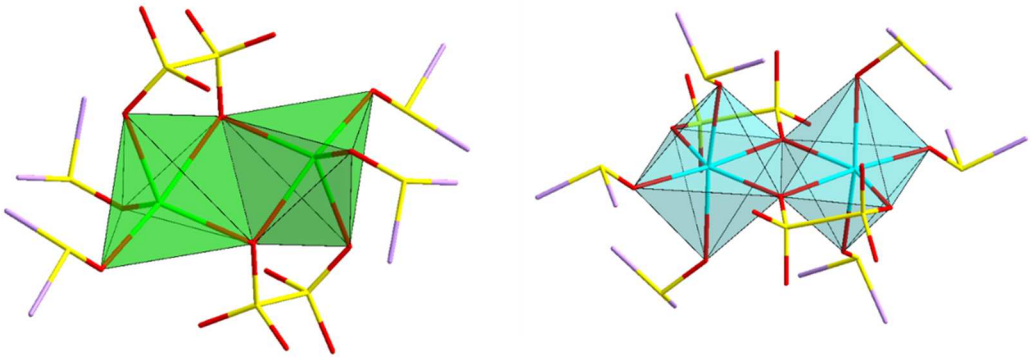

Figure II-9 : Trigonal and octahedral environments of Na^+ ions represented in green and blue respectively.

The apexes of the polyhedra are occupied by the oxygen atoms of the DMSO molecules or of the dithionate anion. The anion chelates the edges of the polyhedra, and ensures the connection from polyhedra to the adjacent ones along the *b* axis, generating columns in this direction.

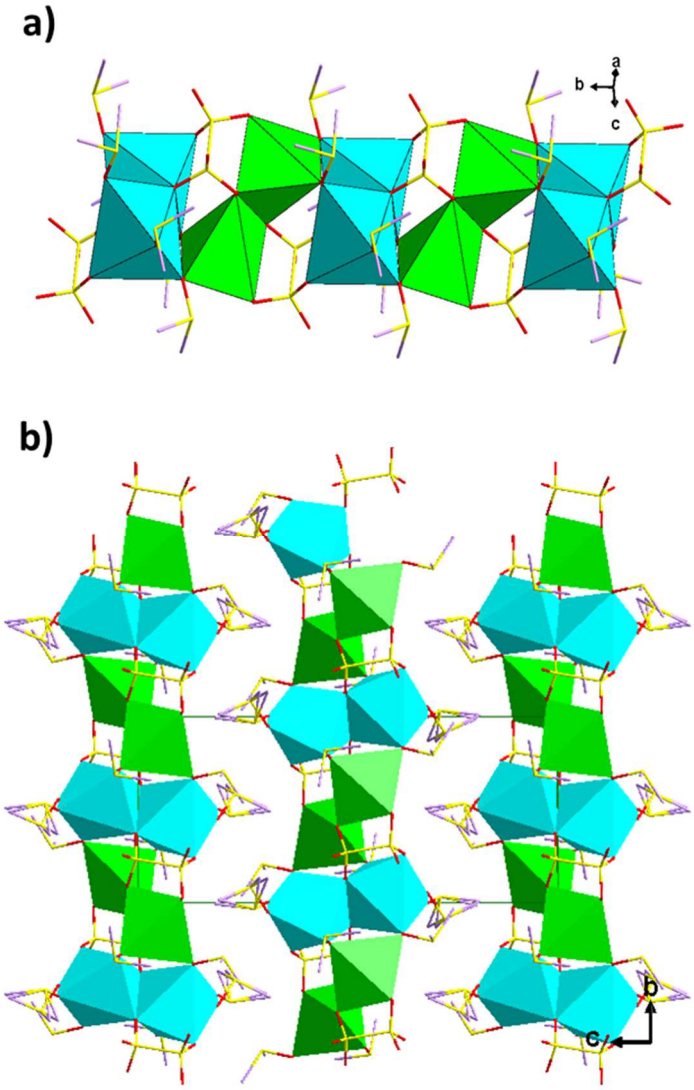

Figure II-10 : Projection of $Na_2S_2O_6 \cdot 3(C_2H_6SO)$ crystal structure (a) along [101] and (b) and along [100]. Polyhedrals of Na^+ ion, trigonal and octahedron, are represented in green and blue respectively.

The solvated crystal is efflorescent under room conditions. This instability is related to the presence of the disordered DMSO molecule in the structure (Figure II-8). The release of DMSO molecules from the solvated structure gives rise to a poorly crystallized powder of the $Na_2S_2O_6$ anhydrous form which is quickly hydrated under room conditions. Therefore, desolvation was not considered to obtain crystal structure of the anhydrous form, either by single crystal X-ray or by XRPD.

VI. **Conclusion**

As confirmed by X-ray diffraction, the synthesis of $Na_2S_2O_6$, was successful with a satisfactory yield of 78 %. Complementary experimental tools were used for a full solid-

state characterization. No polymorphic form of anhydrous $Na_2S_2O_6$ was found, however the existence of a dihydrated form has been confirmed by our analyses. The relative stability of these two forms, dihydrated and anhydrous, has been studied as a function of temperature and RH. FTIR, TG-DSC and TR-XRPD analyses showed that the dihydrated form is the most stable form below 56 °C, and that the anhydrous form decomposes at 255 °C. DVS experiments highlighted the stability domain of each form as a function of relative humidity and that the transition RH is between 40 and 50 %.

Furthermore, insights about the dehydration mechanism could be obtained. Indeed, the large hysteresis between hydration and dehydration detected by DVS and the high energy associated with dehydration measured by DSC, proves that water plays an important role in the scaffolding of the crystal structure of $Na_2S_2O_6 \cdot 2H_2O$. Therefore, all these experiments are in agreement with a destructive-reconstructive mechanism for the dehydration of the dihydrate.

The occurrence of a solvate has been higlighted in DMSO. The structure of $Na_2S_2O_6 \cdot 3(C_2H_6SO)$ has been succesfully resolved in a capillary by single crystal X-ray diffraction.

References

1. Ristic, R., Sherwood, J. N. & Wojciechowski, K. Morphology and growth kinetics of large sodium chlorate crystals grown in the presence and absence of sodium dithionate impurity. *J. Phys. Chem.* **97**, 10774–10782 (1993).

2. Lan, Z. *et al.* Characterization of the Structural Environment of Dithionate Ions Associated with Their Role in the Crystal Habit Modification of Sodium Chlorate. *Cryst. Growth Des.* **18**, 3328–3338 (2018).

3. Torbeev, V. Yu., Shavit, E., Weissbuch, I., Leiserowitz, L. & Lahav, M. Control of Crystal Polymorphism by Tuning the Structure of Auxiliary Molecules as Nucleation Inhibitors. The ß-Polymorph of Glycine Grown in Aqueous Solutions. *Cryst. Growth Des.* **5**, 2190–2196 (2005).

4. Threlfall, T. L. Analysis of organic polymorphs. A review. *Analyst.* **120**, 2435–2460 (1995).

5. Griesser, U. J. The importance of solvates. *Polymorphism in the pharmaceutical industry* 211–233 (2006).

6. Clevers, S., Simon, F., Dupray, V. & Coquerel, G. Temperature resolved second harmonic generation to probe the structural purity of m-hydroxybenzoic acid. *J. Therm. Anal. Calorim.* **112**, 271–277 (2013).

7. Schlessinger, G. G. *Inorganic laboratory preparations*. (Chemical Publishing Company, 1962).

8. Kiers, C. T., Piepenbroek, A. & Vos, A. Refinement of disodium dithionate dihydrate. *Acta Crystallogr. B.* **34**, 888–890 (1978).

9. Papazian, H. A., Pizzolato, P. J. & Peng, J. Observations on the thermal decomposition of some dithionates and sulfites. *Thermochim. Acta.* **5**, 147–152 (1972).

10. Zsakó, J., Brandt-Petrik, E., Liptay, G. & Várhelyi, Cs. Kinetic analysis of thermogravimetric data. XI thermal decomposition of some metal dithionates. *J. Thermal. Anal.* **12**, 421–428 (1977).

11. Yang, Z. & Giester, G. Hydrogen bonding in goldichite, KFe(SO4)2·4H2O: structure refinement. *Miner. Petrol.* **112**, 135–142 (2018).

12. Stuart, B. H. *Infrared Spectroscopy: Fundamentals and Applications*. (2004).

13. Nyberg, B. & Larsson, R. Infrared Absorption Spectra of Solid Metal Sulfites. *Acta Chem. Scand.* **27**, 63–70 (1973).

14. Larson, D. W. & VanCleave, A. B. X-Ray diffraction data for alkali dithionates. *Can. J. Chem.* **41**, 219–223 (1963).

15. Mofaddel, N., Bouaziz, R. & Mayer, M. Le polymorphisme du sulfate de sodium anhydre et les phases intermediaires, glaserite et aphtitalite, dans le binaire Na2S04-K2S04. *Thermochim. Acta.* **185**, 141–153 (1991).

16. Eysel, W. Crystal chemistry of the system Na_2SO_4-K_2SO_4-K_2CrO_4-Na_2CrO_4 and the glaserite phase. *Am. Min.* **58**, 736–747 (1973).

17. Martinez, S., Garcia-Blanco, S. & Rivoir, L. Crystal structure of sodium dithionate dihydrate. *Acta Cryst.* **9**, 145–150 (1956).

18. Kirfel, A., Will, G. & Weiss, A. X-ray diffraction study of $Na_2S_2O_6.2H_2O$ and $Na_2S_20_6$. $2D_20$. *Acta Crystallogr. B.* **36**, 223–228 (1980).

19. Petit, S. & Coquerel, G. Mechanism of Several Solid−Solid Transformations between Dihydrated and Anhydrous Copper(II) 8-Hydroxyquinolinates. Proposition for a Unified Model for the Dehydration of Molecular Crystals. *Chem. Mater.* **8**, 2247–2258 (1996).

20. Accelrys, Inc. *Materials Studio, version 8.0.* (2018).

21. Simon, F., Clevers, S., Dupray, V. & Coquerel, G. Relevance of the Second Harmonic Generation to Characterize Crystalline Samples. *Chem. Eng. Technol.* **38**, 971–983 (2015).

Chapter III Influence of Sodium Dithionate on Sodium Chlorate Deracemization

I. Introduction

Chirality associated with sodium chlorate ($NaClO_3$) was first described by Kipping and Pope.[1] In 1990, Kondepudi showed the possible spontaneous symmetry breaking under crystallization by means of quenching a supersaturated solution.[2] More recently, $NaClO_3$ was used by Viedma as a model compound for the development of a new process of chiral resolution, now called Viedma ripening, based on a spontaneous symmetry breaking phenomenon.[3] Indeed, glass beads in a suspension afford important attrition to the crystals and small local fluctuations of the enantiomeric excess or of the crystal size distribution (CSD). Amplification of these fluctuations *via* the autocatalytic nature of the process and crystal recycling leads to total symmetry breaking.[3,4] Afterwards, other methods derived from Viedma ripening were reported using different types of energy input to hasten deracemization, such as temperature cycling,[5] ultrasound[6,7] or microwaves[8]. It is of note that all these methods have mostly been applied to organic chiral compounds, as the studies were mostly motivated by pharmaceutical aims. In particular, temperature cycling induced deracemization (TCID) drew attention due to the efficacy of the method to deracemize several organic chiral compounds and the absence of work-up.[5,9–11] While deracemization via regular attrition has been largely investigated for $NaClO_3$,[1–3,6,12–22], this inorganic substance has never been resolved by TCID, although Viedma and Cintas already suggested a possible deracemization via the spatial temperature gradient occurring in a boiling solution.[23]

Process optimization of the deracemization of chiral compounds by addition of chiral impurities has been recently studied.[24–26] Studies showed that judicious addition of an enantiopure chiral impurity, with similar geometry as the studied chiral compound, can hamper the growth of the distomer (a term mainly used in a pharmaceutical context to designate the unwanted enantiomer) and hasten deracemization towards the eutomer (*i.e.* the desired enantiomer). This constitutes another hole in the state of the art for $NaClO_3$ deracemization: to the best of our knowledge, there is no experimental data available concerning the impact of eventual impurities on $NaClO_3$ deracemization.

The first part of this chapter is therefore devoted to the development of a TCID process for $NaClO_3$, using the well-known Viedma Ripening process as reference, which was actually reproduced by ourselves, with our equipment. The second part of this work evaluates the influence of sodium dithionate ($Na_2S_2O_6$) on the TCID process of $NaClO_3$ since it has been

reported that $Na_2S_2O_6$ has a strong influence on the morphology of $NaClO_3$ crystals, even in a molar ratio quantity as low as 1/1000.[27–30]

II. Presentation of Sodium Chlorate ($NaClO_3$)

A. Chirality of $NaClO_3$

Sodium chlorate is an achiral compound, *i.e.* without a stereogenic center, crystallizing in the achiral cubic space group $P2_13$, with $a = b = c = 6{,}5758$Å.[31–33] However, the crystal packing of $NaClO_3$ presents two mirror-image related arrangements due to their 2_1 screw axis (see Chapter I, II-4). Each enantiomorph deviates the plane of polarized light in opposite directions, therefore one enantiomorph is dextrogyre (deviation to the right), while the other one is levogyre (deviation to the left).[1,33–35]

As the compound is achiral and only presents chirality in the solid state, enantiomorphs are only distinguishable in the solid crystalline state. All information about the chirality are instantaneously lost when $NaClO_3$ is in the liquid or solvated state.[36] Thus, the use of usual chiral analytical methods, such as chiral chromatography or polarimetry to determine the crystal enantiomeric excess (CEE) of a system is not possible for $NaClO_3$. By slow evaporative crystallization, $NaClO_3$ crystals have a cubic habit and opposite enantiomorphs cannot be discriminated using their habit, contrary to quartz crystals, as no hemihedral faces are visible.[37]

However, transparent single crystals placed against the cell of the polarimeter and crossed by the light beam deviate the plane of the polarized light and allow to determine the dextrogyre or the levogyre nature of those crystals. While this experiment did not give access to the specific rotation of $NaClO_3$, it allows us to determine the dextrogyre or levogyre nature of $NaClO_3$ crystals. Single crystal giving a positive (or negative) deviation, *i.e.* deviating the polarization plane of the light to the right (or left) is dextrogyre (or levogyre). Then, they serve as reference under polarized light microscope. Indeed, with a shift of 5° between the polarizer and the analyzer of the microscope, the levogyre single crystal appear brown (*l*-$NaClO_3$ afterwards), and the dextrogyre single crystal appear blue (*d*-$NaClO_3$ hereafter, Figure III-1). Moreover, $NaClO_3$ crystals are isotropic due to the cubic space group of the structure:[38,39] the optical properties (as well as other physical properties) are identical in every direction of the single crystalline particle, which enables the determination of the enantiomeric excess of a mixture of $NaClO_3$ crystals, whatever

their orientation with reference to the polarizer. The CEE determination of a mixture of $NaClO_3$ is only possible by observation under an optical microscope operating in cross polarization mode.

Figure III-1 : Dextrogyre (d-$NaClO_3$, right) and levogyre (l-$NaClO_3$, left) $NaClO_3$ crystals under polarized light microscopy.

B. Description of the Morphology of $NaClO_3$ Crystals

1. Equilibrium Morphology of $NaClO_3$

Crystallization of $NaClO_3$ from pure aqueous solution, by slow evaporation of the solvent, typically gives rise to large crystals (~ 5×5×2 mm) with typical cuboid {100} morphology (Figure III-1 and Figure III-2). Different authors have described the appearance of the {111}, {110} and {120} faces in the morphology of $NaClO_3$ crystals, when the supersaturation was very low[28] or during flow crystallization.[40] Lan *et al*, observed cuboid shape of $NaClO_3$, complemented with the {111} and {110} faces, depending on the cooling rate used during crystallization.[41]

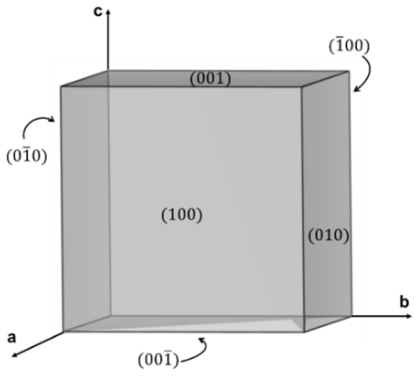

Figure III-2 : Typical cubic habitus of an $NaClO_3$ crystal when grown from aqueous solution. Miller indexes are indicated on corresponding faces. The morphology has been calculated with Material Studio 8.0, by means of the morphology calculation tool and the Bravais Friedel Donnay Harker (BFDH) method.

2. Morphology of $NaClO_3$ Grown from Solutions Containing Sodium Dithionate ($Na_2S_2O_6$)

Evolution of the $NaClO_3$ habit has been studied under the influence of many substances. Firstly, Buckley *et al.*[42,43] explained that the impact of different RO_4 type compounds is due to the similar geometry between the tetrahedron formed by the ClO_3^- ions and by RO_4 ions, and calculated the critical amount at which the $NaClO_3$ crystal habit was modified. Thus, SeO_4^{2-}, ClO_4^-, $Cr_2O_7^{2-}$, CrO_4^{2-}, SO_4^{2-}, $S_2O_3^{2-}$, $B_4O_7^{2-}$ and $S_2O_6^{2-}$ have an influence on the morphology of $NaClO_3$ crystals. A deeper study on the influence of NaS_2O_6 on the $NaClO_3$ habit was performed more recently by Ristic *et al.*[27] These authors estimated a critical value of 70 ppm of NaS_2O_6 above which the typical habit of $NaClO_3$ crystals (Figure 3) is modified, and the higher the amount of NaS_2O_6, the larger the morphological index of {111} faces. In their second publication,[28] they measured the growth rate of the {111} faces in the presence of 120 ppm and 1200 ppm of NaS_2O_6, and described a strong decrease of the growth rate of these faces in the presence of the impurity. However, no comparison with the growth rate of other faces, such as the {100} faces, was performed. Lan *et al.* brought experimental evidence of the influence of $Na_2S_2O_6$ on the crystal habit of $NaClO_3$.[29,30] Local structures of the crystals can be studied by Extended X-Ray Absorption Fine Structure (EXAFS) analyses and the environment around the impurity docked on the $NaClO_3$ crystal surface has been described. The initial hypothesis of Buckley *et al.*[42,43] in which the habit change was due to the geometry of the ionic impurities has been confirmed: The O_3 tetrahedral moiety of the $S_2O_6^{2-}$ ion substitutes an ClO_3^- anion at the {111} faces, consequently, the face growth rates and the morphology are changed.[29] Thus, in the presence of $Na_2S_2O_6$, the crystal habit of $NaClO_3$ is tetrahedral with {111} faces predominating and {100} faces no longer observable.

Experiments of $NaClO_3$ crystallization by slow evaporation of the solvent (water), in the presence of a 1/1000 molar ratio of $Na_2S_2O_6$, clearly showed the habit change (Figure III-3).

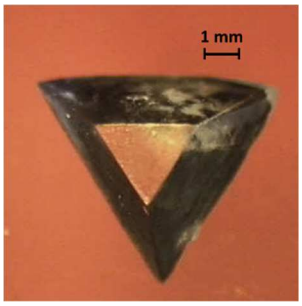

Figure III-3 : Photos of $NaClO_3$ crystals crystallized in water in the presence of 1/1000 molar ratio of $Na_2S_2O_6$.

It should be noted that the eight {111} faces are not symmetrically equivalent depending on the $NaClO_3$ enantiomorph. As a function of the chirality of the crystal, two tetrahedral crystals are described: the dextrogyre crystal (*d*-$NaClO_3$) presents the $\{\overline{1}\overline{1}\overline{1}\}$ faces, *i.e.* $(\overline{1}\overline{1}\overline{1}), (1\overline{1}1), (\overline{1}11)$ and $(11\overline{1})$ faces, and the levogyre crystal (*l*-$NaClO_3$) presents the opposite {111} faces, *i.e.* $(111), (1\overline{1}\overline{1}), (\overline{1}\overline{1}1)$ and $(\overline{1}1\overline{1})$ faces (Figure III-4).[29] Still, they cannot be distinguished from their habitus.

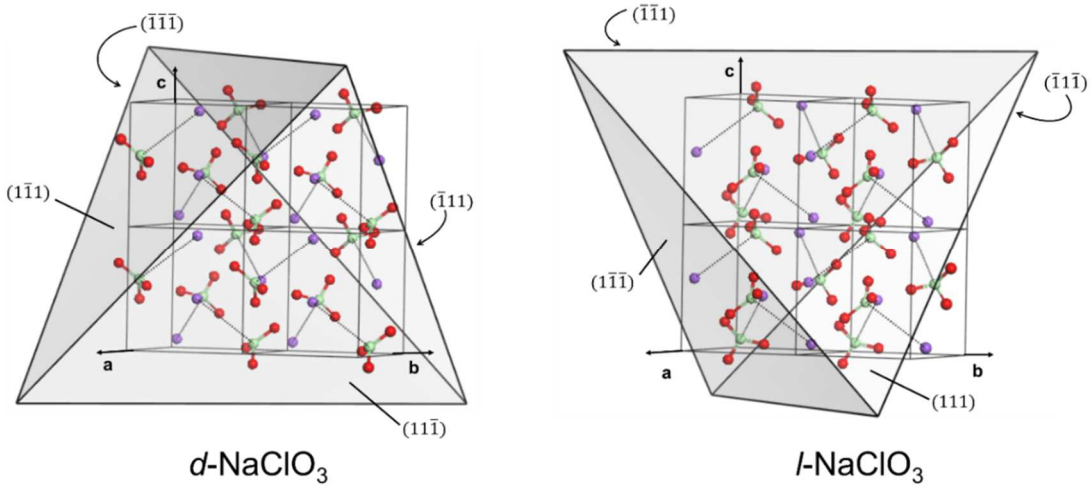

Figure III-4 : Enantiomorph morphologies of d-$NaClO_3$ (right) and l-$NaClO_3$ (left) crystals crystallized in the presence of $Na_2S_2O_6$. Miller indices are indicated on corresponding faces. These morphologies have been calculated with the Material Studio 8.0 software, by means of the morphology calculation tool and the Bravais Friedel Donnay Harker (BFDH) method.

The position of the chlorate (ClO_3^-) ions at the surfaces of these faces are different according to the chirality of the crystals. Dithionate ($S_2O_6^{2-}$) ions can replace chlorate ions at the {111} faces of levogyre crystals and at the $\{\overline{1}\overline{1}\overline{1}\}$ faces of the dextrogyre crystals. Along these specific faces, the triangle formed by the oxygen atoms in the ClO_3^- ions is parallel to the surface and the chlorine atom points outwards. Thus, the SO_3^- tetrahedron (*i.e.* the moiety of the $S_2O_6^{2-}$) can substitute the ClO_3^- ions. The face growth rates are strongly decreased by this substitution, the growth rates of the {111} and the $\{\overline{1}\overline{1}\overline{1}\}$ faces

are slower than the {100} face growth rate and the former are more represented in the final tetrahedral crystal morphology.[29]

In addition, inversion twinning was observed in rare cases (Figure III-5). The twinning phenomenon has been described in the Chapter I.I.F. Inversion twinning is a particular case of twinning where domains on both sides of the twin boundary are linked through an inversion symmetry such as inversion point, mirror or inversion axes.[44,45] The inversion twinning of $NaClO_3$ in the presence of $Na_2S_2O_6$ was described by Lan *et al.*[29,30] : When a moiety of the $S_2O_6^{2-}$ ion is docked on a surface of *e.g.* $\{\overline{1}\overline{1}\overline{1}\}$ faces of the *d*-$NaClO_3$ crystal, the second moiety can act as a nucleation site either for $\{\overline{1}\overline{1}\overline{1}\}$ faces of another *d*-$NaClO_3$ crystal, creating a homochiral twinning, without inversion in the crystallographic packing (Figure III-5-a), or for {111} faces of *l*-$NaClO_3$ crystal, creating an inversion in the packing (2_1 screw axis is inverted) and then an inversion twinning (Figure III-5-b).

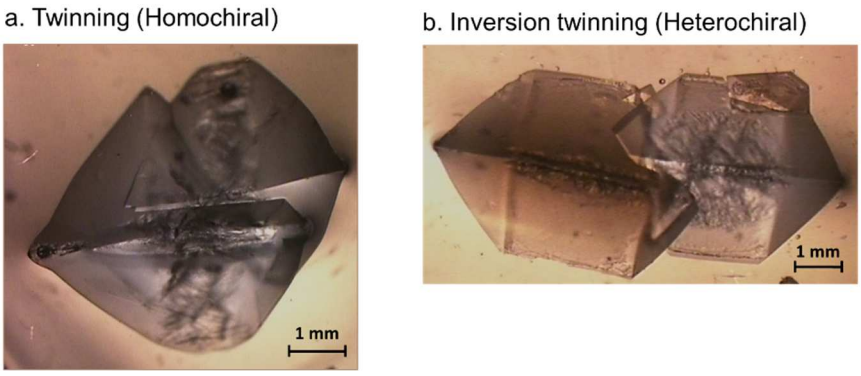

Figure III-5 : Photos of a) homochiral twinning and b) inversion twinning (heterochiral) of $NaClO_3$ crystallized in water in the presence of a 1/1000 molar ratio of $Na_2S_2O_6$.[29,30]

The occurrence of possible co-crystals, solid solutions or chemical reactions in the $NaClO_3$/$Na_2S_2O_6$ system was checked by XRPD. Different compositions such as 20, 40, 50, 60 and 80% mol of $Na_2S_2O_6$ were prepared by two different methods: (i) by manual mixing of both components and (ii) by dissolving the components in water and recrystallization upon complete slow evaporation. The two kinds of sample (mixed or recrystallized) were analyzed by XRPD with an internal standard (NaCl) and similar results were obtained in both cases. Results obtained for the recrystallized samples are presented in Figure III-6. No chemical reaction or new phase between $NaClO_3$ and $Na_2S_2O_6$ was evidenced by XRPD since only the signals of the two compounds were collected. Moreover, no solid solution was detected since no peak shifting was observed (at least within the detection limit of the XRPD patterns).

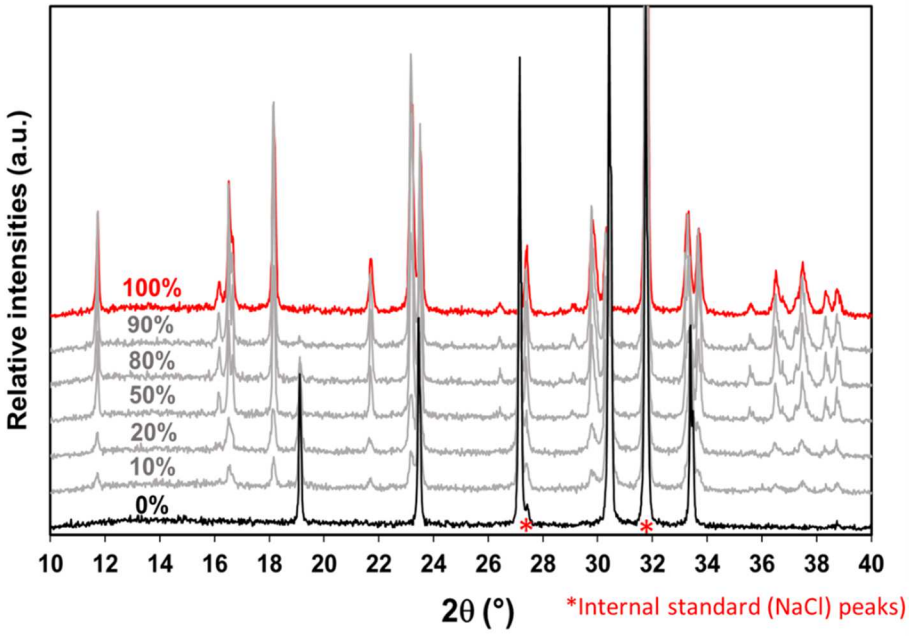

Figure III-6 : XRPD patterns of samples recrystallized in water and analyzed with NaCl as internal standard: 100% $NaClO_3$ (0% of $Na_2S_2O_6,2H_2O$) in black, 100% $Na_2S_2O_6,2H_2O$ in red and different compositions in grey. Percentage of $Na_2S_2O_6$ are indicated on respective XRPD patterns. Red stars indicate aligned peaks of the internal standard (NaCl).

3. Solubility of $NaClO_3$ in Water

$NaClO_3$ solubility in water has been largely investigated by many authors.[27,46–50] Steendam *et al.* and Hosoya *et al.* compared data and highlighted discrepancies.[47,51] In order to have our own reference, we used refractometry to determine the solubility of $NaClO_3$. The gravimetric method has been disregarded due to the easy and uncontrollable formation of liquid inclusion in crystals which leads to over-estimation of the solubility.[52]

For a given compound in a given solvent, the refractive index is, almost linear as a function of the concentration. After establishing the calibration curve of the refractive index as a function of the concentration of $NaClO_3$ in water, the refractometry method enables to determine the concentration of a saturated solution at a given temperature, *i.e.* the solubility C*. The temperature of the refractometer was set at 35°C and the calibration curve was established from 46% to 55%, expressed in %mass of $NaClO_3$. In this range of concentration, the calibration curve is linear with a correlation coefficient (r^2) of 0.9994 (Figure III-7).

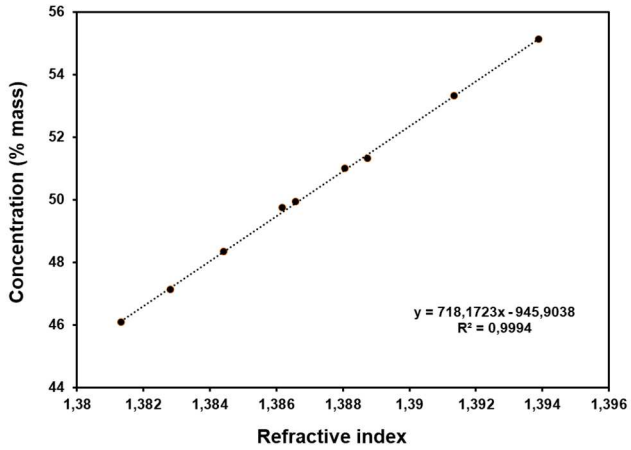

Figure III-7: Calibration curve of the refractive index as a function of the $NaClO_3$ concentration in pure water, in mass percentage at 35°C.

Saturated solutions were prepared by stirring for 12 hours a suspension of $NaClO_3$ powder in water at given temperatures between 20°C and 40°C. Saturated solutions were filtered and analyzed by refractometry. For temperatures above 35°C, *i.e.* the analysis temperature in the refractometer, saturated solutions were diluted by the addition of a known amount of water. Concentrations of saturated solutions in %mass of $NaClO_3$ were deduced from the refractive index and the solubility curve is shown in Figure III-8.

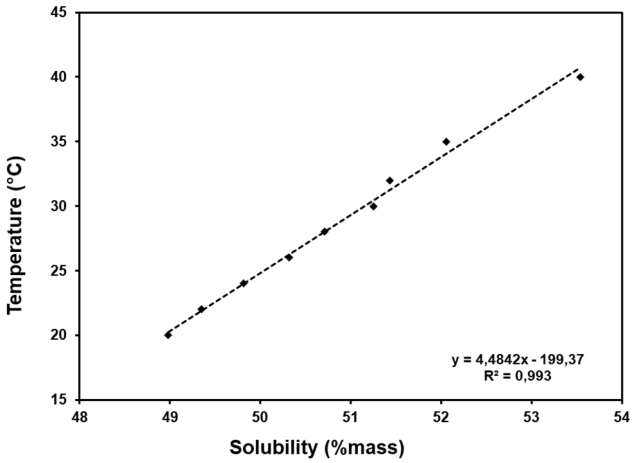

Figure III-8 : Solubility curve of $NaClO_3$ in pure water, determined by the refractometry method.

III. $NaClO_3$ Deracemization

A. Sample Preparations

Commercial $NaClO_3$ (≥98%, Alfa Aesar) was recrystallized from pure water before using in experiments. Kondepudi's method has been used for the recrystallization in order to

obtain pure homochiral populations of $NaClO_3$ crystals:[2] A suspension with 180 g of $NaClO_3$ crystals in 120 mL of pure water was heated at 90°C to obtain a clear solution. This solution was filtered to remove impurities insoluble in hot water, seeded with a ground homochiral crystal of $NaClO_3$ and cooled down to 0°C in an ice bath. By means of seeding, the crystallization is stereoselective and the powder obtained is enantiopure. The suspension was filtered and the powder was dried in a ventilated oven at 50°C overnight. This protocol was repeated with a single crystal of the opposite chirality. $NaClO_3$ crystals were ground and sieved to limit difference of crystal size distribution between each enantiomorph, then the weighing of appropriate amounts of each homochiral population of sieved crystals affords rigorous control over the initial CEE of the powder used in the suspension of deracemization experiments.

For the following experiments, a stock of saturated solution at 20°C was prepared by mixing an excess of recrystallized $NaClO_3$ in pure water at 20°C and filtering the supernatant. All $Na_2S_2O_6$ used was synthesized as described in the previous chapter of this manuscript.

B. Deracemization of $NaClO_3$ by Viedma Ripening

1. Experimental Conditions

Viedma Ripening experiments (VR hereafter) were performed in conditions close to the experiments performed by Viedma.[3] Indeed, these experiments were required to test our equipment and to have a reference situation to compare with temperature cycling induced deracemization experiments, described further in this chapter.

Deracemization experiments by VR were performed in a 50 mL round-bottom flask thermostated at 20°C with:

- 5 g of $NaClO_3$ crystals, either racemic or enantio-enriched on purpose.
- 20 mL of saturated solution at 20°C.
- 15 g of glass beads (1.5mm of diameter)
- Oval magnetic stirrer (PTFE coated, diameter: 0.5 cm, length: 1 cm)
- Stirring at 1000 rpm

To follow the deracemization kinetics, the evolution of the CEE was monitored by sampling a minimal amount of the suspension (~0.5mL) to identify the handedness of the crystals.[3] However the crystals were too small to be immediately observed under the

polarized light of the microscope. A supplementary crystal growth step was required. Thus, crystals were filtered, placed in a fresh saturated solution at 20°C and the solution was allowed to slowly evaporate at 20°C (controlled with a thermostat) for 2 or 3 days. When crystals were sufficiently large, chirality of a set of 500 to 1000 crystals was determined by polarized light microscopy (Figure III-9) and the CEE of the sample was deduced from Equation III-1, where n_d and n_l are the numbers of *d*-crystals and *l*-crystals respectively.

$$CEE_{sample}(\%) = \frac{n_d - n_l}{n_d + n_l} * 100 \qquad \textit{Equation III-1}$$

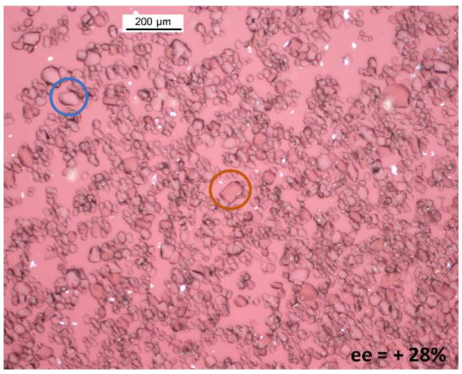

Figure III-9 : Photo of VR experiment sample after the growth step, under polarized light microscopy. A single l-crystal and d-crystal are highlighted with blue and brown circles respectively. The CEE was calculated following Equation III-1

This growth method was validated using a powder with a known CEE in equilibrium with an aqueous saturated solution, ground for few minutes with glass beads and subjected to the growth step procedure described above. For an initial CEE of 10%, 50 and 80%, the CEE of the regrown particles were 13.4%, 50.5% and 79.9% respectively, which demonstrates that the global growth step favors essentially the crystal growth and strongly limits the secondary nucleation (*i.e.* there is no significant modification of the CEE*)*.

2. Results

Recrystallization of $NaClO_3$ before use in deracemization experiments has been revealed to be essential as we observed that if deracemization is performed using commercial (instead of recrystallized) $NaClO_3$, the final CEE was systemically -100%, whatever the starting ee (up to +10% CEE) (Figure III-10). Even more surprisingly, the dashed curve in Figure III-10 shows that when starting from +10% CEE, the process evolved as expected in the first instance up to +70% CEE before a sharp and fast (actually faster than when starting from recrystallized materials) decrease toward -100% CEE.

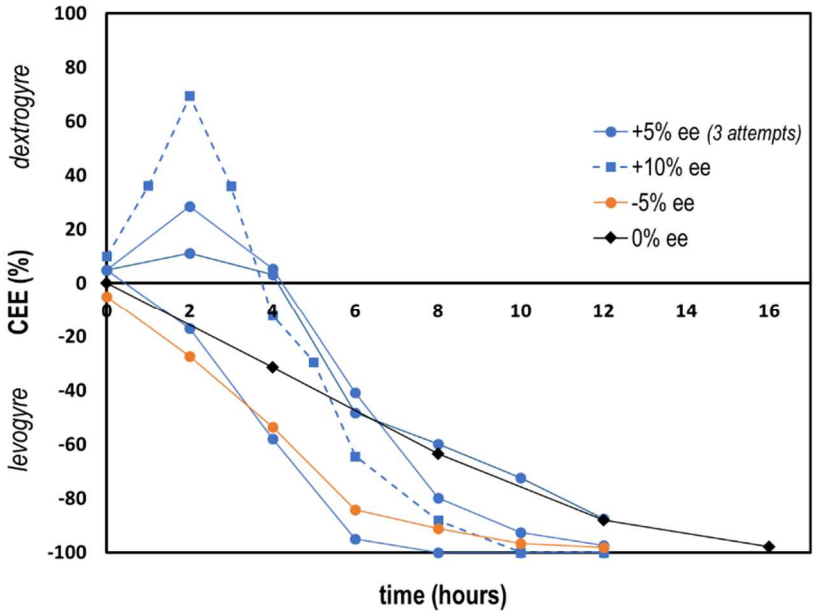

Figure III-10: Evolution of the CEE of the $NaClO_3$ crystals as a function of time for deracemization experiments by Viedma Ripening using commercial $NaClO_3$. The lines are guides to the eyes. Inlay indicates the initial % CEE.

Therefore, the purity grade of the starting material seems to play a major role in this process and underlines how sensitive $NaClO_3$ deracemization is to impurities.[14,53] Further deracemization experiments were thus performed with recrystallized $NaClO_3$.

$NaClO_3$ deracemization by VR was complete within 24 hours (Figure III-11). Results are consistent with Viedma's results.[3] They show that the initial CEE does not impact deracemization kinetics but controls the final CEE. Indeed, for +5 (or +10%) or -5% (or -10%), the final CEE was +100 or -100% respectively. For initial CEE of 0%, the final chirality of the suspension was stochastic.

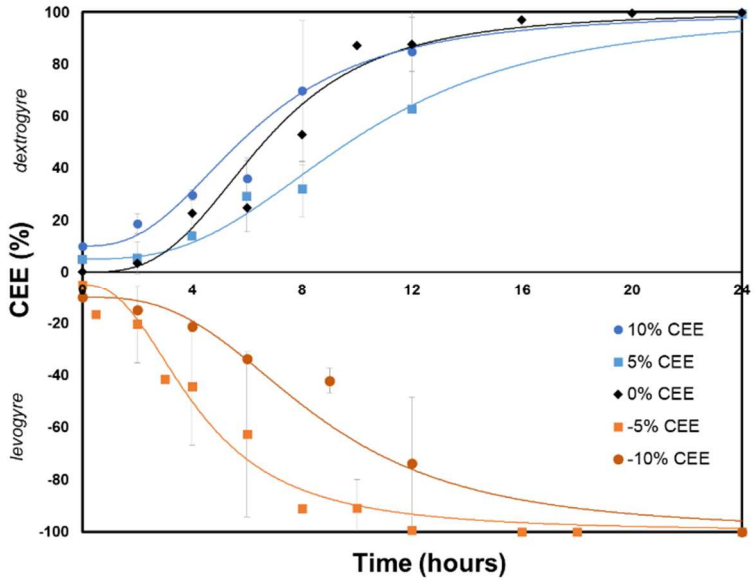

Figure III-11 : Evolution of the CEE of the $NaClO_3$ crystals as a function of time for deracemization experiments by Viedma Ripening. Each point is the averaged CEE between at least 2 attempts at the considered time, error bars results from the standard deviation between attempts. The lines are guides to the eyes. Inlay indicates the initial % CEE.

C. Temperature Cycling Induced Deracemization (TCID) of $NaClO_3$

While deracemization of $NaClO_3$ has been intensively studied by VR, Temperature Cycling Induced Deracemization (TCID hereafter) was never described for $NaClO_3$.

1. Experimental Conditions

Although performed in the same 50 mL round-bottom flask as in VR experiments and from the same initial amount of $NaClO_3$ crystals, TCID experiments required many attempts to find suitable temperature cycles for total symmetry breaking. Particularly, parameters such as the cooling rate and the percentage of crystal mass dissolved per cycles, directly related to the temperature gap (ΔT) between the lower and the higher temperature during the cycles, were found to be determinant. Slow cooling rates (0.22 or 0.33°C/min) strongly enhanced crystal growth of both enantiomorphs and the crystals were too large to permit the total disappearance of one chirality. Also, in the case of small ΔT (such as 5 or 10°C), the crystal percentage dissolved per cycles was only 6.2% and 12.5% respectively. It was insufficient to induce any initial chiral bias in the crystal populations and to evolve toward an enantiopure state.

Therefore, suitable TCID experiments were performed as follows:

- 5 g of $NaClO_3$ crystals, either racemic or enantio-enriched on purpose.
- 10 mL of saturated solution at 20°C.
- Oval magnetic stirrer (PTFE coated, diameter: 0.5 cm, length: 1 cm)
- Stirring at 500 rpm
- Temperature cycles between 26°C and 40°C, ΔT = 14°C (Figure III-12)

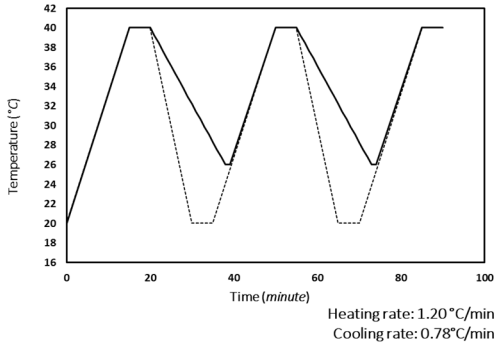

Figure III-12: Temperature cycles between 26°C and 40°C used in TCID experiments. Dashed line is the set temperature program and the solid line is the actual temperature of the suspension, measured by an internal temperature probe. Inlay shows the heating and cooling rates.

With the solubility curve previously defined (Figure III-8), the crystals mass percentage dissolved per cycles was estimated. The solubility of $NaClO_3$ in water at 26°C and 40°C is 50.3%mass and 53.4%mass respectively. Then, 0.97 g of $NaClO_3$ crystals are dissolved per cycle, corresponding to 21% of the crystalline mass repeatedly dissolved and crystallized during each cycle.

As in the VR experiments, the evolution of the CEE was monitored by sampling ~0.5 mL of the suspension, determining and counting crystals of each chirality. In TCID experiments, the growth step was not required since crystals were sufficiently large to be observed under polarized light microscopy immediately after sampling (Figure III-13).

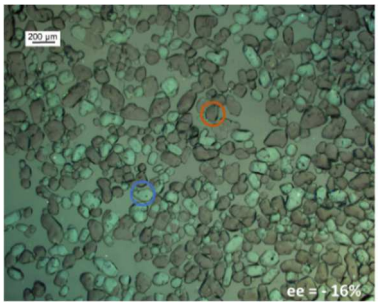

Figure III-13 : Microscopy picture of a TCID experiment sampled and observed by polarized light microscopy. Brown and blue circles point out respectively one l-crystal and one d-crystal. The CEE was calculated following Equation III-1.

2. Results

Results of TCID experiments are summarized in Figure III-14. Total symmetry breaking occurred within 36 hours, *i.e.* using 60 cycles. As in VR experiments, the initial CEE does not impact the kinetics but controls the final CEE. For initial CEE = 0%, the final CEE was stochastic, therefore the results are plotted against absolute value in Figure III-14. A blank experiment, *i.e.* under the same conditions except for the temperature which was constantly set at 20°C (ΔT = 0°C), has been performed to demonstrate the efficiency of the temperature cycle. The CEE remained close to 0 during the whole experiment.

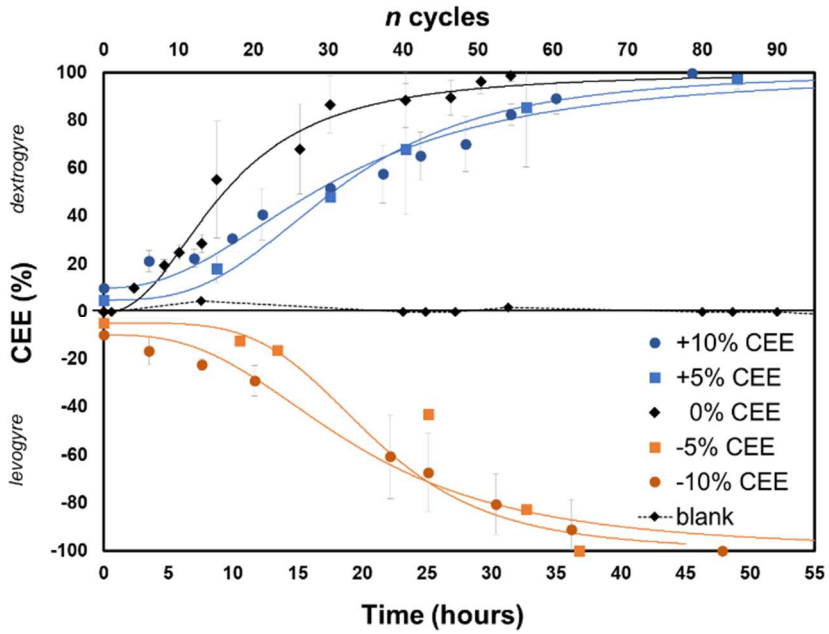

Figure III-14: Evolution of the CEE of the $NaClO_3$ powder as a function of time and cycle number for deracemization experiments by TCID. Each point is the average CEE between at least 2 attempts at the considered time, error bars result from the standard deviation between attempts. The lines are guide to the eyes. Inlay indicates the initial % CEE.

D. Comparison of Viedma Ripening and TCID Processes

In previous deracemization processes, VR or TCID, an identical initial amount of $NaClO_3$ crystals was used to permit an easy comparison between the methods in terms of productivity. While VR process rarely required more than 24 hours for total symmetry breaking (CEE = ±100%), the TCID process required at least 36 hours.

According to the S shape of the curves (Figure III-11 and Figure III-14), the results show a sigmoid evolution and suggest an autocatalytic nature of the processes. The plot of log

(CEE) vs time displays a linear trend at the beginning of deracemization in all our experiments (Figure III-15).

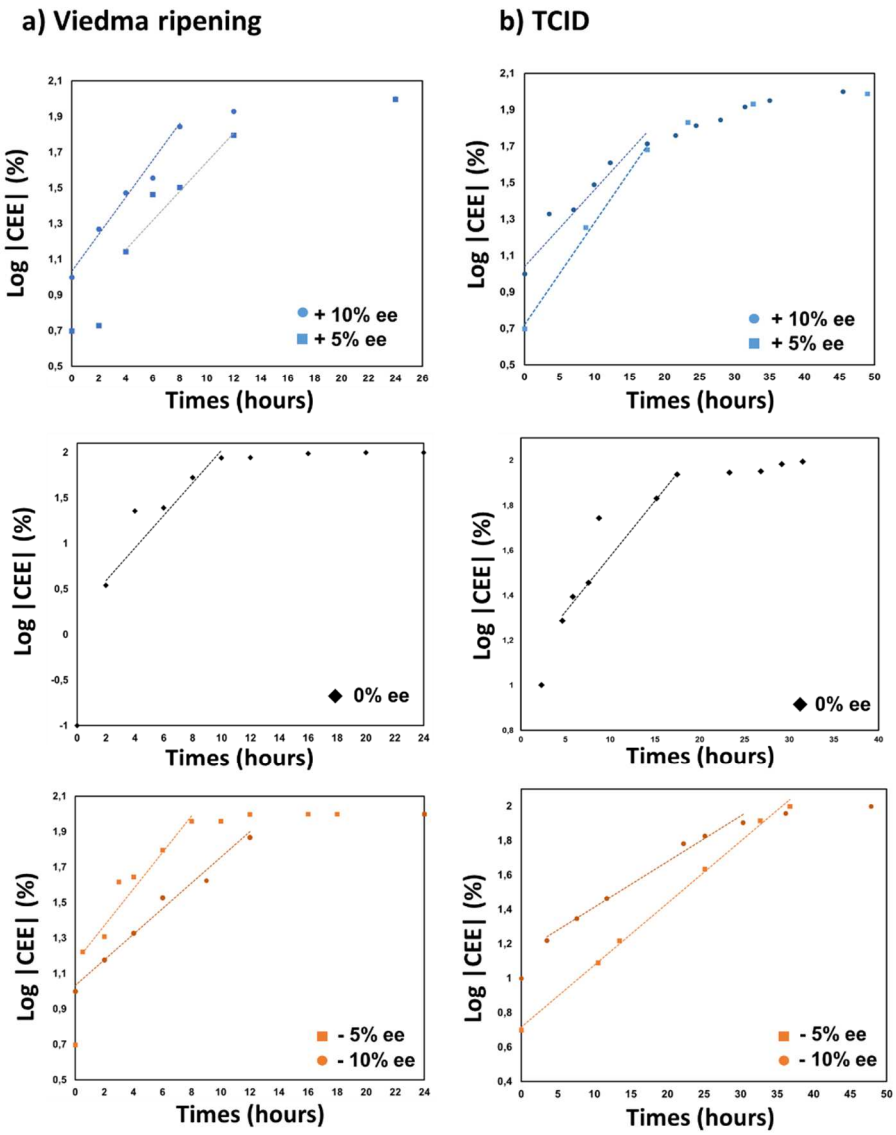

Figure III-15 : log(CEE) = f(t) for a) VR experiments and b) TCID experiments. The lines are guide to the eyes for the linear trend (detailed in appendix B.1). Inlay indicates the starting CEE.

These observations, *i.e.* the S-shaped deracemization curve and linear trends of the logarithm plots, support the autocatalytic character of the deracemization experiments,[54,55] whatever the process.

IV. Influence of $Na_2S_2O_6$ on $NaClO_3$ TCID Process

The particular incidence of $Na_2S_2O_6$ on $NaClO_3$ crystallization has been investigated in the deracemization processes. Indeed, in the case of deracemization of some chiral

compounds,[24,56] the use of chiral impurities displaying similar geometry has shown an improvement of the deracemization kinetics. While $Na_2S_2O_6$ has a similar geometry to that of $NaClO_3$, it is also worth to note the rare occurrence of inversion twinning of $NaClO_3$ crystals in the presence of that compound (Figure III-5). This phenomenon can potentially obstruct deracemization since crystallization of twinned enantiomorphs give rise to almost racemic crystals: The requirement of a conglomerate forming system for deracemization is thus no more fully respected.

Small and increasing amounts of $Na_2S_2O_6$ were added during deracemization experiments either using the VR or the TCID process. The added amounts were calculated in molar fraction as a function of the total mole number of $NaClO_3$ in the deracemization processes. In VR experiments, 5 g of $NaClO_3$ crystals and 20 mL of saturated solutions at 20°C (corresponding to 13.8g of water and 14.4g of $NaClO_3$) correspond to 0.182mol of $NaClO_3$. In TCID experiments, 5 g of $NaClO_3$ crystals and 10 mL of saturated solutions at 20°C (corresponding to 6.9g of water and 7.2g of $NaClO_3$) correspond to 0.115mol of $NaClO_3$. The corresponding amounts of $Na_2S_2O_6,2H_2O$ added are given in Table III-1.

Table III-1: Molar percentage of $Na_2S_2O_6$ and corresponding amounts of $Na_2S_2O_6,2H_2O$ added in a) attrition-enhanced deracemization and b) TCID experiments.

a) Attrition-enhanced deracemization

%mol of $Na_2S_2O_6$	mass of $Na_2S_2O_6,2H_2O$ (mg)
0.50%	*215.0*
1.00%	*430.0*
2.00%	*860.0*

b) TCID

%mol of $Na_2S_2O_6$	mass of $Na_2S_2O_6,2H_2O$ (mg)
0.01%	*2.5*
0.05%	*13.0*
0.10%	*25.0*
0.30%	*70.0*
0.50%	*114.0*
0.70%	*181.0*
1.30%	*360.0*
2.70%	*720.0*
6.00%	*1350.0*

A. Deracemization of $NaClO_3$ by Viedma Ripening in the Presence of $Na_2S_2O_6$

Unfortunately, this part of this work was quickly obstructed by the growth step required to enlarge the size of the sampled crystals during VR experiments. Indeed, as $Na_2S_2O_6$ strongly reduces the crystal growth rate of $NaClO_3$,[28] the slow evaporation of the sampled

solution during the crystal growth step systematically gave rise to the nucleation of new smaller crystals.

Different attempts were performed in order to promote the growth of the crystals and to determine the CEE of the sampled fractions, such as washing the crystals with a fresh saturated solution, without $Na_2S_2O_6$, to remove any mother liquor from the experiments or with undersaturated solutions to partially dissolve the surface of the crystals to ensure removal of $S_2O_6^{-2}$ ions docked at the $NaClO_3$ crystal surface. Yet, efficient washing is difficult to attain due to the strong impact of $Na_2S_2O_6$ even at quantities as low as 40 ppm.[41] In spite of our numerous attempts, the impact of $Na_2S_2O_6$ on the deracemization by VR of $NaClO_3$ crystals could not be established.

B. TCID of $NaClO_3$ in the Presence of $Na_2S_2O_6$

1. Experimental Conditions

Starting from a usual TCID experiment, *i.e.* 5g of $NaClO_3$ crystals and 10 mL of saturated solution, 0.01% to 6% in of $Na_2S_2O_6$ molar fraction, were added at the beginning of the experiments.

2. Results

Figure III-16 summarizes the results of the TCID experiments performed in the presence of increasing amounts of $Na_2S_2O_6$ from 0 to 6%mol. Experiments were performed with an initial CEE of 0% and the results showed that the additive had no influence on the direction of the deracemization since the final CEE was not controlled. Therefore, for the sake of clarity, the results are plotted as a function of the absolute CEE value, |CEE| (%), in Figure III-16.

The results show that the deracemization kinetics of $NaClO_3$ were significantly impacted by the presence of $Na_2S_2O_6$. Using small amounts of $Na_2S_2O_6$ (i.e. 0.01%mol) deracemization kinetics were slightly slowed down and total deracemization was observed after 42 hours (compared to 36 hours without impurity). For larger amounts, it can be seen that the higher the amount of $Na_2S_2O_6$, the longer the deracemization: a 2% mol ratio of the additive led to a process duration of 96 hours and for 6% mol ratio, the deracemization lasted more than two weeks (~20 days).

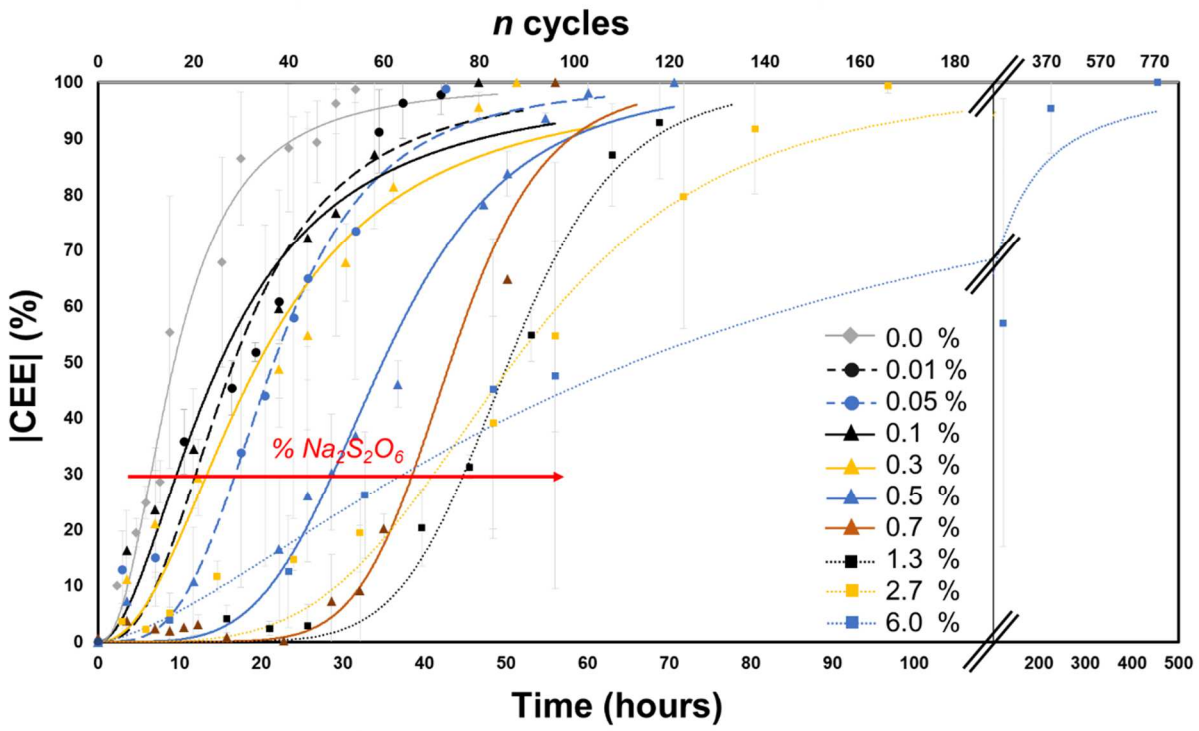

Figure III-16: Evolution of the CEE of the $NaClO_3$ suspension as a function of time and cycle number for deracemization experiments by TCID in the presence of $Na_2S_2O_6$ from 0.01%mol to 6%mol. Each point is the average CEE between at least 2 attempts at the considered time, error bars results from the standard deviation between attempts. The lines are guides to the eyes. Inlay indicates the %mol of $Na_2S_2O_6$.

The plot of the time required for total deracemization as a function of the percentage of $Na_2S_2O_6$ displayed an exponential relationship, as shown in Figure III-17.

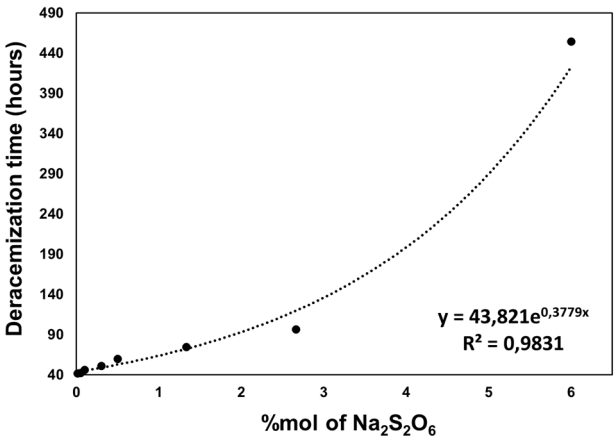

Figure III-17 : Time required for full deracemization in TCID experiments as a function of the %mol of $Na_2S_2O_6$.

Nonetheless, the TCID experiments in the presence of $Na_2S_2O_6$ did not lose their autocatalytic nature since the plots of log(CEE) as a function of time (Figure III-18) show a linear trend.

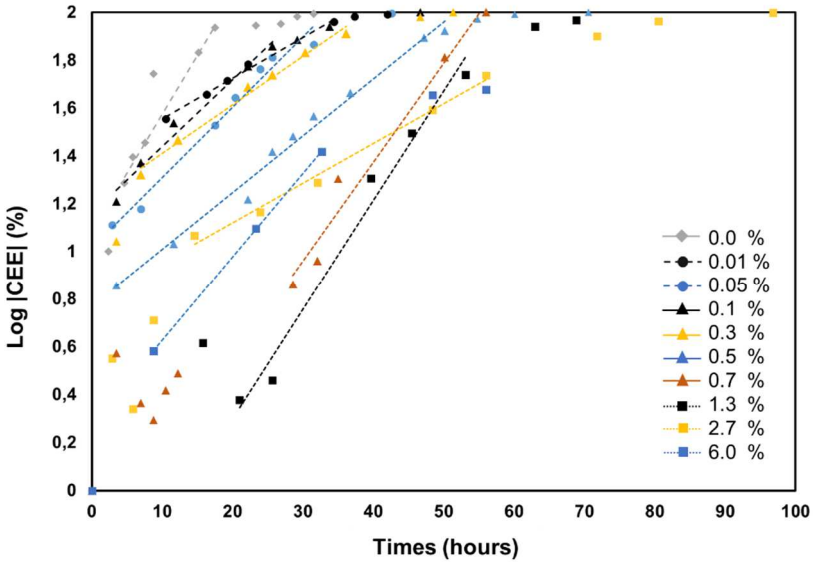

Figure III-18: log |CEE|(%) as a function of time for TCID experiments in the presence of $Na_2S_2O_6$. Dashed lines are the guide to the eyes for the linear trend (detailed in appendix B.2). Inlay indicates the %mol of $Na_2S_2O_6$.

As already detailed, the docking of a $S_2O_6^{2-}$ anion can be responsible for the occurrence of inversion twins (see II.B.2) as reported by Lan *et al.*[29] Indeed, the opposite SO_3^- moiety can act as a site for heterogeneous nucleation of the counter enantiomorph of $NaClO_3$. This could be an obvious explanation to the reduction of the deracemization kinetics of $NaClO_3$ (Figure III-16), however the formation of these twins was almost never encountered in our experiments. Further experiments were focused on the influence of $Na_2S_2O_6$ on the crystallization mechanism of $NaClO_3$, involving measurement of the crystal growth and evaluation of the secondary nucleation during the cooling step of the temperature cycling.

V. Further Investigation on the Impact of $Na_2S_2O_6$ on the Crystallization of $NaClO_3$

From a saturated solution in equilibrium with crystals, the cooling of the system generates a supersaturation which is the driving force for the crystallization either *via* crystal growth or *via* secondary nucleation. In the case of a low supersaturation, the driving force is sometimes not large enough to produce crystallization and the system is able to stay in a supersaturated metastable state favoring crystal growth rather than secondary nucleation. However, when the supersaturation becomes higher, the nucleation is uncontrolled (see, primary nucleation, Chapter 1, part I-C-2). The ability to stay in a metastable state depends on the system, $NaClO_3$ in pure water cannot bear high supersaturation and its metastable zone width (MSZW) is rather narrow.[47] We studied the

influence of $Na_2S_2O_6$ on the crystallization of $NaClO_3$ in pure water by new investigations on the crystal growth and secondary nucleation rates *via* estimates of the supersaturation at different times during TCID experiments.

A. Influence of $Na_2S_2O_6$ on the Growth Rate of $NaClO_3$

Ristic *et al*. have investigated the influence of $Na_2S_2O_6$ on the crystal growth of $NaClO_3$.[28] In this work, new experiments were focused on crystal growth rate measurements of $NaClO_3$ as a function of the percentage of $Na_2S_2O_6$ and under a controlled cooling rate, close to that used in the TCID process. In these conditions, the cooling step used during TCID (in terms of supersaturation and temperature) could be imitated, even if the hydrodynamic or the abrasion between the crystals is not represented.

1. Experimental Conditions

Crystal growth rate measurement experiments were performed in a cylindrical quartz crucible (d = 13 mm and h = 1.3 mm). A small single crystal of $NaClO_3$ (~0,5 mm²) was placed in the crucible under the microscope and warmed at 40°C using a temperature resolved setup (THMS600, Linkam) with an accurate control of the sample temperature (± 0.1°C). The cooling step was ensured by a nitrogen flux into the crucible controlled *via* an automatic pump. The crystal was covered with 5 µL of an aqueous saturated solution (T_{sat}=40°C) purposely doped with quantities ranging from 0 to 22.0 mg (*i.e.*, 0 to 2 %mol) of $Na_2S_2O_6$. The crucible was then swiftly covered with a thin glass slide. After few minutes of equilibration at 40°C, the system was cooled down to 26 °C at 1°C/min. Crystal growth rate measurements of the $NaClO_3$ single crystal were performed by time lapse measurement of the distance between the center of the crystal and the middle of the face. The monitored faces were {100} and {111}.

2. Results

The results are presented in Figure III-19-a for systems with and without $Na_2S_2O_6$. In addition, POM images of $NaClO_3$ single crystals at the beginning and at the end of the experiments (performed with or without $Na_2S_2O_6$) are presented in Figure III-19-b and show the different evolutions of morphologies during growth experiments.

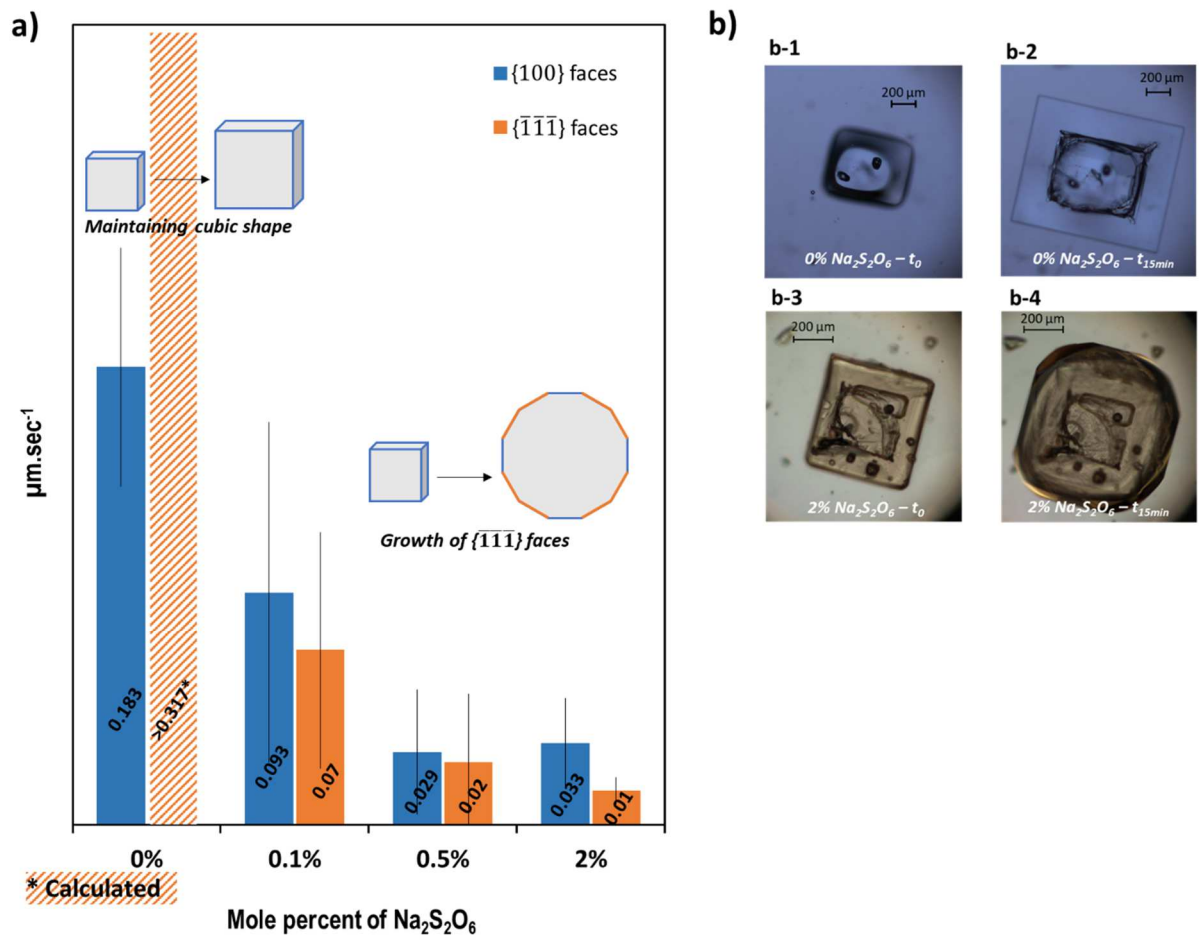

Figure III-19 a) Growth kinetics of {100} and {1̄11̄} faces of $NaClO_3$ crystals in µm / min as a function of mole percent of $Na_2S_2O_6$ in solution. Initial and final shapes of $NaClO_3$ crystals are schematically represented in the graph. b) Images of $NaClO_3$ crystals during crystal growth rate experiments at b-1) t = 0 min, without $Na_2S_2O_6$, b-2) t =15 min (end of the experiment) without $Na_2S_2O_6$, b-3) t= 0 min, with 2%mol of $Na_2S_2O_6$ and b-4) t =15 min (end of the experiment) with 2%mol of $Na_2S_2O_6$.

Without $Na_2S_2O_6$, the typical cuboid shape of $NaClO_3$ is maintained and the {1̄11̄} faces grow too fast to be represented in the final habit. Their growth rate is therefore much higher than the growth rate of {100} faces, and a calculation gave the minimum value of growth rate equals to 0.317 µm/min, above which the {1̄11̄} faces are not observable in the final crystal shape (Figure III-19). This calculation was completed with the simulation of the morphology and by calculation of the face growth rate ratio *via* the SHAPE software.[57] With the smallest amount of $Na_2S_2O_6$ (*i.e.*, 0.1%mol) the growth rates of both {100} and {1̄11̄} faces were significantly decreased. This slowdown was even stronger for the experiment conducted with 0.5% of $Na_2S_2O_6$, however, higher $Na_2S_2O_6$ amounts did not lead to further significant decrease of the growth rate. The presence of $Na_2S_2O_6$ implied a morphology change from typical cuboid shape with predominant {100} faces to round cuboid shape at the end of the growth rate experiments (Figure III-19-b). Actually, when

the growth rate of {$\overline{1}11$} faces becomes much lower than that of {100} faces, tetrahedral crystal can be obtained. A mechanism accounting for this phenomenon was proposed by Lan *et al.* (see II.B.2).[29] During crystal growth experiments, the crystal growth was estimated as a function of the %mol of $Na_2S_2O_6$ by measuring the crystal surface difference between the beginning (Area $_{initial}$) and the end (Area $_{final}$) divided by the time of the experiment, *i.e.* the time required to cool from 40 to 26 °C, 15 min.

The results shown in Table III-2 confirm that during the cooling step of a TCID experiment, the crystals grow slower and smaller in the presence of $Na_2S_2O_6$ than without the additive.

Table III-2: Growth rate of $NaClO_3$ crystals during growth rate experiments in contaminated saturated solution as a function of the %mol of $Na_2S_2O_6$

%mol $Na_2S_2O_6$	Area $_{inital}$ (µm²)	Area $_{Final}$ (µm²)	Growth (µm²/min)
0.0%	*3573132*	*5527192*	*130271*
0.1%	*3830786*	*4355030*	*34950*
0.5%	*2491196*	*2831494*	*22687*
2.0%	*4907637*	*5638282*	*48710*

The delay of crystal growth in the presence of $Na_2S_2O_6$ could generate higher supersaturation during the cooling step of TCID experiments. Therefore, supersaturation and then secondary nucleation rate of the system during TCID process was estimated with and without $Na_2S_2O_6$.

B. Influence of $Na_2S_2O_6$ on the Secondary Nucleation of $NaClO_3$

It is established that the presence of impurities may also affect the rate of nucleation during a crystallization process.[58,59] In case of a TCID experiment, it can be assumed that the presence of an impurity impacts the deracemization kinetics by either reducing or improving the nucleation rate during the cooling step. In the present case, since $Na_2S_2O_6$ increases deracemization time, it can be suspected that this impurity reduces the nucleation rate of $NaClO_3$. To validate this hypothesis, experiments were performed so as to evaluate the secondary nucleation rate of $NaClO_3$ with and without $Na_2S_2O_6$ during a typical cooling step with the same stirring as usual TCID experiments. It consists in

evaluating the remaining supersaturation at the end of a cooling step, without $Na_2S_2O_6$ and with 1%mol.

1. Experimental Conditions

During the third cycle of a TCID experiment, the process was stopped at the end of the isotherm at 40°C. The suspension was filtered and crystals were weighted to determine the concentration (from which β was deduced) at 40°C. The clear solution was placed back in the round-bottom flask and 1 to 2 large single crystals with the same chirality (~5 mm^2) were added as seeds. The system was then cooled down to 26 °C at 0.78 °C/min (same cooling rate as in the TCID process) under stirring. At 26 °C, the suspension was filtered and the crystals were weighted to determine the remaining β at 26°C. The chirality of smaller crystals produced during the cooling was observed under the microscope. These experiments were performed without $Na_2S_2O_6$ and then with 1%mol.

2. Results

The results of these experiments are in shown in Table III-3. As expected, it can be seen that with or without $Na_2S_2O_6$, the solution is saturated at 40°C ($\beta_{40°C}$ is almost 1.000) in both cases. In contrast, at 26°C, while the solution without $Na_2S_2O_6$ is in equilibrium with the crystals after cooling ($\beta_{26°C}$ almost = 1.000), the experiment performed in the presence of 1 %mol of $Na_2S_2O_6$ remains supersaturated ($\beta_{26°C}$ = 1.151). For the experiment performed without $Na_2S_2O_6$, the maximum crystalline mass attainable was reached during the cooling step, and the chirality of the produced crystal was identical to the chirality of seed crystals, which suggests that they were produced *via* secondary nucleation. However, with the experiment performed with 1 %mol $Na_2S_2O_6$, the solution remained clear until the temperature reached 26°C. No secondary nucleation occurred at all during the cooling step. Crystallization occurred only after 1 hour at 26°C and we confirmed that $\beta_{26°C,\ t+1h}$ = 1.000, produced crystals have the same chirality than seed crystals.

Table III-3 : Supersaturation, β, determined at different times of the temperature cycle during TCID experiments.

%mol of $Na_2S_2O_6$	β (40°C)	β (26°C)	β (26°C, t +1H)
0%	*0.989 ± 0.021*	*1.042 ± 0.022*	-
1%mol	*1.018 ± 0.038*	*1.151 ± 0.046*	*1.027 ± 0.077*

It should be noted that in a usual TCID process performed in the presence of 1 %mol of $Na_2S_2O_6$, the supersaturation at 26°C (estimated by a similar weighting procedure) is actually $\beta_{26°C} = 1.099 \pm 0.028$. This value is lower than β=1.151 obtained in the above experiments. This can be explained by the fact that in a regular TCID cooling, the powdered crystals in suspension provide many more sites for secondary nucleation than the single crystals used to seed the solution in the above experiments.

C. Discussion

Although secondary nucleation of $NaClO_3$ is not completely inhibited during the cooling step of TCID, our experiments (Table III-3) prove that the system bears a higher supersaturation for a longer time in the presence of $Na_2S_2O_6$ than without impurity. Therefore, $Na_2S_2O_6$ not only decreases the growth rate of $NaClO_3$ crystals (Figure III-19) but also strongly impacts the MSZW of the $NaClO_3$/water system.[59] By enlarging the MSZW upon addition of $Na_2S_2O_6$, the system undergoes less powerful crystallization-dissolution cycles, *i.e. less powerful crystal recycling,* and the results observed in our deracemization experiments (Figure III-16) likely result from a combination of reduced crystal growth rate and larger MSZW.

It is also worth mentioning that in case of TCID of organic compounds exhibiting a regular stereogenic center, the introduction of enantiopure chiral impurities often permits the control of the final CEE.[24] This is due to the autocatalytic nature of deracemization in favor of the eutomer whose crystallization is enhanced by a decrease of the growth rate of the distomer. In the present case, $Na_2S_2O_6$ delays the growth and the nucleation of both $NaClO_3$ enantiomorphs equally. The autocatalytic character of the process is therefore not enhanced and is even slowed down as the crystal recycling is less efficient.

The incidence of several critical parameters for the TCID process (such as the temperature range, the cooling rate and the racemization rate[5,11,60]) has been investigated but a unified mechanism has not been proposed yet. The experimental data obtained during this work can give valuable information to this end. In good agreement with recently published work,[61] the results highlight the importance of the secondary nucleation during TCID:[61,62] While local fluctuations of CEE or CSD induce symmetry breaking, secondary nucleation may be responsible for the autocatalytic nature of the TCID process. Indeed, the enantiomer in excess statistically produces more enantiomer of the same handedness during the cooling step and the CEE exponentially evolves toward an enantiopure state.

Accordingly, a mechanism of the TCID process can be proposed as schematized in Figure III-20. The supersaturation has to be controlled upon cooling to favor secondary nucleation over crystal growth and to avoid uncontrolled primary nucleation.

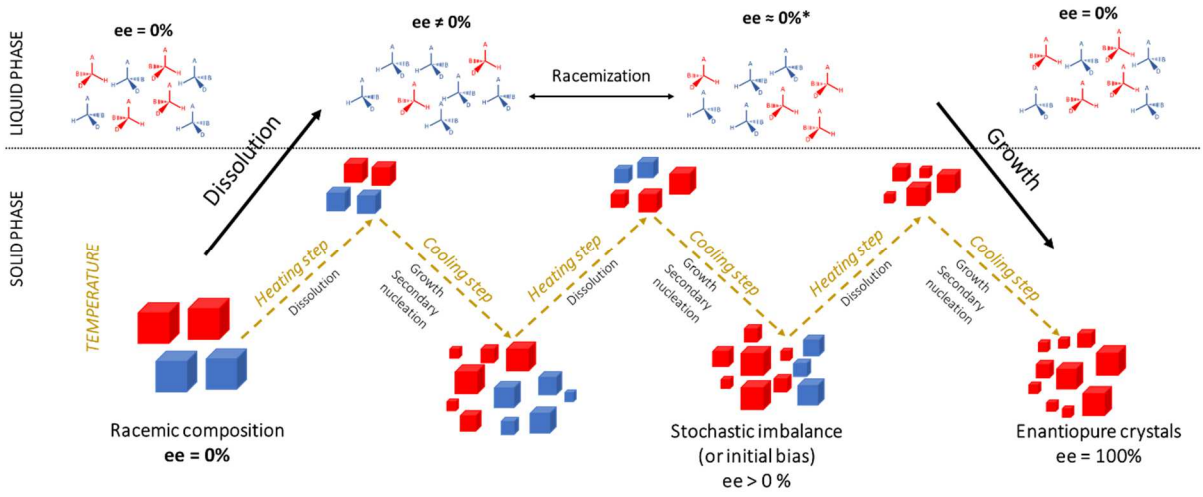

*Figure III-20 : Schematic representation of deracemization mechanisms of chiral molecules, as a general case by Temperature Cycling Induced Deracemization (TCID). *A very small enantiomeric excess of the opposite sign can exist in the solution during the process.*

VI. Influence of Others Impurities on $NaClO_3$ TCID Process

A. Sodium Sulfate (Na_2SO_4)

Buckley *et al.*[43] described the effect of sodium sulfate (Na_2SO_4) on the morphology of $NaClO_3$ from a saturated aqueous solution containing 14%mol of Na_2SO_4. The geometry of the SO_4^{2-} ion also forms a tetrahedron which explains the modification of the $NaClO_3$ habit by adsorption at the crystal surface. Thus, Na_2SO_4 has been also studied as an impurity in the $NaClO_3$ TCID process in the course of this thesis.

1. Experimental Conditions

From usual TCID experiments, *i.e.* 5g of $NaClO_3$ crystals, 10 mL of saturated solution and temperature cycles between 26°C and 40°C (Figure III-12), 1% and 5%mol of Na_2SO_4 (equivalent to 0.16 and 0.8g respectively) were added at the beginning of the experiments.

2. Results

Experiments conducted in the presence of Na_2SO_4 are compared with the TCID experiment without impurity in Figure III-21. Similarly to $Na_2S_2O_6$, the presence of Na_2SO_4 did not influence the final CEE and results were plotted as a function of the absolute value of %CEE.

Deracemization of $NaClO_3$ is weakly impacted by the presence of Na_2SO_4. The time for total deracemization is delayed by 5 hours in the presence of 5%mol of Na_2SO_4, compared to 20 days for 6%mol of $Na_2S_2O_6$. Moreover, the autocatalytic nature of the process is not disturbed as curves still exhibit the characteristic S shape and linear trend on logarithm curves (Figure III-21-a and b).

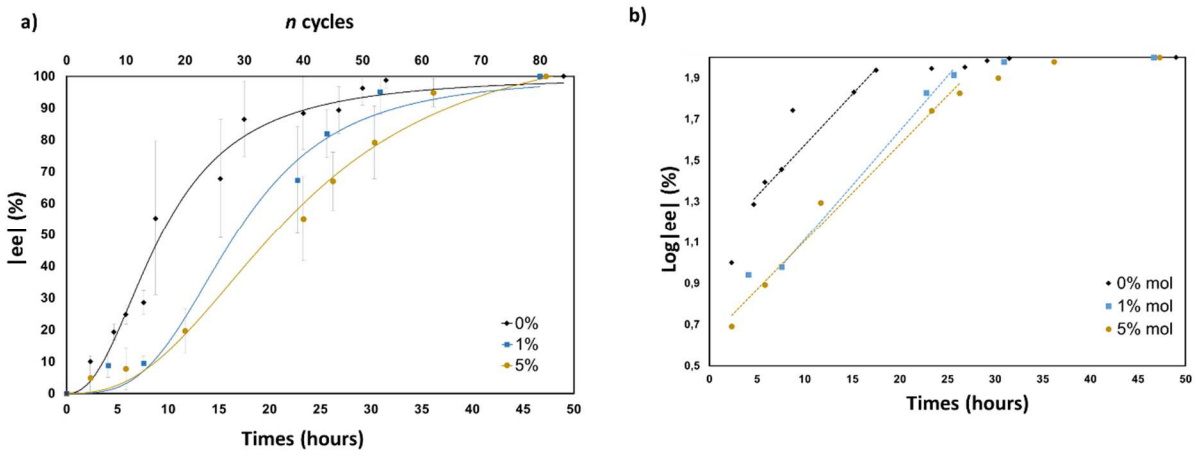

Figure III-21 : a) Evolution of the ee of the $NaClO_3$ suspension as a function of time and number of temperature cycles in the presence of 0%, 1% and 5% of Na_2SO_4. Each point is the average CEE between at least 2 attempts at the considered time, error bars result from the standard deviation between attempts. The inlays indicate the %mol of Na_2SO_4. The lines are guides to the eyes. b) Evolution of the log |CEE|(%) as a function of the time of TCID experiments in the presence of Na_2SO_4. The lines are guides to the eyes.

While the geometry of the SO_4^{2-} ions presents a SO_3 tetrahedron, the attachment of this compound is far less effective than the docking of $S_2O_6^{2-}$ ions.

B. Other Sulfur Compounds as Impurity

Sodium bisulfite ($NaHSO_3$), sodium dithionite ($Na_2S_2O_4$) and sodium metabisulfite ($Na_2S_2O_5$) are other sulfur compounds with an ion geometry including SO_3 tetrahedra and were envisaged as impurities for the TCID process. However, due to the high oxidizing power of $NaClO_3$ and the high reducing power of sulfur atoms, reduction-oxidation reactions occurred almost systematically when $NaClO_3$ and sulfur compounds were mixed

together in aqueous solution: HSO_3^- was oxidized to sulfate ions (SO_4^{2-}, Equation III-2), $S_2O_4^{2-}$ was first oxidized in SO_3^{2-} (Equation III-3), then oxidized to SO_4^{2-} (Equation III-4) Finally, $Na_2S_2O_5$ was dissociated in HSO_3^- (Equation III-5) then oxidized to SO_4^{2-} (Equation III-2)

$5HSO_3^- + 2ClO_3^- \rightarrow 5SO_4^{2-} + Cl_{2(g)} + 3H^+ + H_2O$ *Equation III-2*

$5S_2O_4^{2-} + 2ClO_3^- + 4H_2O \rightarrow 10SO_3^{2-} + Cl_{2(g)} + 8H^+$ *Equation III-3*

$5SO_3^{2-} + 2ClO_3^- + 2H^+ \rightarrow 5SO_4^{2-} + Cl_{2(g)} + H_2O$ *Equation III-4*

$S_2O_5^{2-} + H_2O \rightarrow 2HSO_3^{2-}$ *Equation III-5*

VII. **Conclusion**

This chapter was devoted to the deracemization of $NaClO_3$ by temperature cycling-induced deracemization (TCID). This method has been described for many organic compounds,[5,9,11,63] and recently for sodium bromate ($NaBrO_3$),[64] an inorganic compound sharing a strong similarity with $NaClO_3$ in terms of crystallography. However, TCID has never been applied to $NaClO_3$ despite its use as a model compound in the Viedma ripening process.[3,19]

We report that TCID is almost as efficient as Viedma ripening to deracemize $NaClO_3$. It is worth noting that the operating conditions of these two processes have not been optimized. However, during the search for suitable conditions, we evidenced that:

- The amplitude of the temperature variations must be large enough to repeatedly dissolve and crystallize a sufficient $NaClO_3$ crystalline mass (a fact intrinsically related to the mild temperature dependence of $NaClO_3$ solubility versus temperature).
- The cooling rate has to be fast enough to favor secondary nucleation at the expense of the crystal growth.

We also showed that the kinetics of TCID experiments are strongly affected by the presence of $Na_2S_2O_6$. Indeed, in case of $NaClO_3$ TCID process performed with quantity as small as 0.01%mol of $Na_2S_2O_6$, deracemization was significantly delayed and the higher the $Na_2S_2O_6$ amount, the longer the process. It is demonstrated that $Na_2S_2O_6$ decreases the growth rate of $NaClO_3$ crystals and enlarges the MSZW of the system. It is thus

concluded that the success of the TCID process relies on optimizing the balance between growth and secondary nucleation.

Therefore, the optimization of a TCID process requires a control over both crystal growth and secondary nucleation rates by a suitable adjustment of the temperature cycles (*i.e.* the ΔT and the cooling rate), especially when an impurity affecting crystallization is present.

References

1. Kipping, F. S. & Pope, W. J. LXIII.—Enantiomorphism. *J. Chem. Soc. Trans.* **73**, 606–617 (1898).

2. Kondepudi, D. K., Kaufman, R. J. & Singh, N. Chiral Symmetry Breaking in Sodium Chlorate Crystallization. *Science.* **250**, 975–976 (1990).

3. Viedma, C. Chiral Symmetry Breaking During Crystallization: Complete Chiral Purity Induced by Nonlinear Autocatalysis and Recycling. *Phys. Rev. Lett.* **94**, 065504 (2005).

4. Saito, Y. & Hyuga, H. Chirality Selection in Crystallization. *J. Phys. Soc. Jpn.* **74**, 535–537 (2005).

5. Suwannasang, K., Flood, A. E., Rougeot, C. & Coquerel, G. Using Programmed Heating–Cooling Cycles with Racemization in Solution for Complete Symmetry Breaking of a Conglomerate Forming System. *Cryst. Growth Des.* **13**, 3498–3504 (2013).

6. Xiouras, C. *et al.* Attrition-Enhanced Deracemization of $NaClO_3$: Comparison between Ultrasonic and Abrasive Grinding. *Cryst. Growth Des.* **15**, 5476–5484 (2015).

7. Rougeot, C., Guillen, F., Plaquevent, J.-C. & Coquerel, G. Ultrasound-Enhanced Deracemization: Toward the Existence of Agonist Effects in the Interpretation of Spontaneous Symmetry Breaking. *Cryst. Growth Des.* **15**, 2151–2155 (2015).

8. Cameli, F., Xiouras, C. & Stefanidis, G. D. Intensified deracemization via rapid microwave-assisted temperature cycling. *Cryst. Eng. Comm.* **20**, 2897–2901 (2018).

9. Breveglieri, F., Maggioni, G. M. & Mazzotti, M. Deracemization of NMPA via Temperature Cycles. *Cryst. Growth Des.* **18**, 1873–1881 (2018).

10. Li, W. W. *et al.* Deracemization of a Racemic Compound via Its Conglomerate-Forming Salt Using Temperature Cycling. *Cryst. Growth Des.* **16**, 5563–5570 (2016).

11. Oketani, R., Hoquante, M., Brandel, C., Cardinael, P. & Coquerel, G. Practical Role of Racemization Rates in Deracemization Kinetics and Process Productivities. *Cryst. Growth Des.* **18**, 6417–6420 (2018).

12. Kondepudi, D. K., Bullock, K. L., Digits, J. A., Hall, J. K. & Miller, J. M. Kinetics of chiral symmetry breaking in crystallization. *JACS.* **115**, 10211–10216 (1993).

13. Uwaha, M. A Model for Complete Chiral Crystallization. *J. Phys. Soc. Jpn.* **73**, 2601–2603 (2004).

14. Veintemillas-Verdaguer, S., Esteban, S. O. & Herrero, M. A. The effect of stirring on sodium chlorate crystallization under symmetry breaking conditions. *J. Cryst. Growth.* **303**, 562–567 (2007).

15. El-Hachemi, Z., Crusats, J., Ribó, J. M., McBride, J. M. & Veintemillas-Verdaguer, S. Metastability in Supersaturated Solution and Transition towards Chirality in the Crystallization of NaClO3. *Angew. Chem. Int. Ed.* **50**, 2359–2363 (2011).

16. Callahan, C. J. & Ni, X.-W. Probing into Nucleation Mechanisms of Cooling Crystallization of Sodium Chlorate in a Stirred Tank Crystallizer and an Oscillatory Baffled Crystallizer. *Cryst. Growth Des.* **12**, 2525–2532 (2012).

17. Niinomi, H. *et al.* Emergence and Amplification of Chirality via Achiral–Chiral Polymorphic Transformation in Sodium Chlorate Solution Growth. *Cryst. Growth Des.* **14**, 3596–3602 (2014).

18. Callahan, C. J. & Ni, X.-W. An investigation into the effect of mixing on the secondary nucleation of sodium chlorate in a stirred tank and an oscillatory baffled crystallizer. *CrystEngComm.* **16**, 690–697 (2014).

19. Sögütoglu, L.-C., Steendam, R. R. E., Meekes, H., Vlieg, E. & Rutjes, F. P. J. T. Viedma ripening: a reliable crystallisation method to reach single chirality. *Chem. Soc. Rev.* **44**, 6723–6732 (2015).

20. Ahn, J., Kim, D. H., Coquerel, G. & Kim, W.-S. Chiral Symmetry Breaking and Deracemization of Sodium Chlorate in Turbulent Flow. *Cryst. Growth Des.* **18**, 297–306 (2018).

21. Macleod, R. & Ni, X. Effect of surface scraping on chiral symmetry in seeded cooling crystallization of sodium chlorate. *CrystEngComm.* **20**, 3696–3701 (2018).

22. Xiouras, C. *et al.* Particle Breakage Kinetics and Mechanisms in Attrition-Enhanced Deracemization. *Cryst. Growth Des.* **18**, 3051–3061 (2018).

23. Viedma, C. & Cintas, P. Homochirality beyond grinding: deracemizing chiral crystals by temperature gradient under boiling. *Chem. Commun.* **47**, 12786 (2011).

24. Belletti, G., Meekes, H., Rutjes, F. P. J. T. & Vlieg, E. Role of Additives during Deracemization Using Temperature Cycling. *Cryst. Growth Des.* **18**, 6617–6620 (2018).

25. Engwerda, A. H. J. *et al.* Deracemization of a Racemic Compound by Using Tailor-Made Additives. *Chem. Eur. J.* **24**, 2863–2867 (2018).

26. Engwerda, A. H. J. *et al.* Solid-Phase Conversion of Four Stereoisomers into a Single Enantiomer. *Angew. Chem.* **130**, 15667–15670 (2018).

27. Ristic, R., Sherwood, J. N. & Wojciechowski, K. Morphology and growth kinetics of large sodium chlorate crystals grown in the presence and absence of sodium dithionate impurity. *J. Phys. Chem.* **97**, 10774–10782 (1993).

28. Ristic, R., Shekunov, B. Yu. & Sherwood, J. N. Growth of the tetrahedral faces of sodium chlorate crystals in the presence of dithionate impurity. *J. Cryst. Growth.* **139**, 336–343 (1994).

29. Lan, Z.-P., Lai, X., Roberts, K. & Klapper, H. X-ray Topographic and Polarized Optical Microscopy Studies of Inversion Twinning in Sodium Chlorate Single Crystals Grown in the Presence of Sodium Dithionate Impurities. *Cryst. Growth Des.* **14**, 6084–6092 (2014).

30. Lan, Z. *et al.* Characterization of the Structural Environment of Dithionate Ions Associated with Their Role in the Crystal Habit Modification of Sodium Chlorate. *Cryst. Growth Des.* **18**, 3328–3338 (2018).

31. Zachariasen, W. H. XXVIII. The Crystal Structure of Sodium Chlorate. *Zeitschrift für Kristallographie - Crystalline Materials.* **71**, 517–529 (1929).

32. Ramachandran, G. N. & Chandrasekaran, K. S. The absolute configuration of sodium chlorate. *Acta Cryst* **10**, 671–675 (1957).

33. Abrahams, S. C., Glass, A. M. & Nassau, K. Crystal chirality and optical rotation sense in isomorphous NaClO3 and NaBrO3. *Solid State Commun.* **24**, 515–516 (1977).

34. Chandrasekhar, S. & Madhava, M. S. Optical rotatory dispersion of a mixed crystal of sodium chlorate-sodium bromate. *Materials Research Bulletin.* **4**, 489–493 (1969).

35. Chandrasekaran, K. S. & Mohanlal, S. K. The x-ray anomalous dispersion and optical rotation in the crystalline solid solution $NaClO_3$: $NaBrO_3$. *Pramana.* **7**, 152–159 (1976).

36. Blackmond, D. G. “Chiral Amnesia” as a Driving Force for Solid-Phase Homochirality. *Chem. Eur. J.* **13**, 3290–3295 (2007).

37. De Vries, A. Determination of the absolute configuration of a-Quartz. *Nature.* 1193 (1958).

38. Clydesdale, G. *et al.* Prediction of the Polar Morphology of Sodium Chlorate Using a Surface-Specific Attachment Energy Model. *J. Phys. Chem. B.* **102**, 7044–7049 (1998).

39. Viswanathan, R. Elastic Constants of Sodium Chlorate Single Crystals by Pulse-Echo Method. *J. Appl. Phys.* **37**, 884–886 (1966).

40. Simon, B. Influence of the direction of the influence flow on the morphology of NaClO3 crystals. *J. Cryst. Growth.* **61**, 167–169 (1983).

41. Lan, Z. The structural role of sodium dithionate impurity in the habit modification of sodium chlorate single crystals. (University of Leeds, 2013).

42. The influence of RO4 and related ions on the crystalline form of sodium chlorate. *Zeitschrift für Kristallographie - Crystalline Materials.* **75**, 15–31 (1930).

43. Buckley, H. E. Habit modification in crystals as a result of the introduction of impurities during growth. *Discuss. Faraday Soc.* **5**, 243–254 (1949).

44. Flack, H. D. Chiral and Achiral Crystal Structures. *HCA.* **86**, 905–921 (2003).

45. Flack, H. D. & Bernardinelli, G. Absolute structure and absolute configuration. *Acta Crystallogr A Found Crystallogr.* **55**, 908–915 (1999).

46. Blanc, M. L. & Schmandt, W. Über Kristallisation und Auflösung in wässeriger Lösung. *Zeitschrift für Physikalische Chemie.* **77U**, (1911).

47. Steendam, R. R. E. & Frawley, P. J. Secondary Nucleation of Sodium Chlorate: The Role of Initial Breeding. *Cryst. Growth Des.* **19**, 3453–3460 (2019).

48. Buhse, T., Durand, D., Kondepudi, D., Laudadio, J. & Spilker, S. Chiral Symmetry Breaking in Crystallization: The Role of Convection. *Phys. Rev. Lett.* **84**, 4405–4408 (2000).

49. Ni, X., Shepherd, R., Whitehead, J. & Liu, T. Chiral symmetry breaking due to impeller size in cooling crystallization of sodium chlorate. *CrystEngComm.* **20**, 6894–6899 (2018).

50. Chen, W. C., Liu, D. D., Ma, W. Y., Xie, A. Y. & Fang, J. The determination of solute distribution during growth and dissolution of $NaClO_3$ crystals: the growth of large crystals. *J. Cryst. Growth.* **236**, 413–419 (2002).

51. Hosoya, S., Kitamura, M. & Miyata, T. Growth mechanisms of $NaClO_3$ and KBr from aqueous solutions under relatively high supersaturation ranges. *Mineralogical Journal.* **9**, 147–168 (1978).

52. Kitamura, M., Kouchi, A., Hosoya, S. & Sunagawa, I. Growth and dissolution of $NaClO_3$ crystal in aqueous solutions. *Mineralogical Journal.* **11**, 119–137 (1982).

53. Cruz, J. *et al.* Non-stochastic behavior in sodium chlorate crystallization. *Chirality.* **32**, 120–134 (2020).

54. Plasson, R., Brandenburg, A., Jullien, L. & Bersini, H. Autocatalyses. *J. Phys. Chem. A.* **115**, 8073–8085 (2011).

55. Frank, F. C. On spontaneous asymmetric synthesis. *Biochem. Biophys. Acta.* **11**, 459–463 (1953).

56. Steendam, R. R. E. *et al.* Linear Deracemization Kinetics during Viedma Ripening: Autocatalysis Overruled by Chiral Additives. *Cryst. Growth Des.* **15**, 1975–1982 (2015).

57. *SHAPE software*. (2004).

58. Leeman, M., Kaptein, B. & Kellogg, R. M. Nucleation inhibition in attrition-enhanced Pope-Peachey type of diastereomeric resolutions. *Tetrahedron- Asymmetry*. **20**, 1363–1364 (2009).

59. Titiz-Sargut, S. & Ulrich, J. Influence of Additives on the Width of the Metastable Zone. *Cryst. Growth Des.* **2**, 371–374 (2002).

60. Breveglieri, F. & Mazzotti, M. Role of Racemization Kinetics in the Deracemization Process via Temperature Cycles. *Cryst. Growth Des.* **19**, 3551–3558 (2019).

61. Cameli, F., ter Horst, J. H., Steendam, R. R. E., Xiouras, C. & Stefanidis, G. D. On the Effect of Secondary Nucleation on Deracemization via Temperature cycles. *Chem. Eur. J.* **26**, 1344-1354 (2020).

62. Schindler, M., Brandel, C., Kim, W.-S. & Coquerel, G. Temperature cycling induced deracemization (TCID) of $NaClO_3$ under the influence of $Na_2S_2O_6$. *Cryst. Growth Des.* **20**, 414–421 (2019).

63. Bodák, B., Maggioni, G. M. & Mazzotti, M. Population-Based Mathematical Model of Solid-State Deracemization via Temperature Cycles. *Cryst. Growth Des.* **18**, 7122–7131 (2018).

64. Steendam, R. R. E. & ter Horst, J. H. Scaling Up Temperature Cycling-Induced Deracemization by Suppressing Nonstereoselective Processes. *Cryst. Growth Des.* **18**, 3008–3015 (2018).

Chapter IV Couette Taylor Reactor

Implementation of the Deracemization and Perspectives

I. Introduction

The critical attributes of a crystallized material, *e.g.* structural purity, crystal morphology and crystal size distribution (CSD), an enantiomeric purity in case of enantioseparative crystallization, are governed by the crystallization procedure and by how nucleation, crystal growth and eventually: attrition-agglomeration occured.[1] In the particular case of deracemization by crystallization, the process is based on the repetitive dissolution & recrystallization cycles either ensured by attrition[2] or by temperature cycling.[3,4] The majority of reported deracemization processes was designed for batch procedures and relies on a careful control of temperature during the process. Concerning Temperature Cycling Induced Deracemization (TCID) performed in batch, an important drawback arises from the fact that it is quite difficult to scale up such process due to heat transfer problems:[5] Temperature is therefore difficult to control, possibly giving rise to a marked departure from the targeted critical attributes of the final product. It is thus necessary to circumvent this issue in order to achieve easy scale up of TCID.

In 1977, Kataoka showed highly efficient heat and mass transfer phenomena in a Couette Taylor (CT) reactor, *i.e.* a reactor in which a fluid circulates in the gap between two concentric cylinders.[6,7] Therefore, such reactors have a high potential in the field of continuous flow processes.[8] However, it is only recently that CT reactors have been considered for crystallization and deracemization processes.[9,10] Indeed, even though the first report of the occurrence of a unique periodic hydrodynamic fluid motion (*i.e.* Taylor vortex flow) in a CT reactor dates back from the end of the 19th century,[11] the first studies on the influence of such fluid motion on crystallization were published 20 years ago.[12,13] Crystallization experiments performed in a CT reactor highlighted that Taylor vortex flow has a marked incidence on nucleation and growth mechanisms, crystal morphology, phase transformation, and on agglomeration.[10,12,14–18] Moreover, even if the design of chemical reactions have been considered in CT reactors,[12,14,16,19] enantiomer resolutions *via* crystallization based methods in such reactors has been seldom investigated.[9]

Thus, in order to further investigate TCID, a CT reactor has been implemented in the laboratory and used for $NaClO_3$ deracemization. The selection of this compound, initially used as a model compound by Viedma,[20] enables to compare the results obtained in the CT reactor with those obtained in batch by attrition or by temperature cycling, presented in the third chapter.

II.State of the Art

A. History

In 1890 Couette considered the fluid flow between two concentric cylinders with a rotating outer cylinder.[11] Afterwards, numerous parameters were studied such as the outer cylinder rotation speed, the viscosity of the fluid, the cylinder radii, the gap width between the cylinders, the cylinder actually rotating (inner and/or outer), and, in case both cylinders were rotating, the respective direction of rotations (rotations in opposite or in the same direction).[21–24] All authors observed the occurrence of instability in the flow when the rotation speed was sufficient. Among them, Taylor theoretically and experimentally explained the nature of this instability by highlighting the development of specific vortices in the liquid.[24] Taylor described square vortices where size equals the gap size between the cylinders. Two neighboring vortices have opposite rotation directions (Figure IV-1).

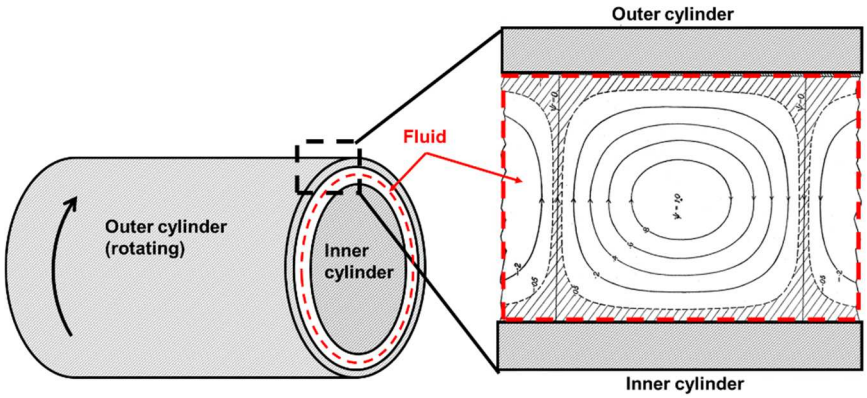

Figure IV-1 : Side view of vortices produced by the first instability in the flow between two concentric cylinders described by Taylor in 1923.[24]

Later on, when the rotation speed was further increased, Coles and Fenrstermacher highlighted the occurrence of further other instabilities, up to the turbulent flow regime.[25–27]

From the Couette study and the Taylor vortex flow description, reactors made of two concentric cylinders with rotation of one of them are now called Couette Taylor (CT) reactors.

B. Fluid Dynamics in Couette Taylor Reactor

1. Reynolds and Taylor Numbers

Fluid dynamics are described as a function of the flow regime (of the liquid or suspension) which range from laminar (the flow is along parallel layers of the fluid) to turbulent flow (where movements of the fluid layers are chaotic). To characterize the flow in standard cylinders or stirred tank reactors, the Reynolds number (Re) is commonly used. It is a dimensionless value and is calculated from the velocity and the viscosity of a fluid and the hydraulic diameter (Equation IV-1). Laminar flow is characterized by low Re (Re < 2000) while higher Re (Re > 4000) stand for turbulent flow.

$$Re = \frac{V*D}{\upsilon} \qquad \textit{Equation IV-1}$$

Where:

- V: velocity of the fluid ($m.s^{-1}$)
- D: diameter of the cylinders (m)
- υ: the kinematic viscosity of the fluid ($m^2.s^{-1}$)

In a CT reactor, the flow is rather characterized by the Taylor number (Ta) and the peculiar flows involved in CT reactors are categorized according to Ta values. Ta is related to the centrifugal and the viscous forces, and is dependent on the geometry of the reactor, the rotation of the internal cylinder and on the dynamic viscosity of the fluid (Equation IV-2).[24]

$$Ta = \left(\frac{R_1\Omega(R_2 - R_1)}{\upsilon}\right)^2 \qquad \textit{Equation IV-2}$$

Where :

- R_1: the inner cylinder diameter (m)
- R_2: the outer cylinder diameter (m)
- Ω: the rotation rate of the inner cylinder (s^{-1})
- υ: the kinematic viscosity of the fluid ($m^2.s^{-1}$)

A critical value of Ta, Ta_c (Equation IV-3), has been described and delimits flow regimes. This specific value is mainly dependent on the diameters of the cylinders.[24]

$$Ta_c = \frac{R_2 - R_1}{R_1} * \left(\frac{\pi^4 \left(1 + \frac{R_2 - R_1}{2R_1}\right)}{0{,}0571\left(1 - 0{,}652\left(\frac{R_2 - R_1}{R_1}\right)\right) + 0{,}00056\left(1 - 0{,}652\left(\frac{R_2 - R_1}{R_1}\right)\right)^{-1}} \right)^2$$ Equation IV-3

2. Flow Regimes

Different flow regimes in CT were described according to Ta and Ta_c, directly related to the rotation rate of the inner cylinder and to the cylinder radii of the CT reactor. In the case of an inner cylinder rotating and an outer cylinder at rest, these regimes are described as follows:[9]

Couette flow: For low rotation speeds, $Ta < Ta_c$ and the flow is established along symmetric rings around the rotation axis. This flow is laminar.

Taylor vortex flow: When $Ta_c < Ta < 3Ta_c$, although the flow is still laminar, first instabilities appear and produce toroidal vortices, called Taylor vortices, represented in Figure IV-2.

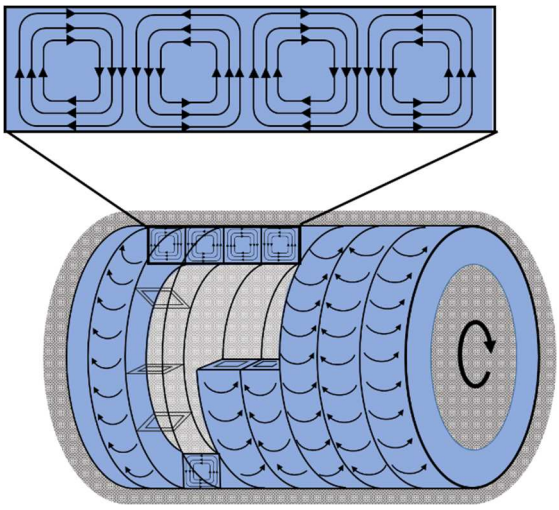

Figure IV-2: Schematic representation of Taylor vortex flow in the CT reactor

Vortex cells are periodically arranged along the axial direction as the outer cylinder is fixed and the inner cylinder rotates. Boundaries between vortex cells are perpendicular to the cylindrical axis.[28] Two vortex cells side by side are counter rotating, heat and mass transfer/exchange are favored at those boundary layers.[6,7]

Wavy vortex flow: For higher rotation rates, $3Ta_c < Ta < 18Ta_c$ a second instability is added to the flow. Vortices are slightly distorted by waves, boundaries are no longer perpendicular to the cylindrical axis.[28] When Ta further increases, wave frequencies increase until the occurrence of a chaotic wavy vortex flow.

Turbulent vortex flow: For $18Ta_c < Ta < 160Ta_c$, previously described waves disappear and vortices are similar to Taylor vortices. However, speed fluctuations in vortices make the flow turbulent.

Turbulent flow: Flow is fully turbulent, $Ta > 160Ta_c$ and the Taylor vortex structures are no longer observable.

C. Crystallization and Deracemization in Couette Taylor Reactor

Concerning crystallization, the unique periodic flow properties of a Taylor vortex flow can provide a robust control of the structural purity, the morphology, the mean crystal size and the crystal size distribution (CSD), giving rise to a narrower and higher CSD,[8,29] of crystallized compounds.[10–15] Parameters, such as the temperature, the rotation speed, the reactor geometry, have to be mindfully determined from the purpose of the crystallization procedure.

A recent study showed that applying a temperature gap ΔT (thus generating a temperature gradient in the fluid) between the cylinders of the CT reactor, separately thermostated, provide a promising control over the CSD.[29] The authors found that the use of ΔT enlarges the mean crystal size and narrows the CSD. They also investigated the impact of the direction of the temperature gradient and have shown that the influence is even more marked for hot inner and cold outer cylinders.

Kim *et al.*[9] patented the use of the CT reactor to conduct deracemization of various compounds. Inventors also found that deracemization was hastened in non-isothermal mode in the CT reactor. Actually, by using different temperatures for the inner cylinder and the outer cylinder, crystals undergo billions of temperature cycles in the CT reactor, which might afford a similar (or maybe more effective) effect to that of the temperature cycling in batch process, *i.e.* TCID process.[3,9,29]

III. Implementation of Couette Taylor Reactor

A. Description of the Reactor

The CT reactor used in this work is schematically represented in Figure IV-3. The reactor is composed of two concentric cylinders between which a solution or a suspension of crystals flows. In this study, the inner cylinder (radius R_1 = 19.5 mm) rotates at controlled rotation rate and the outer cylinder (radius R_2 = 23.4 mm) is at rest. The total length is 196 mm. The reactor is made of hastelloy, resistant to corrosion and mechanical stresses. Two different thermostats independently control the temperature of both cylinders.

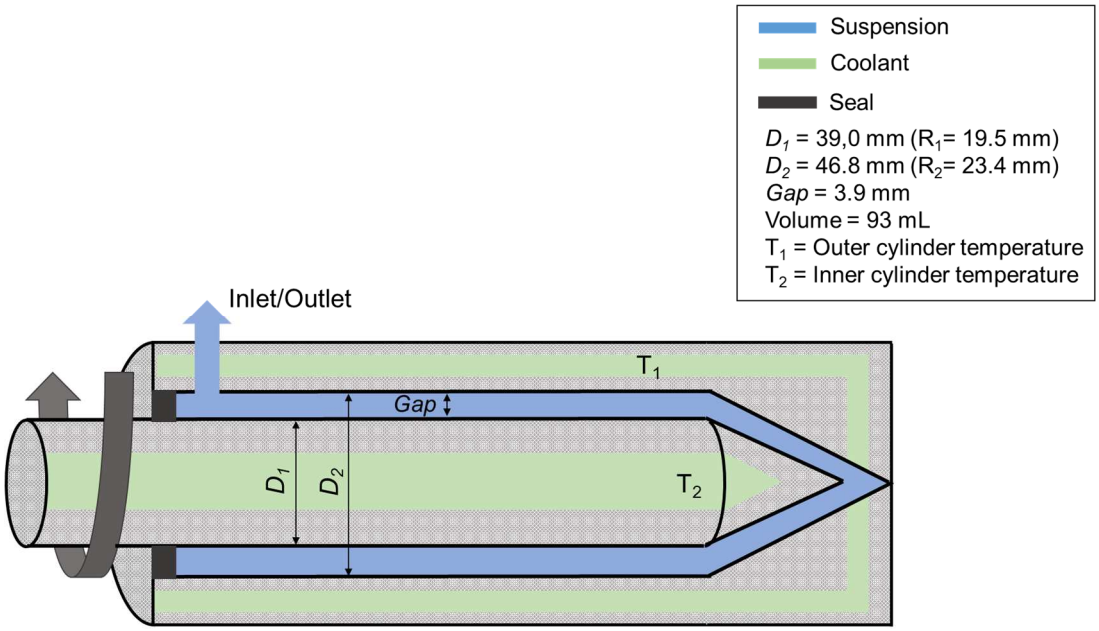

Figure IV-3 : Schematic representation of the Couette Taylor reactor. The inlay details parameters of the reactor used in this study.

In addition to the inlet/outlet, three ports at the top of the reactor are available to inject reactant, to sample the system, or to plug various probes (temperature, pH …).

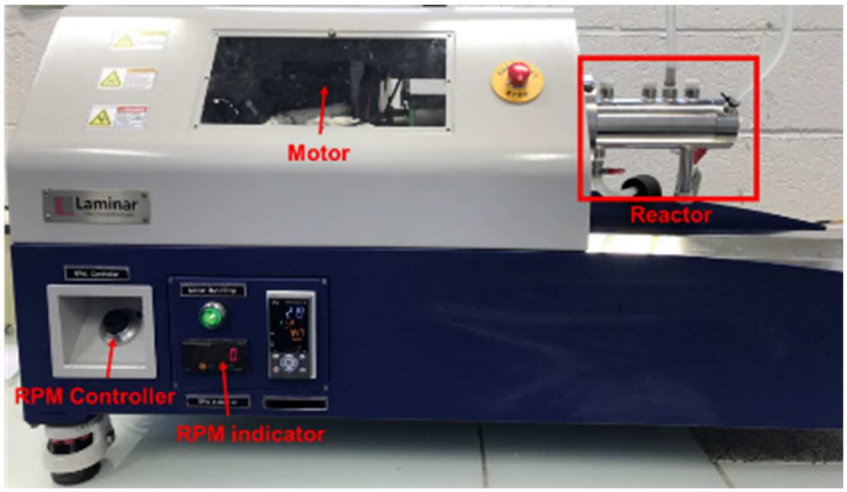

Figure IV-4 : Photo of the whole Couette Taylor apparatus implemented in the laboratory.

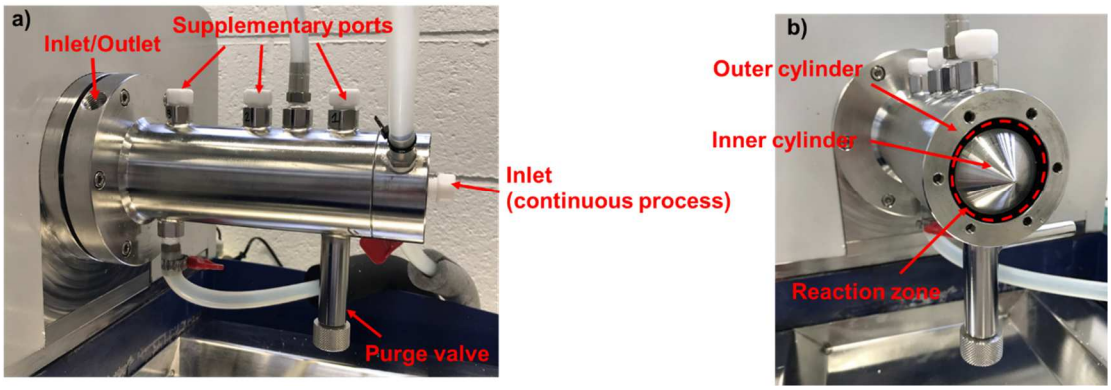

Figure IV-5 : Photos of the Couette Taylor reactor a) closed and b) opened, where the reaction zone is visible.

B. Technical Issues

The seal (yellow part in Figure IV-6) is made of Teflon and ensures sealing between the inner and the outer cylinder at the end of the reactor. The seal is mounted on the outer cylinder (Figure IV-6) and the inner cylinder rotates through the seal. Due to the mechanical stress generated by the rotation, the inner part of the seal is damaged after few hours of experiment and a leak was systematically observed in every experiment. The seal had to be changed after each experiment. This technical difficulty prevented experiment longer than 3 days.

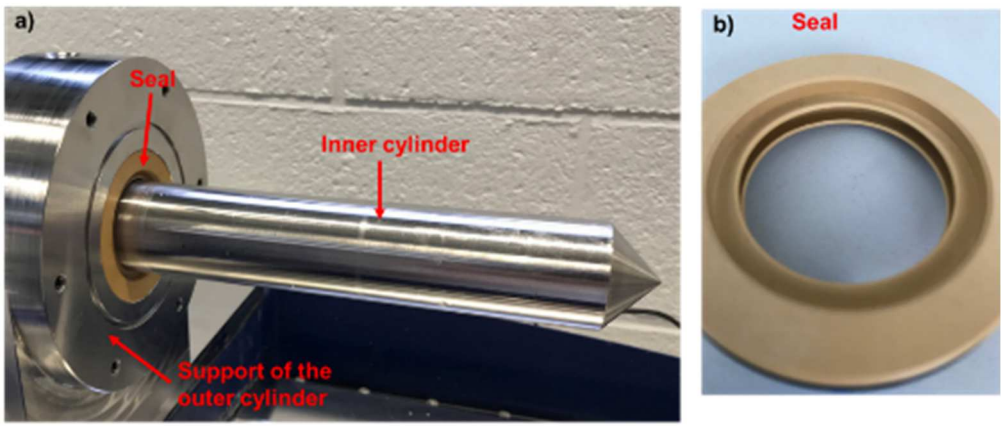

Figure IV-6 : a) Photo of the inner cylinder without the outer cylinder, highlighting the yellow seal and b) photo of the disassembled seal.

IV. Preliminary Experiments of $NaClO_3$ Deracemization in the CT Reactor

In this work, experiments were focused on $NaClO_3$ deracemization using non-isothermal mode, *i.e.* using a ΔT between the inner and the outer cylinders, in the CT reactor. Indeed, crystals are then continuously driven by Taylor vortex cells close to the hot surface (*i.e.* surface of the hot inner cylinder) and then to the cold surface (*i.e.* surface of the cold outer cylinder) which likely generates billions of temperature cycles for each individual crystal and should enhance the dissolution, crystallization and thus deracemization.[3,9,29] Parameters, such as the initial crystal size, the magnitude of ΔT and the rotation speed of the inner cylinder, were investigated to enhance deracemization in the CT reactor.

A. Sample Preparation

Commercial $NaClO_3$ (≥98%, Alfa Aesar) was recrystallized *via* Kondepudi's method,[31] dried in a ventilated oven, ground and sieved before using in experiments, as described in the third chapter of this manuscript. A stock of saturated solution at 20°C was prepared by mixing an excess of recrystallized $NaClO_3$ in pure water at 20°C and filtering the supernatant. The suspension for deracemization experiments was prepared by weighting 25g of each homochiral population of sieved crystals to obtain 50g of racemic mixture (CEE = 0%) with controlled crystal size in 100mL of saturated solution. The suspension density corresponds to the suspension density used in the TCID processes of this work (See Chapter 3). The suspension of $NaClO_3$ crystals in saturated aqueous solution was stirred

in a beaker, withdrawn with a syringe and injected in the CT reactor *via* the inlet/outlet (Figure IV-5).

B. Experimental Conditions

Three parameters (i) the initial crystal size ($\varnothing_{particles}$), (ii) the magnitude of the temperature gap between cylinders of the CT reactor (ΔT) and (iii) the rotation rate (Ω) of the inner cylinder, were investigated during the deracemization experiments, as follows:

- Initial crystal size, $\varnothing_{particles}$: $\mathbf{25 < \varnothing_{particles} < 32\ \mu m}$ or $\mathbf{32 < \varnothing_{particles} < 50}$ µm (with ΔT and Ω fixed)
- Temperature gap, $\Delta T = T_{inner} - T_{outer}$ (the inner cylinder is hotter than the outer) : **10°C**, **20°C** or **30°C**
- Rotation speed, Ω: **600 rpm** or **1200 rpm**.

In order to maintain an average temperature of the suspension close to 20°C in the reactor for all experiments, the temperatures of the cylinders were set as a function of the desired ΔT and centered around 20°C, *e.g.* for ΔT = 10°C, the inner cylinder temperature was set at 25°C and the outer cylinder temperature at 15°C. A summary of the experiments performed is given in Table IV-1.

Table IV-1 : Summary of deracemization experiments performed in the CT reactor according to the initial size of particles ($\varnothing_{particles}$), the ΔT and the Ω.

Exp.	$\varnothing_{particles}$ (µm)	ΔT (°C)	Ω (rpm)
0	$32 < \varnothing < 50$	10	1200
I	$25 < \varnothing < 32$	10	1200
II	$25 < \varnothing < 32$	20	100
III	$25 < \varnothing < 32$	20	600
IV	$25 < \varnothing < 32$	10	600
V	$25 < \varnothing < 32$	30	1200

To follow the deracemization kinetics, the evolution of the CEE was monitored by sampling a minimal amount of the suspension (~0.5mL) to identify the handedness of the crystals using the procedure described in Chapter III.[20]

C. Results

1. Influence of the Initial Crystal Size

At fixed $\Delta T = 10°C$ and $\Omega = 1200$ rpm, two initial populations, $32 < \varnothing_{particles} < 50$ µm (Exp. 0) and $25 < \varnothing_{particles} < 32$ µm (Exp. I), were investigated for deracemization experiments in the CT reactor. Results are shown in Figure IV-7.

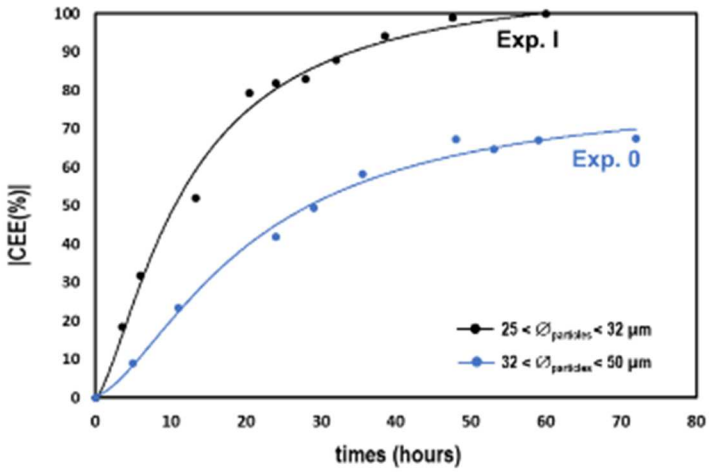

Figure IV-7: Evolution of the absolute value of CEE of $NaClO_3$ as a function of time for deracemization experiments in the CT reactor. The lines are guides to the eyes. Inlay indicates the initial particle crystal size.

Total symmetry breaking occurred for the smaller initial population ($25 < \varnothing_{particles} < 32$ µm) under 48 hours. However the CEE was blocked at 67% for the larger initial population ($32 < \varnothing_{particles} < 50$ µm). Observation under polarized optical microscopy (POM) to determine the CEE of the samples showed a large increase of crystal size during the experiments, in particular during Exp. 0 (Figure IV-8).

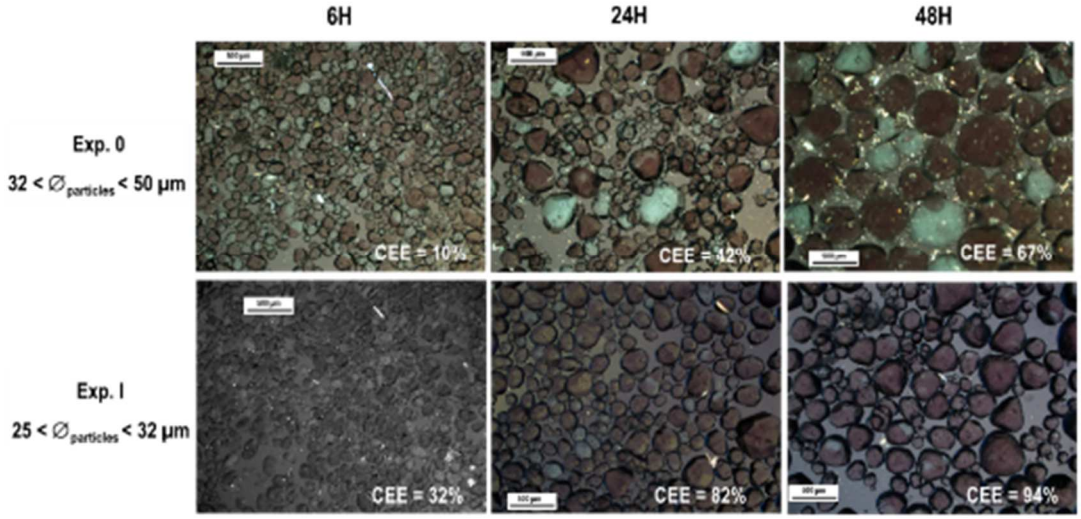

Figure IV-8 : POM Pictures of $NaClO_3$ crystals after 6, 24 and 48 hours in the deracemization experiments in the CT reactor for initial crystal size between 32 and 50 µm (top), and for initial crystal size between 25 and 32 (bottom). The inlays indicate the %CEE.

For Exp. 0, the evolution of the CEE is slower than in Exp. I. Indeed, at 6 hours, the CEE gap between Exp 0 and Exp. I is 22% and is even more significant at 24 hours (40%). POM pictures of crystals from Exp. 0 at 24 hours (CEE = 42%) show large crystals of both chiralities and these crystals survived until the end of the experiment, locking the CEE around 67%. Furthermore, for Exp. I, at 24 hours, minor enantiomorphic crystals (blue crystals) are small and disappear at the end of the experiment giving rise to total deracemization.

From these results, further experiments to assess the impact of the other parameters were performed using the smallest initial crystal size, $25 < \varnothing_{particles} < 32$ µm.

2. Influence of the ΔT and the Ω

Several ΔT (10, 20 and 30°C) and Ω (600 and 1200 rpm) values were investigated and the results of these experiments are gathered in Figure IV-9.

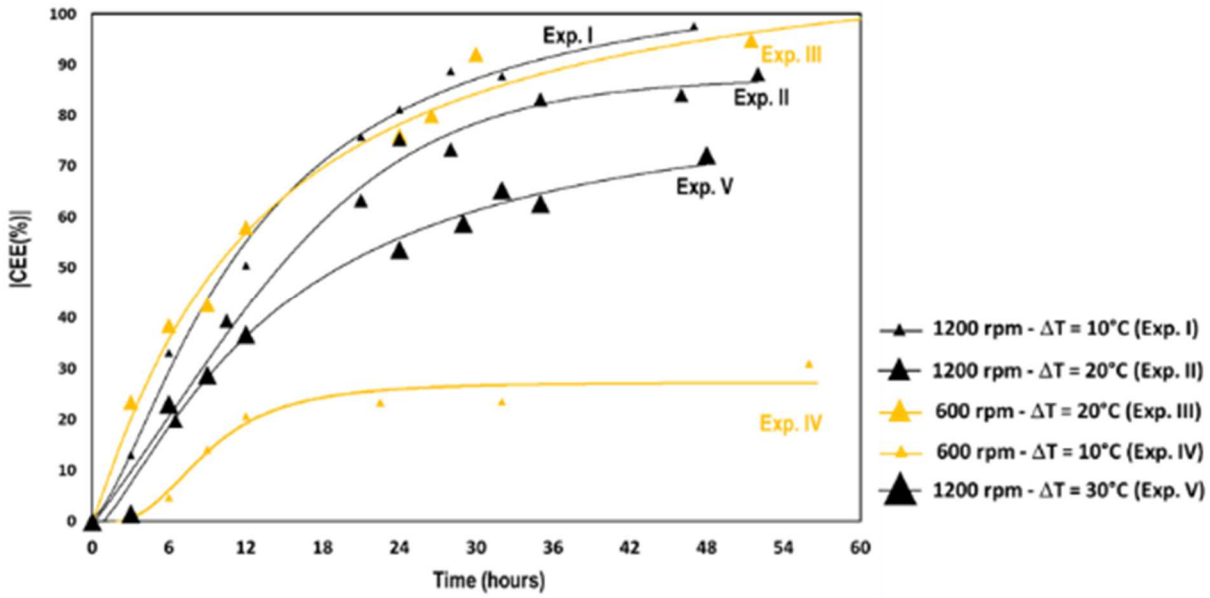

Figure IV-9 : Evolution of the absolute value of CEE of NaClO3 as a function of time for deracemization experiments in the CT reactor. The lines are guides to the eyes. Inlay indicates the rotation rate (ω) and the ΔT between set temperatures of cylinders.

Experiments I and III presented similar deracemization kinetics and total chiral symmetry breaking occurred under 48 hours. At a fixed ΔT of 10°C, deracemization is favored by *higher* Ω (Exp. I and IV, Figure IV-9). At a fixed ΔT of 20°C, deracemization is favored by *lower* Ω (Exp. II and III, Figure IV-9*)*. The lower Ω with the smaller ΔT (Exp. IV) are the less efficient conditions, with the CEE quickly blocked around 23% *(*Figure IV-9). In addition, the higher Ω with the larger ΔT (Exp. V), did not induce total deracemization as the CEE was blocked at 70% (Figure IV-9). At a fixed Ω = 1200 rpm, deracemization is favored by lower ΔT. Indeed, Exp. I, II and V showed that the increase of ΔT from 10 to 30°C induced less efficient deracemization with final CEE at 98%, 84% and 70% respectively.

As for previous experiments (Exp. 0 and I), marked growth of the crystals in suspension was observed in all experiments (Figure IV-10).

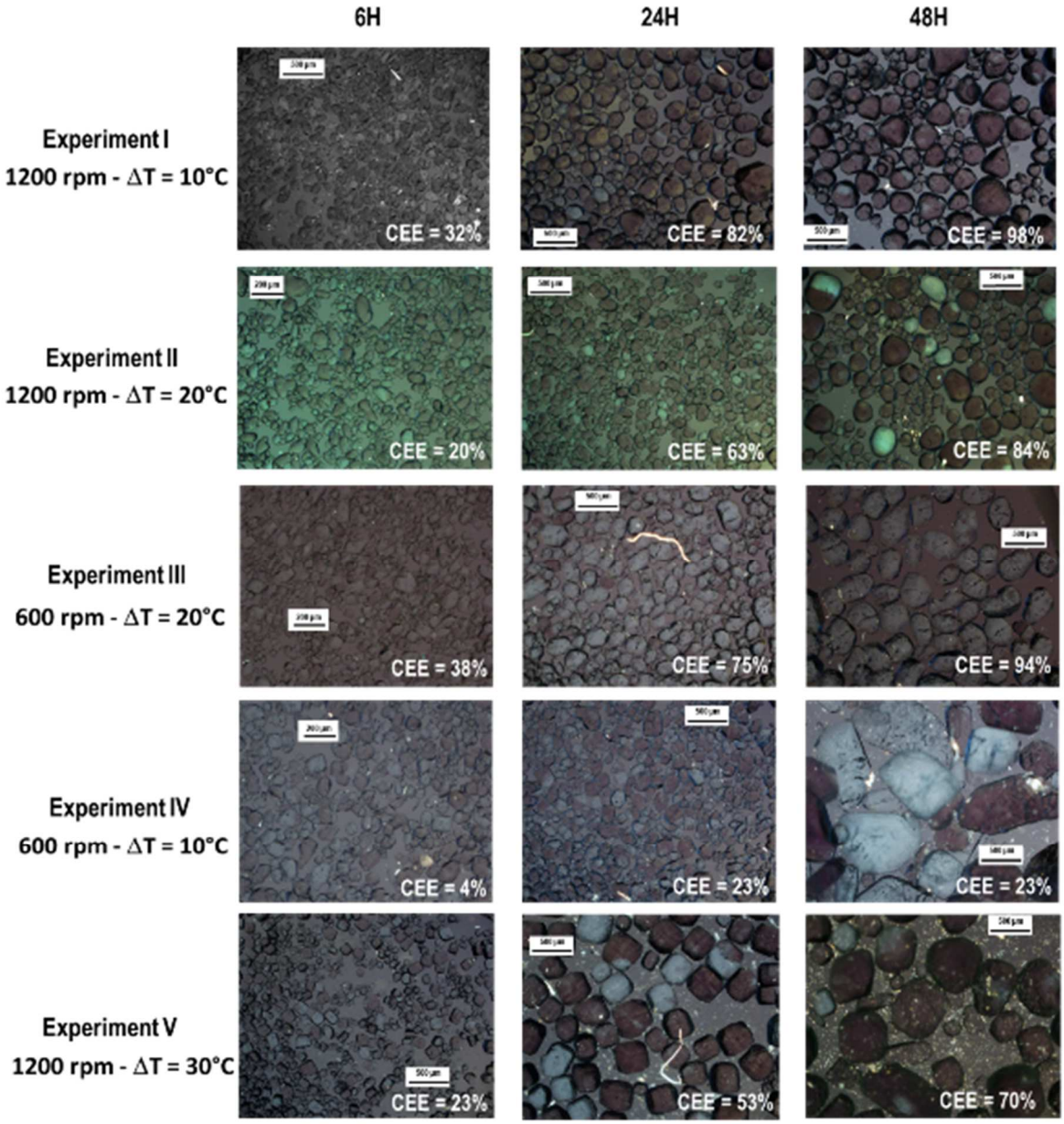

Figure IV-10 : POM pictures of $NaClO_3$ crystals after 6, 24 and 48 hours of deracemization experiments as a function of ΔT and Ω (conditions shown on the left side). The inlays indicate the %CEE.

POM pictures of crystals during deracemization experiments (Figure IV-10) showed much larger crystals (600 < ∅ < 800 µm) for the less effective conditions (Exp. IV and V, Figure IV-10). In case of Exp. I, II and III, the final CEE is circa 90% and the crystals have roughly the same size (∅ < 400 µm). It is worth noting that, whatever the conditions, 100% CEE was never reached. This is explained by the systematic occurrence of particles presenting both chiralities (Figure IV-11). These particles were counted twice in the determination of the CEE, once as *l*-crystal and once as *d*-crystal.

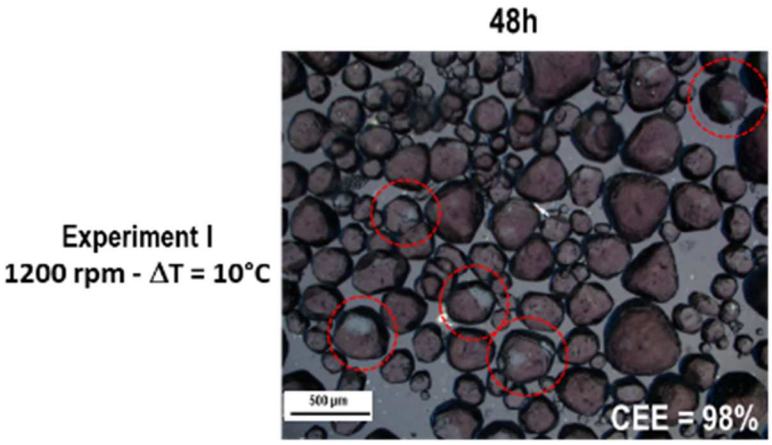

Figure IV-11 : POM picture of crystals from Exp. I at 48 hours, crystals with both chiralities are circled in red.

Even if such crystals remain minor in most experiments, we have experienced cases (not presented here) where almost every particle consisted of both chiralities (Figure IV-12). Such specific cases of heterochiral agglomeration obviously jeopardize the complete disappearance of one of the two chiralities.

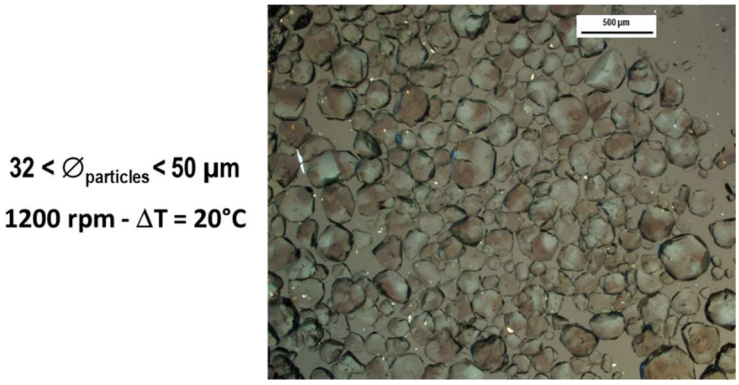

Figure IV-12 : POM Pictures of $NaClO_3$ crystals after 16 hours in the deracemization experiment in the CT reactor for initial crystal size between 32 and 50 µm (top), Ω = 1200 rpm and ΔT = 20°C.

Even if these particles resemble the inversion twinning of $NaClO_3$ reported by Lan *et al.* in the presence of $Na_2S_2O_6$,[32] the crystals presented in Figure IV-10 and Figure IV-11 have been obtained in experiments free from this impurity. The two chiral domains do not appear to be oriented with each other according to any specific crystallographic orientation, which suggests an agglomeration of enantiomorphic crystals instead of twinning. Further to this, what looks like the same phenomenon has been reported by Steendam *et al.*[5] during TCID of $NaBrO_3$. In their experiments, authors solved this agglomeration issue by an efficient mixing which broke the heterochiral agglomerates. Therefore, it can be supposed that mixing in the CT reactor is not powerful enough to

break the agglomerates, which is further supported by the marked propensity of the crystals to grow up to a quite large size without breakage.

D. Influence of $Na_2S_2O_6$ on the $NaClO_3$ Deracemization in the CT Reactor

Similarly to the batch experiments performed and reported in Chapter 3, $Na_2S_2O_6$ has been used as an impurity during deracemization experiments in the CT reactor. The main objective of this work was to assess the impact of $Na_2S_2O_6$ under these conditions and to check if the specific flow properties of a CT reactor can speed up the deracemization procedure notwithstanding the antagonist effect of the impurity.

1. Experimental Conditions

Using the most efficient conditions previously identified (*i.e.* $\Delta T = 10°C$ and $\Omega = 1200$ rpm), 0.5% mol of $Na_2S_2O_6$ (*i.e.* 1,10g of $Na_2S_2O_6,2H_2O$), were added at the beginning of the experiment. The $Na_2S_2O_6$ used in this part was synthesized as described in the second chapter of this manuscript.

2. Results

POM observation of the crystals during the experiment performed in the presence of 0.5% mol of $Na_2S_2O_6$ (Figure IV-13) showed that the $NaClO_3$ crystals almost did not grow during the experiment and that the CEE remained 0%.

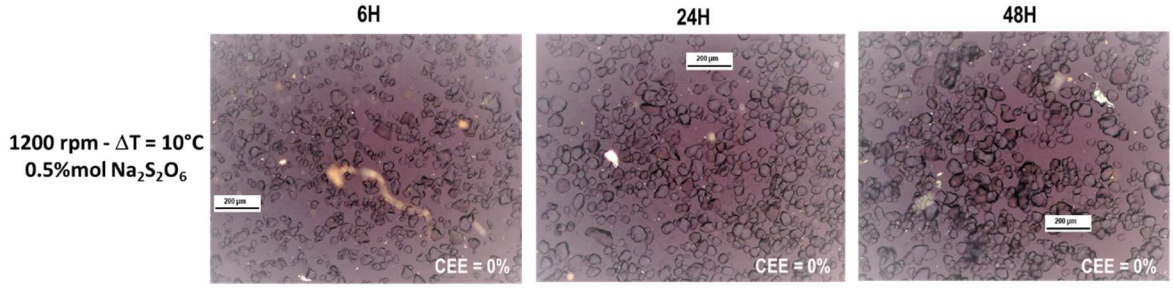

Figure IV-13 : POM picture of $NaClO_3$ crystals after 6, 24 and 48 hours of deracemization experiment in the presence of 0.5%mol of $Na_2S_2O_6$. Inlays indicate the %CEE.

In comparison, batch $NaClO_3$ deracemization experiments performed in round-bottom flask with 0.5%mol of $Na_2S_2O_6$ (see Chapter 3), showed a very sluggish increase of the CEE. In the CT reactor and under these conditions, deracemization of $NaClO_3$ is fully prevented by the presence of 0.5%mol of $Na_2S_2O_6$ (Figure IV-13).

It is also noteworthy that if most deracemizations performed without $Na_2S_2O_6$ were jeopardized because of the occurrence of too large crystals in the CT reactor (Exp, IV and V, Figure IV-9), oppositely, the presence of $Na_2S_2O_6$ hampers symmetry breaking by preventing crystal growth (Figure IV-13).

E. Discussion

Almost all experiments performed in the CT reactor using pure $NaClO_3$ were characterized by a marked growth of the crystals. Since the average temperature was maintained constant (T = 20°C) during all experiments, it is reasonable to state that no significant supersaturation was generated in the CT reactor and that any form of primary nucleation was unlikely under our operating conditions. Thus, the marked growth in the CT reactor was mainly a consequence of Ostwald ripening.[33] This assertion is further supported by the fact that the mass transfer between liquid and solid phases is strongly improved in the Taylor vortices of the reactor.[15,17] The mass transfer here is the diffusion of solvated ions from the solution to the crystal surfaces, thus it is directly correlated to the crystal growth.[34] In the absence of crystal growth, *i.e.* in the presence of $Na_2S_2O_6$ preventing the growth, chiral symmetry breaking cannot occur. Therefore, the evolution of the CEE in CT reactor is closely dependent on the crystal growth, *i.e.* Ostwald ripening.

Nonetheless, Ostwald ripening is required but is not sufficient to induce total chiral symmetry breaking, as shown in experiments IV and V of this work (Exp. IV and V, Figure IV-10) in which excessive crystal growth of both chiralities without restraint blocked CEE at a scalemic (*i.e.*, no racemic) value. Actually, numerous studies focused on deracemization mechanisms, including experimental work and modelling,[3,20,35–38] confirm that Ostwald ripening alone is not sufficient to induce total chiral symmetry breaking and evidence the necessity of a continuous formation of small chiral crystals (*i.e.* a crystal recycling)[36]. For attrition enhanced deracemization processes, the powerful mixing and abrasion ensure the continuous production of smaller crystals and chiral clusters[39] alike secondary nucleation in TCID experiments upon the cooling stage.[38,40,41] Thus, it is suspected that there is another phenomenon that takes place during experiments I and III (Figure IV-9), which provides the feed material to Ostwald ripening and which ensures almost total symmetry breaking. One can also note that total symmetry breaking occurred only for suitable combinations of ΔT and Ω, *i.e.* the smaller ΔT combined with the higher Ω or the larger ΔT combined with the lower Ω.

Wu et al.[29] evidenced a shift of the crystal size distribution (CSD) towards big crystals under non isothermal mode in the CT reactor. However, as highlighted by the authors, temperature cycles could have different effects according to the solubility curve and the metastable zone width (the Ostwald limit) of the compound in the solvent. Indeed, the temperature cycles, produced in Taylor vortex cells between the cold outer cylinder and the hot inner cylinder, could either enhance Ostwald ripening, improving crystallinity and crystal growth, if the system stays in the metastable zone upon cooling, close to the solubility curve (Figure IV-14, 'a' profile),[42] or produce nucleation when faster cooling rates (and/or higher ΔT) produce higher supersaturation (Figure IV-14, 'b' profile).

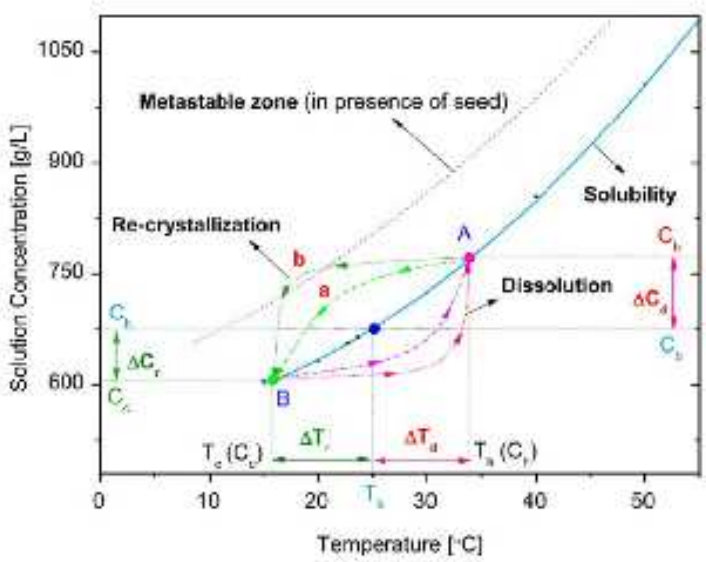

Figure IV-14 : Schematic representation of internal heating-cooling cycles, i.e. temperature cycles, in non-isothermal CT reactor, where A and B are solubility at the hotter and the colder temperature respectively and the blue point, the solubility at the temperature of the suspension. For the supersaturation following the 'a' profile, Ostwald ripening is enhanced, i.e. crystal growth, without nucleation and for the supersaturation following the 'b' profile, nucleation occurs.[29]

Depending on other parameters such as the rotation speed or the gap size, Wu et al. described an experimental limit value of ΔT. Below this limit, the system stays in the metastable zone favoring the crystal growth with the larger the ΔT, the higher and narrower the CSD ('a' profile, Figure IV-14). Above this limit, secondary nucleation occurs and the larger the ΔT, the smaller the CSD ('b' profile, Figure IV-14). Also quite counterintuitively, the higher the Ω, the higher the ΔT limit which is explained by the enhancement of the mass transfer in CT reactors at higher Ω favoring crystal growth by Ostwald ripening over nucleation events.[6,7] For instance, they determined that this limit at 600 rpm is ΔT = 12.5°C whereas at 900 rpm, the limit is ΔT = 17.5°C [29]

From our experiments, the results obtained at Ω = 600 rpm in the CT reactor are consistent with this observation: At the lower ΔT value of 10°C (Exp. IV), the system probably stays in the metastable zone and the temperature cycles favor the growth of the crystal at the expense of secondary nucleation. At the higher ΔT value of 20°C (Exp. III), secondary nucleation could occur, preventing excessive crystal growth, which favors deracemization.

Nevertheless, at higher Ω, here 1200 rpm, our results show that the higher the ΔT, the higher the mean CSD and the less efficient is deracemization (Exp I, II and V). It appears that the system stays in the metastable zone even at ΔT = 30°C: there is no, or not enough, secondary nucleation to ensure an efficient crystal recycling and deracemization is blocked by the growth of very large particles (see Figure IV-10). However, the total symmetry breaking occurring in the Exp. I, *i.e.* at ΔT = 10°C, suggests that an optimum combination of ΔT and Ω leads to total deracemization, thus, another phenomenon should happen to ensure the crystal recycling at lower ΔT. Therefore, other ΔT should be tested at high Ω, either close to zero to reduce mass transfer and to fully grasp the other involved phenomenon, or at very high ΔT (*i.e.*, > 30°C) to favor secondary nucleation over crystal ripening.

Indeed, at low Ω, here 600 rpm, and ΔT = 20°C, the effective temperature oscillations undergone by the crystals are logically much greater than that at 1200 rpm and ΔT = 10°C. As deracemization did not occur at 1200 rpm and ΔT = 20°C or 30°C, we could surmise that two different mechanisms might be involved in deracemization by using CT reactor.

To summarize our hypotheses, crystal growth remains an essential factor for deracemization in the CT reactor since the presence of $Na_2S_2O_6$ in the experiments showed that the hindrance of crystal growth prevents the evolution of the CEE. Therefore, there is a competition between the secondary nucleation and crystal growth which has to be controlled by the choice of a suitable ΔT and Ω. As in TCID process (see chapter 3), the success of deracemization is a balance between crystal growth and secondary nucleation.

Another important phenomenon observed in these experiments is the agglomeration of crystals. Indeed, Taylor vortices enhance not only mass transfer but also aggregation of crystals. Crystals form aggregates under collisions and/or because of close parallel trajectories. They are converted to agglomerates by means of crystal growth.[17] Although $NaClO_3$ crystals do not tend to agglomerate in usual crystallization/deracemization experiments, the peculiar fluid dynamics involved in the CT reactor favor $NaClO_3$ crystal agglomerations. Mayra and Kim described an effective decrease of crystal agglomerations

by reducing the gap size of the reactor.[17] Indeed, narrower gap size induced a higher shear forces and reduced the crystal size *via* breakage of crystals, which may be an advantage for deracemization.

In a collaborative work, Professor Kim's group[10] also performed deracemization experiments in their own CT reactor. Their reactor has larger radii and enables to change the inner cylinder to work with different gap sizes: 2 mm or 4 mm. Thus, we can consider the influence of the gap size on deracemization. For experiments presented hereafter, Professor Kim's group worked with the same density of suspension as our experiments, *i.e.* 50 g of racemic $NaClO_3$ crystals in 100 mL of saturated solution, and with ΔT =20°C. Cylinder radii and experimental conditions are gathered in the Table IV-2. Results of experiments performed with a gap size of 2 mm and with a gap size of 4 mm are presented in Figure IV-15.

Table IV-2 : Operating conditions (ΔT and Ω) and dimensions of CT reactor used by Professor Kim's group for $NaClO_3$ deracemization and used in our experiment for comparison.

CT reactors	Outer cylinder radius (mm)	Inner cylinder radius (mm)	Gap (mm)	ΔT (°C)	Ω (rpm)
Professor Kim's group work	64.0	62.0	2.0	20	378
	64.0	60.0	4.0	20	390
This work (for comparison)	23.4	19.5	3.9	20	1200 or 600

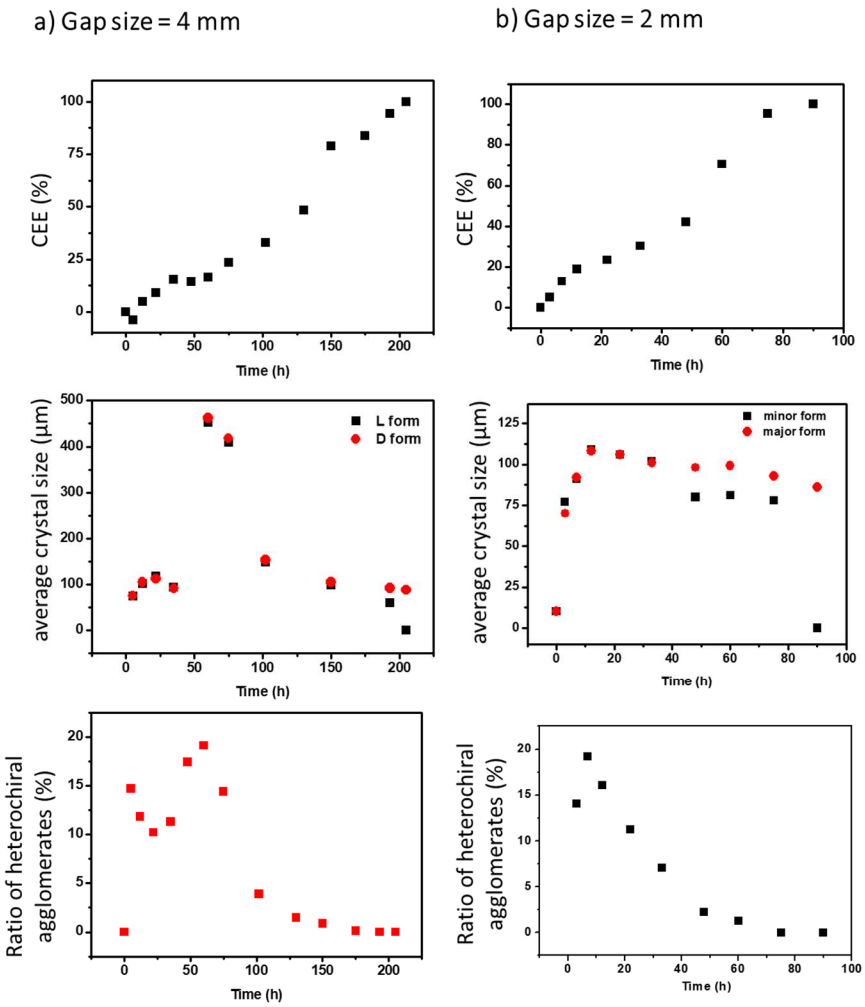

Figure IV-15 : Results of $NaClO_3$ deracemization experiments performed by Professor Kim's group in a CT reactor a) with a gap size of 4 mm and b) with a gap size of 2 mm. The CEE(%) (top), the average crystal size (middle) and the ratio of heterochiral agglomerates (over the total crystal number) (bottom) are presented as a function of the time (hours).

First, the large cylinder radii in their CT reactor increase the processing time of deracemization to 200 hours, compared to our experiments where deracemization occurred under 48 hours (Figure IV-9). However, as expected, deracemization is strongly influenced by the gap size. Indeed, results of Professor Kim's group showed that the required time for total deracemization is divided by more than 2, from 200 hours to 90 hours, when the gap size is divided by 2, from 4 mm to 2 mm (Figure IV-15).

In both cases, *i.e.* gap sizes of 2 and 4 mm, large crystal growth and formation of heterochiral agglomerates of $NaClO_3$ take place at early stages of the experiments, as in our experiments. For gap size of 4 mm, like in our reactor (Table IV-2), the average crystal size reaches ~450 µm (Figure IV-15-a), as in our experiments I, II and III (Figure IV-10). Then, after 10 hours for gap size of 2 mm and after 75 hours for a gap size of 4 mm, the average crystal size and the number of heterochiral agglomerations strongly decrease.

Finally, total deracemization occurs after 90 hours and 200 hours, for gap size of 2 mm and 4 mm respectively.

Unfortunately, technical issues with our reactor, *i.e.* leak of the seal (see part II.B), prevent longer experiment than 48 hours but those results suggest that deracemization is not fully blocked by the excessive crystal growth and heterochiral agglomeration, it could be simply a transient state. Indeed, deracemization curves present a slowdown of the CEE evolution, corresponding to the higher average crystal size, then deracemization is hastened and the average crystal size decreases (Figure IV-15) concomitantly. It appears that a phenomenon happens in the CT reactor and induces re-breakage of crystals and agglomerates, leading to the total symmetry breaking. While, this phenomenon might be related to a change in the fluid dynamics due to the important enlargement of crystals, further studies are required to determine the origin of this phenomenon.

Thus, although preliminary, the results collected during this work showed the feasibility of $NaClO_3$ deracemization in the CT reactor. Production-wise, the performance of the process could be improved by (i) recycling the enantiomerically enriched suspension at the end of the reactor, and (ii) by increasing the attrition between the crystals, *e.g.* by increasing fluid shear rates, which could inhibit excessive crystal growth and promote deracemization.

V. Perspectives

A. Optimization of the process in the CT Reactor

Since the efficiency of deracemization depends on the balance between mass transfer (to ensure Ostwald ripening) and crystal recycling (*i.e.*, the production of smaller crystals *via* attrition or secondary nucleation), further experiments should be performed in order to improve the process.

1. Inhibition of the Crystal Growth

In order to enhance deracemization of $NaClO_3$, crystal growth has to be partially inhibited but not blocked, as highlighted in the experiment performed in the presence of $Na_2S_2O_6$. In the literature, it is reported that crystal growth can be inhibited using an isothermal mode ($T_{inner} = T_{outer}$) or with the inversed non isothermal mode (*i.e.* where the inner cylinder is colder than the outer).[29] Therefore, several experiments can be envisaged from these

observation: using $\Delta T = 0°C$ at 1200 rpm, an even larger ΔT value (*i.e.*, > 20°C) at $\Omega = 600$ rpm. Larger range of ΔT combined with a larger range of Ω should be investigated.

Besides, attrition in the CT reactor can be improved by using foreign particles, chemically inert, and added to the suspension to mimic the effect of glass beads in attrition enhanced deracemization process.[2]

2. Modification of the Reactor Geometry

Different studies underlined the importance of the gap size and the radius of the inner cylinder. Indeed, smaller gap size and larger inner cylinder radius improve the fluid shear force inhibiting crystal growth and agglomeration. CSD is strongly decreased by decreasing the gap size and increase of the inner cylinder radius.[17,43] Modifications of the reactor geometry have more significant effect on the CSD control, *i.e.* on the crystal growth and agglomeration, than the change of rotation speed or temperature gradient. Indeed, while experiments performed by Professor Kim's group did not highlighted the advantage of larger inner cylinder radius, deracemization time was divided by two in their experiments when the gap size was divided by two, whereas not significant change was observed by changing the ΔT (from 10 to 20°C) or the Ω (from 600 to 1200 rpm) in our experiments.

B. Application to Organic Chiral Compounds

Deracemization of $NaClO_3$ has the advantage of a total amnesia of the chirality in solution since $NaClO_3$ molecules are achiral. Racemization of common chiral molecules could also be enhanced by Taylor vortices, as is the case for some other reported chemical reactions.[44] This would favor deracemization in the CT reactor and provide more efficient process compared to stirred tank crystallizer.[45,46] Suitable CT reactor geometry combined with the best parameters could give rise to faster and more robust deracemization processes than those performed in batch by using reactors, which makes CT reactors promising for deracemization.

C. Continuous Process

Couette Taylor reactor provides the possibility to work in a continuous flow, which could be a promising improvement for deracemization process and more generally, for

crystallization processes. By means of a continuous feeding and collecting on opposite ends of the CT reactor, continuous deracemization could be implemented.

Up to now, the residence time required for total deracemization is of 48 hours. It is much too long to consider bringing the method to a continuous flow process and the process first require improvement of deracemization time to transfer it to a continuous process. Nevertheless, Kataoka and Maron showed that the mass transfer in Couette Taylor reactors (*i.e.*, related to the crystal growth) was considerably decreased when a sufficient axial flow was added to the Taylor vortex flow.[6,7] Implementation of a continuous flow of the suspension in the CT reactor will generate an axial flow, in addition of the Taylor vortex flow, which decrease the mass transfer and then should improve deracemization.

Besides, other enantiomeric resolutions processes *via* crystallization, such as preferential crystallization or SOAT processes, are generally faster than deracemization,[47,48] thus study of those processes in a continuous way should be considered in the CT reactor for possible great improvements in terms of productivity.

VI. **Conclusion**

This chapter was focused on the implementation of a Couette Taylor (CT) reactor in order to investigate a new deracemization process. First experiments performed in this reactor were devoted to $NaClO_3$ deracemization and revealed its feasibility. The mechanisms involved in the CT reactor have been discussed.

The peculiar fluid flow involved in a CT reactor, *i.e.* Taylor vortex flow, enhances the mass transfer between liquid and solid phases, which improves the crystal growth and the agglomeration of crystals. This phenomenon has been also observed in our experiments and is thought responsible for several deracemization experiment failures. Indeed, deracemization process is based on efficient crystallization/dissolution cycles, whereas $NaClO_3$ crystals in suspension in the CT reactor often excessively grow (and/or agglomerate) which jeopardize total chiral symmetry breaking in absence of crystal recycling.[36]

Nevertheless, a suitable combination of the right temperature gap (ΔT) and rotation speed (Ω) showed the feasibility of the $NaClO_3$ deracemization as $NaClO_3$ deracemization was successfully achieved under 48 hours in several experiments.

Besides the geometry of the reactor (mainly the gap size and the radius of the inner cylinder) was suggested as a key factor to efficiently inhibit the crystal growth and agglomeration.[17] Studies showed that the smaller the gap size, the higher the fluid shear which reduces the propensity for crystals to grow.[29]

Up to now, deracemization in CT reactor was not shown to be more efficient than standard batch procedure (*i.e.*, *via* regular attrition or temperature cycling where deracemization occurred under 24 and 36 hours respectively) but potential improvements have been suggested and further experiments are required to fully assess the potential of this technique for chiral resolution.

References

1. Mullin, J. W. *Crystallization*. (Elsevier, 2001).

2. Sögütoglu, L.-C., Steendam, R. R. E., Meekes, H., Vlieg, E. & Rutjes, F. P. J. T. Viedma ripening: a reliable crystallisation method to reach single chirality. *Chem. Soc. Rev.* **44**, 6723–6732 (2015).

3. Suwannasang, K., Flood, A. E., Rougeot, C. & Coquerel, G. Using Programmed Heating–Cooling Cycles with Racemization in Solution for Complete Symmetry Breaking of a Conglomerate Forming System. *Cryst. Growth Des.* **13**, 3498–3504 (2013).

4. Breveglieri, F., Maggioni, G. M. & Mazzotti, M. Deracemization of NMPA via Temperature Cycles. *Cryst. Growth Des.* **18**, 1873–1881 (2018).

5. Steendam, R. R. E. & ter Horst, J. H. Scaling Up Temperature Cycling-Induced Deracemization by Suppressing Nonstereoselective Processes. *Cryst. Growth Des.* **18**, 3008–3015 (2018).

6. Kataoka, K., Doi, H. & Komai, T. Heat/mass transfer in taylor vortex flow with constant axial flow rates. *Int. J. Heat. Mass. Tran.* **20**, 57–63 (1977).

7. Maron, D. M. & Cohen, S. Hydrodynamics and Heat/Mass Transfer near Rotating Surfaces. in *Advances in Heat Transfer.* **21,** 141–183 (Elsevier, 1991).

8. Nguyen, A.-T., Yu, T. & Kim, W.-S. Couette-Taylor crystallizer: Effective control of crystal size distribution and recovery of l-lysine in cooling crystallization. *J. Cryst. Growth.* **469**, 65-77 (2016).

9. Kim, W.-S., Yu, T. & Wu, Z. Method for conducting deracemization using Taylor flow and a device therefor. US0081188A1 (2017).

10. Kim, W.-S. Application of Taylor Vortex to Crystallization. *J. Chem. Eng. Japan.* **47**, 115–123 (2014).

11. Couette, M. Distinction de deux régimes dans le mouvement des fluides. *J. Phys. Theor. Appl.* **9**, 414–424 (1890).

12. Jung, W. M., Kang, S. H., Kim, W.-S. & Choi, C. K. Particle morphology of calcium carbonate precipitated by gas–liquid reaction in a Couette–Taylor reactor. *Chemical Engineering Science.* **55**, 733–747 (2000).

13. Marchisio, D. L., Barresi, A. A. & Fox, R. O. Simulation of turbulent precipitation in a semi-batch Taylor-Couette reactor using CFD. *AIChE J.* **47**, 664–676 (2001).

14. Kang, S. H. *et al.* Effect of Taylor vortices on calcium carbonate crystallization by gas–liquid reaction. *Journal of Crystal Growth.* **254**, 196–205 (2003).

15. Lee, S., Choi, A., Kim, W.-S. & Myerson, A. S. Phase Transformation of Sulfamerazine Using a Taylor Vortex. *Cryst. Growth Des.* **11**, 5019–5029 (2011).

16. Nguyen, A.-T., Kim, J.-M., Chang, S.-M. & Kim, W.-S. Taylor Vortex Effect on Phase Transformation of Guanosine 5-Monophosphate in Drowning-Out Crystallization. *Industrial & Engineering Chemistry Research.* **49**, 4865–4872 (2010).

17. Mayra, Q.-P. & Kim, W.-S. Agglomeration of Ni-Rich Hydroxide in Reaction Crystallization: Effect of Taylor Vortex Dimension and Intensity. *Cryst. Growth Des.* **15**, 1726–1734 (2015).

18. Thai, D. K., Mayra, Q.-P. & Kim, W.-S. Agglomeration of Ni-rich hydroxide crystals in Taylor vortex flow. *Powder Technol.* **274**, 5–13 (2015).

19. Jung, W.-M., Hoon Kang, S., Kim, K.-S., Kim, W.-S. & Kyun Choi, C. Precipitation of calcium carbonate particles by gas–liquid reaction: Morphology and size distribution of particles in Couette-Taylor and stirred tank reactors. *J. Cryst. Growth.* **312**, 3331–3339 (2010).

20. Viedma, C. Chiral Symmetry Breaking During Crystallization: Complete Chiral Purity Induced by Nonlinear Autocatalysis and Recycling. *Phys. Rev. Lett.* **94**, 065504 (2005).

21. Mallock, A. III. Experiments on fluid viscosity. *Phil. Trans. A.* **187**, 40–56 (1896).

22. Davey, A. The growth of Taylor vortices in flow between rotating cylinders. *J. Fluid Mech.* **14**, 336–368 (1962).

23. Stuart, J. T. On the non-linear mechanics of hydrodynamic stability. *J. Fluid Mech.* **4**, 1–21 (1958).

24. Taylor, G. I. Stability of a Viscous Liquid Contained between Two Rotating Cylinders. *Phil. Trans. A.* **223**, 289–343 (1923).

25. Coles, D. Transition in circular Couette flow. *J. Fluid Mech.* **21**, 385–425 (1965).

26. Fenstermacher, P. R., Swinney, H. L. & Gollub, J. P. Dynamical instabilities and the transition to chaotic Taylor vortex flow. *J. Fluid Mech.* **94**, 103–128 (1979).

27. Andereck, C. D., Liu, S. S. & Swinney, H. L. Flow regimes in a circular Couette system with independently rotating cylinders. *J. Fluid Mech.* **164**, 155–183 (1986).

28. Fénot, M., Bertin, Y., Dorignac, E. & Lalizel, G. A review of heat transfer between concentric rotating cylinders with or without axial flow. *International Journal of Thermal Sciences.* **50**, 1138–1155 (2011).

29. Wu, Z., Seok, S., Kim, D. H. & Kim, W.-S. Control of Crystal Size Distribution using Non-Isothermal Taylor Vortex Flow. *Cryst. Growth Des.* **15**, 5675–5684 (2015).

30. *Micro and macro mixing: analysis, simulation and numerical calculation*. (Springer, 2010).

31. Kondepudi, D. K., Kaufman, R. J. & Singh, N. Chiral Symmetry Breaking in Sodium Chlorate Crystallization. *Science.* **250**, 975–976 (1990).

32. Lan, Z.-P., Lai, X., Roberts, K. & Klapper, H. X-ray Topographic and Polarized Optical Microscopy Studies of Inversion Twinning in Sodium Chlorate Single Crystals Grown in the Presence of Sodium Dithionate Impurities. *Cryst. Growth Des.* **14**, 6084–6092 (2014).

33. Ostwald, W. Studien über die Bildung und Umwandlung fester Körper. *Z. Phys. Chem.* **22U**, 289–330 (1897).

34. Karpiński, P. H. Crystallization as a mass transfer phenomenon. *Chem. Eng. Sci.* **35**, 2321–2324 (1980).

35. Uwaha, M. A Model for Complete Chiral Crystallization. *J. Phys. Soc. Jpn.* **73**, 2601–2603 (2004).

36. Saito, Y. & Hyuga, H. Complete Homochirality Induced by Nonlinear Autocatalysis and Recycling. *J. Phys. Soc. Jpn* **73**, 33–35 (2004).

37. Xiouras, C., Van Aeken, J., Panis, J., Ter Horst, J.H., Van Gerven, T., Stefanidis, G.D., Attrition-Enhanced Deracemization of $NaClO_3$: Comparison between Ultrasonic and Abrasive Grinding. *Cryst. Growth Des.* **15**, 5476–5484 (2015).

38. Schindler, M., Brandel, C., Kim, W.-S. & Coquerel, G. Temperature cycling induced deracemization (TCID) of $NaClO_3$ under the influence of $Na_2S_2O_6$. *Cryst. Growth Des.* **20***,* 414-421, (2020)

39. Noorduin, W. L. *et al.* The Driving Mechanism Behind Attrition-Enhanced Deracemization. *Angew. Chem.* **122**, 8613–8616 (2010).

40. Bodák, B., Maggioni, G. M. & Mazzotti, M. Population-Based Mathematical Model of Solid-State Deracemization via Temperature Cycles. *Cryst. Growth Des.* **18**, 7122–7131 (2018).

41. Cameli, F., ter Horst, J. H., Steendam, R. R. E., Xiouras, C. & Stefanidis, G. D. On the Effect of Secondary Nucleation on Deracemization via Temperature cycles. *Chem. Eur. J.* **26**, 1344-1354 (2020).

42. Bakar, M. R. A., Nagy, Z. K. & Rielly, C. D. Seeded Batch Cooling Crystallization with Temperature Cycling for the Control of Size Uniformity and Polymorphic Purity of Sulfathiazole Crystals. *Org. Process Res. Dev.* **13**, 1343–1356 (2009).

43. Shaqfeh, E. S. G., Muller, S. J. & Larson, R. G. The effects of gap width and dilute solution properties on the viscoelastic Taylor-Couette instability. *J. Fluid Mech.* **235**, 285 (1992).

44. Judat, B., Racina, A. & Kind, M. Macro- and Micromixing in a Taylor-Couette Reactor with Axial Flow and their Influence on the Precipitation of Barium Sulfate. *Chem. Eng. Technol.* **27**, 287–292 (2004).

45. Oketani, R., Hoquante, M., Brandel, C., Cardinael, P. & Coquerel, G. Practical Role of Racemization Rates in Deracemization Kinetics and Process Productivities. *Cryst. Growth Des.* **18**, 6417–6420 (2018).

46. Breveglieri, F. & Mazzotti, M. Role of Racemization Kinetics in the Deracemization Process via Temperature Cycles. *Cryst. Growth Des.* **19**, 3551–3558 (2019).

47. Gendron, F.-X., Mahieux, J., Sanselme, M. & Coquerel, G. Resolution of Baclofenium Hydrogenomaleate By Using Preferential Crystallization. A First Case of Complete Solid Solution at High Temperature and a Large Miscibility Gap in the Solid State. *Cryst. Growth Des.* **19**, 4793–4801 (2019).

48. Oketani, R. *et al.* Deracemization in a Complex Quaternary System with a Second-Order Asymmetric Transformation by Using Phase Diagram Studies. *Chem. Eur. J.* **25**, 13890–13898 (2019).

General Conclusion

This work was dedicated to the crystallization mechanisms involved during deracemization of sodium chlorate ($NaClO_3$) under temperature cycling (Temperature Cycling Induced Deracemization, TCID) and in Couette Taylor (CT) reactor. Solid state characterization of sodium dithionate ($Na_2S_2O_6$) has also been a part of this work before using this compound as a non-chiral impurity in $NaClO_3$ deracemization.

$Na_2S_2O_6$ is not commercially available and had to be synthesized then characterized by complementary experimental tools to describe the behavior of the anhydrous and the dihydrated forms as a function of temperature or relative humidity (RH). The dehydration of $Na_2S_2O_6 \cdot 2H_2O$ occurs at 56°C. At room temperature, reversible dehydration occurs between 40 and 50%RH. While we did not succeed in resolving the crystal structure of the anhydrous form, the various experiments performed to grow single crystals led to the discovery of a new solvate of dimethyl sulfoxide (DMSO). Thus, the crystal structure of the $Na_2S_2O_6 \cdot 3(C_2H_6SO)$ has been resolved by single crystal-X-ray diffraction.

While $NaClO_3$ deracemization was intensively studied *via* Viedma ripening, TCID for this model compound is a novelty of this work. The mild temperature dependence of $NaClO_3$ solubility and the high crystal growth rate of $NaClO_3$ crystals required large temperature variations and fast cooling rate to complete deracemization. It has been shown that the success of the TCID process depends on the right balance between growth and secondary nucleation. Indeed, the study of the influence of $Na_2S_2O_6$ on the $NaClO_3$ TCID process revealed the importance of secondary nucleation in TCID. Deracemization of $NaClO_3$ was exponentially delayed as a function of the $Na_2S_2O_6$ amount due to the blockage of secondary nucleation and crystal growth of $NaClO_3$ during the cooling steps. Whereas chiral impurities in regular chiral compound deracemization usually affects only one enantiomer which hastens deracemization towards the counter enantiomer, in our case, $Na_2S_2O_6$ affects both enantiomers of $NaClO_3$ which delays the whole deracemization process. This study introduced new reflections about deracemization mechanism *via* temperature cycles. While Ostwald ripening and re-incorporation of chiral clusters provide crystal recycling in Viedma ripening process, controlled secondary nucleation seems to ensure success of TCID process.

The last part of this work was devoted to the implementation of a new reactor in order to develop a continuous process of deracemization. From an industrial perspective, development of a continuous process (Couette-Taylor) is desirable regarding the productivity. $NaClO_3$ deracemization experiments were successful albeit optimizable. While improvements are required to consider a transfer to continuous, the feasibility of

total symmetry breaking of $NaClO_3$ has been evidenced in CT reactor. Crystal recycling has to be improved in CT reactor to enhance symmetry breaking. Indeed, growth, ripening and agglomeration of crystals are strongly favored by the large mass transfer existing in the CT reactor, and the recycling of crystals must be more efficient to lead to a robust deracemization process. Further experiments were thus suggested: (i) More effective temperature cycles could favor secondary nucleation or (ii) higher rotation speed of the inner cylinder could generate more attrition and enhance re incorporation of chiral clusters, as in Viedma ripening process.

This Ph.D. work bring new reflections about the mechanism involved in TCID process and the key role of secondary nucleation, which is central in the achievement of deracemization in CT reactor. This new reactor is a promising device for continuous process of deracemization.

Appendices

A. **Experimental Part**

1. Infra Red Spectroscopy

Infra-red spectra were acquired using an ATR-FTIR spectrometer (Alpha FT-IR spectrometer, Bruker). The powdered samples were slightly ground before being deposited on the ATR. For each spectrum, a total of 64 scans were recorded at room temperature between 4000 and 400 cm^{-1}.

2. X-Ray Powder Diffraction (XRPD)

XRPD analyzes were performed using a D8-Discover diffractometer (Bruker, Germany) equipped with a goniometer of geometry (θ/θ). The incident X-ray beam consisted of the Cu Kα radiation (λ=1.5418 Å) with a tube voltage and amperage set at 40 kV and 40 mA respectively. The X-ray diffraction patterns were collected with a Lynx Eye® linear detector (Bruker, Germany). The X-ray diffraction patterns were recorded by steps of 0.02° over the angular 2θ range 15-40° with a counting time of 1s per step. The position of characteristic powder diffraction peaks are expressed in degrees 2-theta

3. Temperature Resolved X-Ray Powder Diffraction (TR-XRPD)

TR- X-Ray diffraction analyses were performed using a D5005 diffractometer (Siemens-Bruker). X-ray beam is generated by a sealed Cu Source (40 kV, 40 mA), and a K_β filter (Ni). Patterns were measured with steps of 0.04° with a counting time of 4 seconds per step over an angular range 8- 60°. Temperature of the chamber and sample holder of the diffractometer is controlled using a TTK 450 heating stage (Anton Paar). Diffraction patterns are collected at different temperatures (from room temperature to 304°C) to characterize the phases in the presence as a function of temperature.

4. Thermogravimetry Differential Scanning Calorimetry (TG-DSC)

TG-DSC analyses are carried out with a STA 409 PC instrument (Netzsch). The DSC and TGA signal are plotted against temperature. Around 10mg of $Na_2S_2O_6,2H_2O$ were analyzed in aluminium sealed pierced crucible and heated at a rate of 5°C/min from 20°C to 300°C. Helium was used as a purging gas. Proteus® Software (Netzsch) was used for data treatment.

5. Dynamic Vapor Sorption (DVS)

DVS isotherms were performed on a DVS-1 automated water sorption analyzer (Surface Measurement Systems, Alperton, U.K.). 30mg of $Na_2S_2O_6$,$2H_2O$ were analyzed from 90 to 0% relative humidity (RH) by steps of 10%RH, at an isothermal temperature of 25°C and 43°C. Steps were maintained as long as the relative mass variations dm/dt remained below 0.0005% for 10min. The maximum stabilization time was adjusted to 2000min. The partial vapour pressure was controlled with a precision of +/- 0,5%. Mass variations were recorded with a precision of 0.1µg and plotted against RH

6. Microscopy

Optical microscopy pictures were obtained on a Nikon Eclipse LV100 optical microscope equipped with a pair of cross polarizers. $NaClO_3$ crystals were observed with a +5° tilt between the polarizer planes, then, dextrogyre crystals (*d*-crystals) appear blue and levogyre crystals (*l*-crystals) appear brown.

7. ImageJ Software

ImageJ is a software to edit, analyze, process, save and print images. In order to determine the CEE of $NaClO_3$ samples, crystal of each chirality were pointed and counted with ImageJ software. This software was also used for the measurement of the crystal growth by setting the scale and then measure the distance between the center of the crystal and the middle of the considered face along the growth experiment.

8. Structure Resolution of Single Crystal

- Single crystal X-ray diffraction:

The crystal structure of sodium dithionate DMSO solvate $Na_2S_2O_6$, 3DMSO has been determined from single crystal X-Ray diffraction. The chosen crystal was placed in a capillary with mother liquor and mounted on the full three-circle goniometer of a Bruker SMART APEX diffractometer with a CCD area detector. Four sets of exposures (a total of 1350 frames) were recorded, corresponding to four ω scans (steps of 0.3°), for four different values of ϕ.

The cell parameters and the orientation matrix of the crystal were preliminary determined by using SMART Software[i]. Data integration and global cell refinement were performed with SAINT Software[ii]. Intensities were corrected for Lorentz, polarisation, decay and absorption effects (SAINT and SADABS Softwares) and reduced to F_o^2. The program package WinGX[iii] was used for space group determination, structure solution and refinement.

- Crystallographic data of the $Na_2S_2O_6,3(C_2H_6SO)$ structure:

The non-standard space group $P2_1/n$ (n°14) was determined from systematic extinctions and relative F_O^2 of equivalent reflections. The structure was solved by direct methods[iv]. Anisotropic displacement parameters were refined for all non-hydrogen atoms. Every Hydrogen atoms were located from subsequent difference Fourier syntheses and placed with geometrical constraints (SHELXL[v]). The crystal data are collected in Table 1.

Table 1: Crystal data

Chemical Formula	**$Na_2S_2O_6$,3DMSO**
Molecular Weight / *g.mol*$^{-1}$	440.5
Crystal System	Monoclinic
Space Group	$P2_1/n$
Z , Z' (asymmetric units per unit cell)	4,1
a / *Å*	10.846(1)
b / *Å*	8.5185(9)
c / *Å*	19.676(2)
β / °	96.162(2)
V / *Å*^{3}	1807.5(3)
d_{calc} / *g.cm*$^{-3}$	1.619
Final R indices [I>2sigma(I)]	R1 = 0.0766, wR2 = 0.2104
Unique reflections / with I> 2.σ(I)	3721 / 2788

(i) SMART for WNT/2000 V5.622 (2001), Smart software reference manual, Bruker Advanced X Ray Solutions, Inc., Madison, Wisconsin, USA.

(ii) SAINT+ V6.02 (1999), Saint software reference manual, Bruker Advanced X Ray Solutions, Inc., Madison, Wisconsin, USA.

(iii) WinGX: Version 1.70.01: An integrated system of Windows Programs for the solution, refinement and analysis of Single Crystal X-Ray Diffraction Data, By LouisJ. Farrugia, Dept. of chemistry, University of Glasgow. L. J. Farrugia (1999) J. Appl. Cryst. 32, 837-838.

(iv) include in WinGX suite : SIR 92: A. Altomare, G. Cascarano, & A. Gualardi (1993) J. Appl. Cryst. 26, 343-350; SHELXS-97: Sheldrick, G. M., (1990) Acta cryst, A46, 467.

(v) include in WinGX suite: SHELXL-97 – a program for crystal structure refinement, G. M. .Sheldrick, University of Goettingen, Germany, 1997, release 97-2.

B. Supplementary Curves and Tables on Deracemization of $NaClO_3$ via Attrition Enhanced Deracemization and TCID.

1. $NaClO_3$ deracemization experiments without $Na_2S_2O_6$

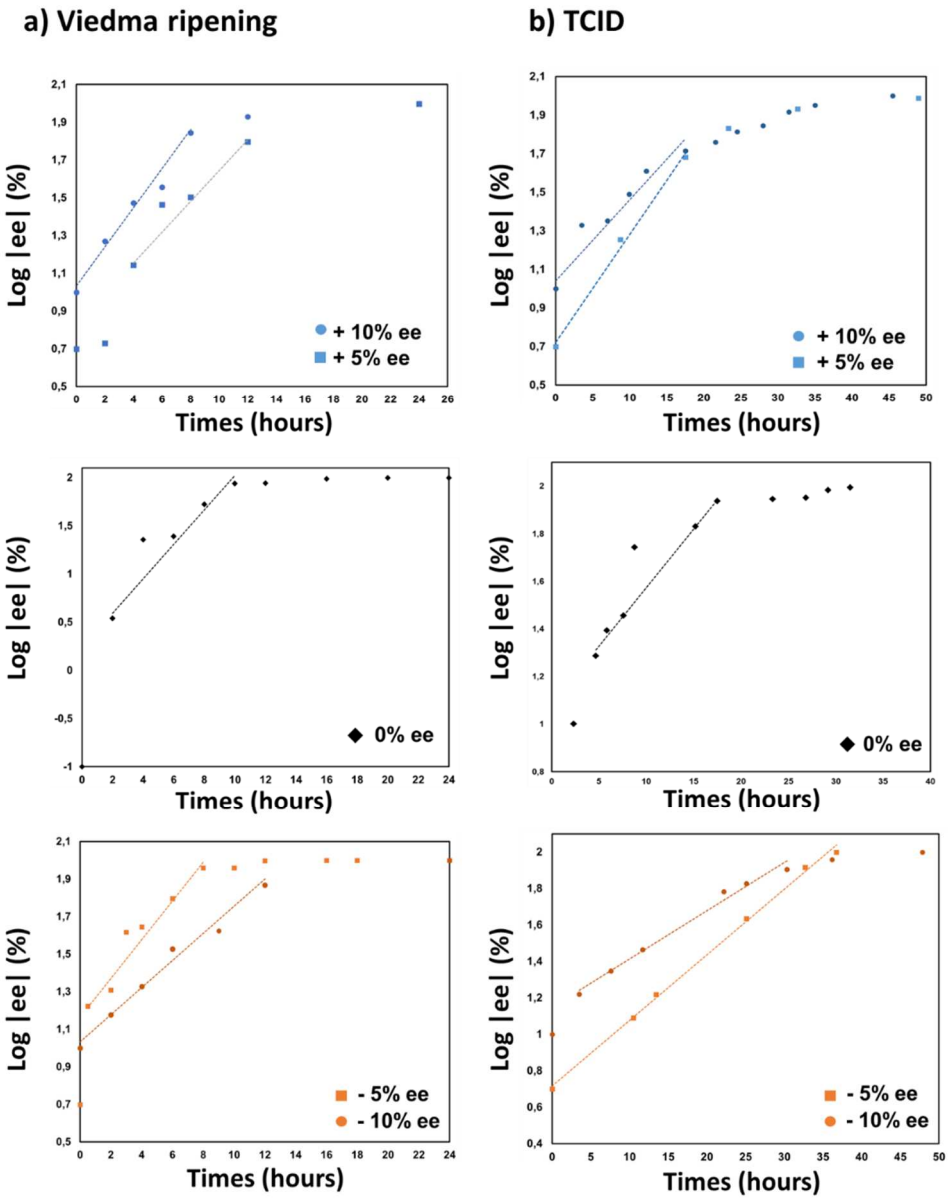

Figure II: Evolution of the log |ee|(%) as a function of the time of a) VR experiments and b) TCID experiments. The line is the linear regression, detailed in table I. Inlay indicates the starting $ee_{crystal}$.

Table I: Summary of linear regressions of the VR deracemization experiments (left) and TCID deracemization experiments (right)

	Viedma Ripening		TCID	
ee initial	Linear regression	r^2	Linear regression	r^2
- 10%	Log |ee| = 0.0722 * *t* + 1.0329	0.9869	Log |ee| = 0.0265 * *t* + 1.148	0.9875
- 5%	Log |ee| = 0.1035 * *t* + 1.1621	0.9757	Log |ee| = 0.036 * *t* + 0.7159	0.9977
0%	Log |ee| = 0.1786* *t* + 0.2383	0.9823	Log |ee| = 0.0492 * *t* + 1.0821	0.9960
5%	Log |ee| = 0.0815 * *t* + 0.8291	0.9967	Log |ee| = 0.0561 * *t* + 0.7207	0.9942
10%	Log |ee| = 0.0986 * *t* + 1.0338	0.98039	Log |ee| = 0.0421 * *t* +1.0401	0.9684

2. $NaClO_3$ deracemization experiments in the presence of $Na_2S_2O_6$

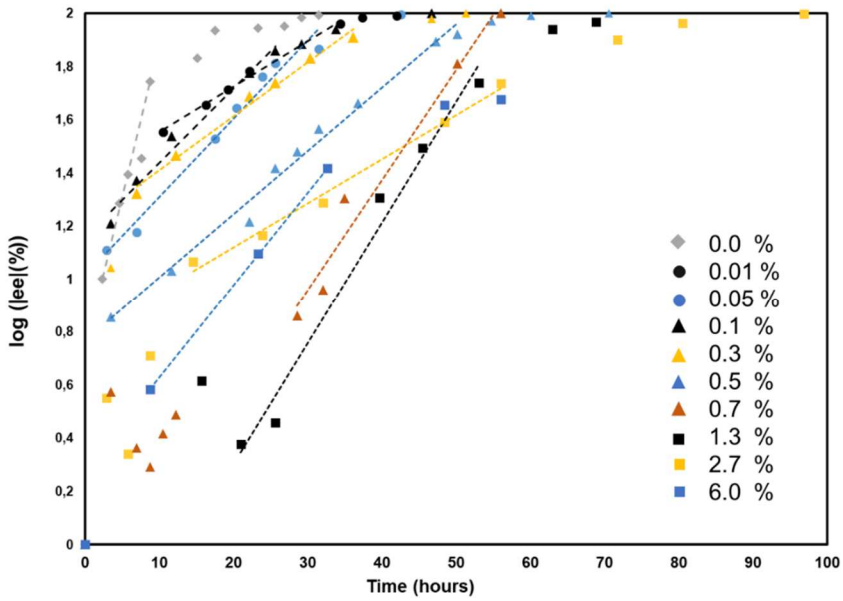

Figure III: Evolution of the log |ee|(%) as a function of the time of TCID experiments in the presence of $Na_2S_2O_6$. The line is the linear regression, detailed in table II. Inlay indicates the starting %mol of $Na_2S_2O_6$.

Table II: Summary of linear regressions of the VR deracemization experiments (left) and TCID deracemization experiments (right)

%mol $Na_2S_2O_6$	Linear regression	r^2
0%	Log |ee| = 0.0492 * *t* + 1.0821	0.9960
0.01%	Log |ee| = 0.0171 * *t* + 1.3838	0.9922
0.05%	Log |ee| = 0.0294 * *t* + 1.0169	0.9778
0.1%	Log |ee| = 0.028 * *t* + 1.1585	0.9812
0.3%	Log |ee| = 0.0203 * *t* + 1.2091	0.9884
0.5%	Log |ee| = 0.0238 * *t* + 0.7698	0.9877
0.7%	Log |ee| = 0.0414 * *t* - 0.2851	0.9711
1.3%	Log |ee| = 0.0457 * *t* + 0.6135	0.9813
2%	Log |ee| = 0.0166 * *t* + 0.7897	0.9905
6%	Log |ee| = 0.0349 * *t* + 0.2783	0.9999

C. Scientific Production

1. Publications

"Synthesis and Characterization of sodium dithionate and its dihydrate", M. Schindler, N. Couvrat, , Y.Cartigny, C. Brandel, G. Coquerel, **Chemical Engineering & Technology (2019)** I.F.: 2.418

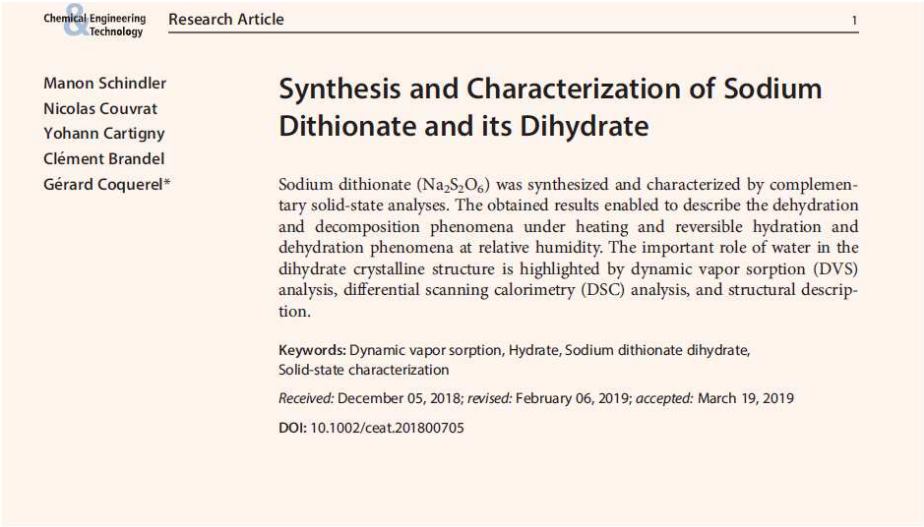

Chemical Engineering & Technology Research Article 1

Manon Schindler
Nicolas Couvrat
Yohann Cartigny
Clément Brandel
Gérard Coquerel*

Synthesis and Characterization of Sodium Dithionate and its Dihydrate

Sodium dithionate ($Na_2S_2O_6$) was synthesized and characterized by complementary solid-state analyses. The obtained results enabled to describe the dehydration and decomposition phenomena under heating and reversible hydration and dehydration phenomena at relative humidity. The important role of water in the dihydrate crystalline structure is highlighted by dynamic vapor sorption (DVS) analysis, differential scanning calorimetry (DSC) analysis, and structural description.

Keywords: Dynamic vapor sorption, Hydrate, Sodium dithionate dihydrate, Solid-state characterization

Received: December 05, 2018; *revised:* February 06, 2019; *accepted:* March 19, 2019

DOI: 10.1002/ceat.201800705

"Temperature cycling induced deracemization (TCID) of NaClO3 under the influence of Na2S2O6" M. Schindler, C. Brandel, W.-S. Kim and G. Coquerel, **Crystal Growth and Design (2019)** I.F.: 4.153

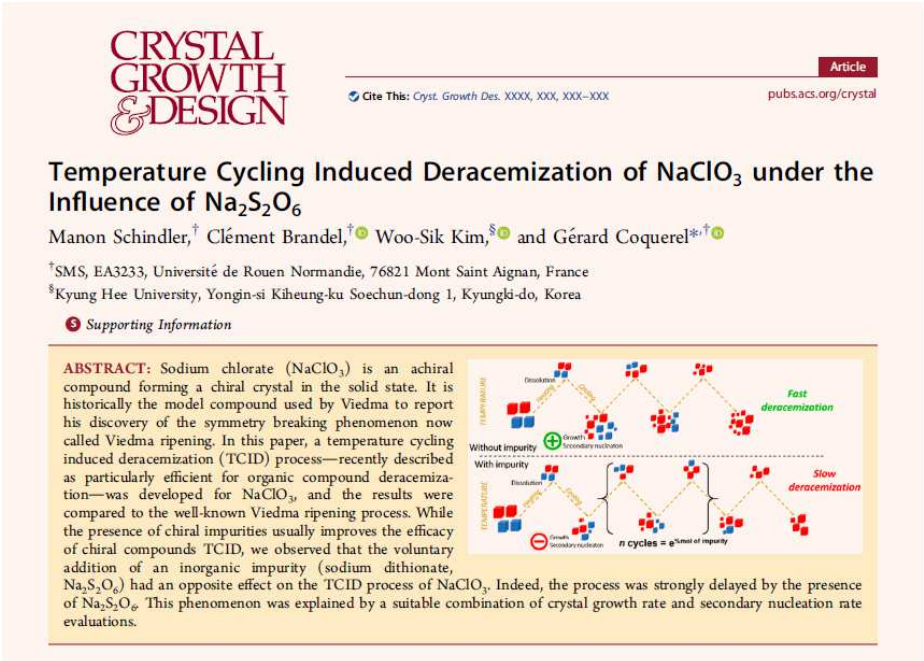

CRYSTAL GROWTH & DESIGN

Article

Cite This: *Cryst. Growth Des.* XXXX, XXX, XXX−XXX

pubs.acs.org/crystal

Temperature Cycling Induced Deracemization of $NaClO_3$ under the Influence of $Na_2S_2O_6$

Manon Schindler,[†] Clément Brandel,[†] Woo-Sik Kim,[§] and Gérard Coquerel*[,†]

[†]SMS, EA3233, Université de Rouen Normandie, 76821 Mont Saint Aignan, France
[§]Kyung Hee University, Yongin-si Kiheung-ku Soechun-dong 1, Kyungki-do, Korea

Supporting Information

ABSTRACT: Sodium chlorate ($NaClO_3$) is an achiral compound forming a chiral crystal in the solid state. It is historically the model compound used by Viedma to report his discovery of the symmetry breaking phenomenon now called Viedma ripening. In this paper, a temperature cycling induced deracemization (TCID) process—recently described as particularly efficient for organic compound deracemization—was developed for $NaClO_3$, and the results were compared to the well-known Viedma ripening process. While the presence of chiral impurities usually improves the efficacy of chiral compounds TCID, we observed that the voluntary addition of an inorganic impurity (sodium dithionate, $Na_2S_2O_6$) had an opposite effect on the TCID process of $NaClO_3$. Indeed, the process was strongly delayed by the presence of $Na_2S_2O_6$. This phenomenon was explained by a suitable combination of crystal growth rate and secondary nucleation rate evaluations.

2. Oral communications

"*Detection of a metatectic invariant in the system 1,3-dimethylurea/water and crystal structure determination of DMU monohydrate"* **M. Schindler**, G. Baaklini, Y.Cartigny, N. Couvrat, M. Sanselme, C. Brandel, G. Coquerel, **JEEP, Barcelone (Espagne), Mars 2017**

"*Crystallization and macroscopic symmetry breakings"* **G. Coquerel**, R. Oketani, F-X. Gendron, M. Schindler, S. Clevers, C. De Saint Jores, P. Cardinaël, N. El Gharbi, R. Kuroda, et C. Brandel. **Symposium on Molecular Chirality 2018**, **Chiba (Japon), Juin 2018.**

"Deracemization of $NaClO_3$ by TCID under the influence of $Na_2S_2O_6$" **M. Schindler**, C. Brandel, G. Coquerel, **BIWIC, Rayong (Thailand), Août 2019**

3. Poster presentations

"*Study of the behaviour of the 1,3-dimethyluera in presence of water : Construction of the binary system*." **M. Schindler**, G. Baaklini, Y.Cartigny, N. Couvrat, M. Sanselme, G. Coquerel., **Journées Nord-Ouest Européennes des Jeunes Chercheurs, Lille (France), Juin 2016.**

"*Influence of water on the behaviour of the 1,3-dimethylurea studied by construction of the binary phase diagram"* **M. Schindler**, G. Baaklini, Y.Cartigny, N. Couvrat, M. Sanselme, G. Coquerel, **Cristech, Autrans (France), Octobre 2016.**

"Morphology of sodium bromate ($NaBrO_3$) under the influence of purified sodium dithionate ($Na_2S_2O_6$)" **M. Schindler**, C. Brandel, G. Coquerel, **JEEP, JEEP, Barcelona (Spain), March 2017.**

"Maturation of a population of crystals by using a Couette-Taylor reactor" **F.-X. Gendron**, M. Schindler, C. Brandel, W.-S. Kim, G. Coquerel. **BIWIC, Dortmund (Allemagne), Août 2017.**

"Determination of the crystal structure of a hydrate of 1-3-dimethylurea (DMU) stable at low temperature" M. Schindler, M. Sanselme, P. Négrier, D. Mondieig, **G. Gbabode**, G. Coquerel, **Colloque de l'Association Française de Cristallographie, Lyon (France), Juillet 2018.**

"*Deracemization of sodium chlorate in the presence of sodium dithionate impurity*" M. Schindler, C. Brandel, **G. Coquerel, CGOM, Seoul (Korea), Août 2018**.

"Influence of $Na_2S_2O_6$ on $NaClO_3$ deracemization" **M. Schindler**, C. Brandel, G. Coquerel, **BIWIC, Rouen (France), Septembre 2018**

Abtsract

In the field of pharmaceutical chemistry, crystallization based methods are used to obtain pure enantiomers. The advantage of deracemization is the conversion of the unwanted enantiomer into the desired enantiomer by means of racemization in liquid phase, giving rise to a theoretical yield of 100%. The mechanism of *Temperature Cycling Induced Deracemization* (TCID) process, still matter of debate, has been investigated in this thesis. Research was focused on the development of the TCID process for sodium chlorate ($NaClO_3$). This model compound is achiral at the solvated state which enables to focus investigation on crystallization mechanisms involved during deracemization.

After the full solid state characterization of sodium dithionate ($Na_2S_2O_6$), this compound has been used as a non-chiral impurity in the TCID process of $NaClO_3$ and highlighted the key role of secondary nucleation in the process. Thus, the success of the TCID process depends on the right balance between growth and secondary nucleation.

From an industrial perspective, the *Couette Taylor* reactor has been considered as a promising device for the development of continuous deracemization process. Attempts to deracemize $NaClO_3$ in this kind of reactor showed that symmetry breaking and deracemization of $NaClO_3$ were successful. Nonetheless, crystal recycling, *via* either attrition or secondary nucleation, has to be improved to enhance deracemization process before considering the execution of continuous process.

Key Words: Deracemization, Sodium Chlorate, Sodium Dithionate, Impurity, Couette Taylor Reactor, Secondary Nucleation, Crystal Growth

Résumé

Dans le domaine pharmaceutique, la séparation des énantiomères est souvent effectuée par des méthodes de cristallization. L'avantage de la déracémisation est la possibilité d'obtenir un rendement théorique de 100% grâce à la conversion du contre énantiomère en l'énantiomère désiré en solution. Le mécanisme de la déracemisation par cycles de température (TCID), a été étudié dans ce manuscrit. Les recherches se sont concentrées sur le développement d'un procédé de TCID pour $NaClO_3$. Ce composé modèle pour la déracémisation est achiral à l'état solvaté, ce qui permet de se focaliser sur les méchanismes de cristallisation impliqués dans le procédé de déracémisation.

Après la caractérisation complète de l'état solide de $Na_2S_2O_6$, ce composé a été utilisé comme une impureté non-chirale dans le procédé de TCID du $NaClO_3$ et a permis de mettre en évidence le rôle important de la nucléation secondaire dans le procédé. Ainsi, le succès du TCID dépend d'un bon équilibre entre la croissance des cristaux et la nucléation secondaire.

A des fins industrielles, les réacteurs du type Couette Taylor sont des appareils prometteurs pour le développement de procédés de déracémisation en continu. Les premiers tests de déracémisation réalisés dans ce type de réacteur ont montré que la brisure de symétrie et la déracémisation du $NaClO_3$ ont été réalisés avec succès. Néanmoins, le « recyclage de cristaux », soit par attrition soit par la nucléation secondaire, doit être amélioré pour obtenir un procédé de déracémisation plus performant avant de considérer l'implémentation d'un procédé en continu.

Mots Clés : Déracémisation, Chlorate de Sodium, Dithionate de Sodium, Impureté, Réacteur Couette Taylor, Nucléation Secondaire, Croissance Cristalline